

AD-A118 847

MASSACHUSETTS INST OF TECH LEXINGTON LINCOLN LAB
SOLID STATE RESEARCH: 1982-1.(U)
FEB 82 A L MCWHORTER

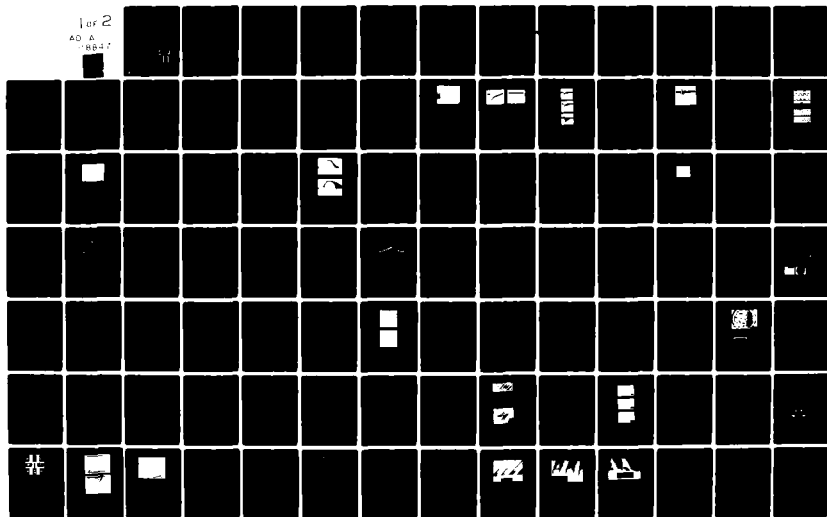
F/6 9/5

UNCLASSIFIED

ESD-TR-82-010

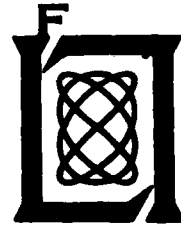
F19628-80-C-0002
NL

for 2
AD A
8847



12

AD A118847

	1
<p>Solid State Research</p>	<p>1982</p> <p>DTIC ELECTE SEP 3 1982</p>
<p>Prepared under Electronic Systems Division Contract F19628-80-C-0002 by</p> <p>Lincoln Laboratory</p> <p>MASSACHUSETTS INSTITUTE OF TECHNOLOGY</p> <p>LEXINGTON, MASSACHUSETTS</p>	

DTIC FILE COPY

Approved for public release; distribution unlimited.

82 09 03 05 5

The work reported in this document was performed at Lincoln Laboratory, a center for research operated by Massachusetts Institute of Technology, with the support of the Department of the Air Force under Contract F19628-80-C-0002.

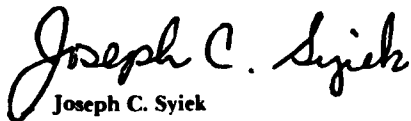
This report may be reproduced to satisfy needs of U.S. Government agencies.

The views and conclusions contained in this document are those of the contractor and should not be interpreted as necessarily representing the official policies, either expressed or implied, of the United States Government.

The Public Affairs Office has reviewed this report, and it is releasable to the National Technical Information Service, where it will be available to the general public, including foreign nationals.

This technical report has been reviewed and is approved for publication.

FOR THE COMMANDER



Joseph C. Syiek
Acting ESD Lincoln Laboratory Project Officer

Non-Lincoln Recipients
PLEASE DO NOT RETURN

Permission is given to destroy this document
when it is no longer needed.

MASSACHUSETTS INSTITUTE OF TECHNOLOGY
LINCOLN LABORATORY

SOLID STATE RESEARCH

QUARTERLY TECHNICAL SUMMARY REPORT

1 NOVEMBER 1981 — 31 JANUARY 1982

ISSUED 1 JULY 1982



Accession For	
NTIS GRA&I	<input checked="checked" type="checkbox"/>
DTIC TAB	<input type="checkbox"/>
Unannounced	<input type="checkbox"/>
Justification	
By	
Distribution/	
Availability Codes	
Dist	Avail and/or Special
A	

Approved for public release; distribution unlimited.

LEXINGTON

MASSACHUSETTS

ABSTRACT

This report covers in detail the solid state research work of the Solid State Division at Lincoln Laboratory for the period 1 November 1981 through 31 January 1982. The topics covered are Solid State Device Research, Quantum Electronics, Materials Research, Microelectronics, and Analog Device Technology. Funding is primarily provided by the Air Force, with additional support provided by the Army, DARPA, Navy, NASA, and DOE.

TABLE OF CONTENTS

Abstract	iii
Introduction	vii
Reports on Solid State Research	xi
Organization	xvii
 I. SOLID STATE DEVICE RESEARCH	 1
A. Picosecond InP Optoelectronic Switches	1
B. 4-Bit 828-MS/s Guided-Wave Electrooptic Analog-to-Digital Converter	7
C. A Novel Technique for GaInAsP/InP Buried Heterostructure Laser Fabrication	11
 II. QUANTUM ELECTRONICS	 19
A. Co:MgF ₂ Laser: High-Average-Power Operation, Q-Switched Performance, and Scaling Operations	19
B. Jahn-Teller Effect and the Optical Absorption Spectrum of V ²⁺ in MgF ₂	23
C. Raman Spectra of Ultrathin Si Films	27
D. Efficient GaAs Solar Cells Formed by UV Laser Chemical Doping	32
E. Fabrication of Through-Wafer Via Conductors in Si by Laser Photochemical Processing	36
F. Three-Terminal Device Used for Optical Heterodyning at Submillimeter IFs	39
 III. MATERIALS RESEARCH	 43
A. Properties of Zone-Melting-Recrystallized Si Films on SiO ₂ -Coated Substrates	43
1. Majority-Carrier Transport	45
2. Generation Lifetime	51
B. Preparation of Oriented GaAs Bicrystal Layers by Vapor-Phase Epitaxy Using Lateral Overgrowth	55

IV. MICROELECTRONICS	65
A. Vertical Single-Gate CMOS Inverters on Laser-Processed Multilayer Substrates	65
B. High-Resolution Ion-Beam Lithography	70
C. Charge-Coupled Devices: Two-Dimensional Correlator	78
V. ANALOG DEVICE TECHNOLOGY	87
A. Considerations for an Integrated Optical Spectrum Analyzer (IOSA)	87
1. Bragg-Cell Design	87
2. Output-Lens Design	92
B. Superconductive Convolver	93
C. Compact Multiple-Channel SAW Sliding-Window Spectrum Analyzer	98
1. System Architecture	99
2. Device Characteristics	100
3. The Spectrum Analyzer	101

INTRODUCTION

I. SOLID STATE DEVICE RESEARCH

The response speed of InP optoelectronic switches has been enhanced by using proton bombardment. Response times following bombardment of less than 100 ps have been deduced from photoconductivity measurements.

Individual bit channels of a 4-bit guided-wave electrooptic analog-to-digital converter have been operated at 828 MS/s. The conversion of an analog signal with the highest reported frequency of 413 MHz was demonstrated by means of a beat-frequency test.

A mass-transport phenomenon has been utilized to achieve GaInAsP/InP buried heterostructure (BH) lasers. The novel technique is considerably simpler and more easily controlled than previously reported ones, and has resulted in BH lasers with threshold currents as low as 9.0 mA.

II. QUANTUM ELECTRONICS

An average output power of 7.3 W at a 50-Hz pulse rate has been obtained from a Co:MgF₂ laser, and 20 mJ has been generated in a 200-ns-wide output pulse in Q-switched operation. Scaling relations to extend Q-switched operation to higher energies have been calculated.

As part of an effort to understand the basic mechanisms of the MgF₂:V²⁺ laser, a theoretical fit for the ${}^4A_2 \rightarrow {}^4T_2$ zero-phonon absorption spectrum in σ and π polarization has been obtained. The fit indicates the presence of a strong Jahn-Teller interaction for the 4T_2 level.

Raman spectra of ultrathin Si films are being investigated as a probe of grain sizes in beam-recrystallized semiconductor materials. A strong broadening, as well as a low-frequency tail in the Si phonon spectrum, is observed as the film thickness is decreased to ~ 30 Å.

Photolysis of H_2S with an ArF excimer laser has been used to form p-n junctions in GaAs by S-doping. Solar cells having AM1 efficiencies of 10.8 percent have been fabricated from these junctions.

Laser photochemical etching and deposition have been used to fabricate high-aspect-ratio, through-wafer via conductors. This technique for via-conductor fabrication should have application in the assembly of large-area focal-plane detectors.

Heterodyning in the visible has been carried out in GaAs FETs with IFs up to 300 GHz. This high-frequency response was independently verified in mixing experiments in the millimeter and submillimeter regimes. For IFs up to 40 GHz, the LO was injected directly into the gate, and the mixer operated as a three-terminal device.

III. MATERIALS RESEARCH

Measurements on thin-film resistors and n-channel MOSFETs fabricated in zone-melting-recrystallized Si films on SiO_2 -coated Si substrates have shown that the sub-grain boundaries in these films have very little effect on electron transport. Minority-carrier-generation lifetimes in the microsecond range have been measured in such films and in epitaxial Si layers grown by chemical vapor deposition on these films. These results indicate that Si-on-insulator structures prepared by zone-melting recrystallization and subsequent epitaxial growth are potentially useful for integrated circuit and bipolar device applications.

To study the relationship between the structure and electrical properties of semiconductor grain boundaries, a novel technique has been developed for preparing bicrystals with specified grain boundary structure by means of vapor-phase epitaxy. A series of GaAs bicrystals has been grown with (110) tilt boundaries differing only in the magnitude of the [110] rotation angle. Initial electrical measurements indicate that the height of the potential barrier associated with these boundaries varies systematically with the rotation angle.

IV. MICROELECTRONICS

By using a top-down, self-aligning process, a joint-gate, vertically stacked CMOS inverter has been fabricated in a multilayer substrate. The nMOS transistor was formed in a layer of laser-recrystallized CVD silicon, and the pMOS transistor in the underlying single-crystal silicon substrate. The low-frequency gain of the inverter was -12.5, and the rise and fall times were 2 μ s.

Oxygen reactive-ion etching has been used to form a reusable, polyimide membrane mask for the proton exposure of resists. Lines as small as 600 Å have been replicated in PMMA using membranes 1 to 2 μ m thick, a beam energy chosen so that the protons are stopped in the thick areas of the masks, and a dose of 2×10^{13} H^+ cm^{-2} .

A high-speed, CCD-based, two-dimensional correlation system has been built which correlates a 256 x 256-element signal with a 32 x 32-element reference in approximately 1 s; this corresponds to a computation rate of more than 100 million operations per second. The correlation is performed by two CCDs: a programmable transversal filter which performs a series of one-dimensional correlations, and an accumulating memory which sums these operations to form the two-dimensional correlation.

V. ANALOG DEVICE TECHNOLOGY

The performance limits of integrated optical spectrum analyzers have undergone a comprehensive analysis. Improvement in the Bragg cell bandwidth-efficiency product by up to an order of magnitude should be possible through the use of acoustic beam-steering or birefringent-diffraction techniques.

A superconductive convolver has been fabricated and tested in which a niobium-on-sapphire microstrip meander line provides electromagnetic delay for counter-propagating signal and reference waves. Capacitive taps along the delay path feed superconductive lead-niobium tunnel-junction mixers, and the local signal-reference products are summed spatially to form the desired

convolution. This technology should provide for programmable matched-filtering of waveforms of up to 10-GHz bandwidth and 100-ns duration.

A sliding-window spectrum analyzer consisting of twelve identical surface-acoustic-wave (SAW) chirp-Fourier transform circuits is under development to process twelve parallel-beam Doppler-shifted CW returns from an airborne infrared laser radar. Although not all the required reflective-array compressors have been fabricated, tests with existing compressors have shown that every system requirement has been met or exceeded, including an 84-kHz frequency resolution with 10-MHz analyzer bandwidth, >50 dB dynamic range, and sidelobes >25 dB down.

REPORTS ON SOLID STATE RESEARCH

15 November 1981 through 15 February 1982

PUBLISHED REPORTS

Journal Articles

<u>JA No.</u> 5172	A Theoretical Note on the Structural Features Observed in Pulsed Energy-Beam Crystallization	H.J. Zeiger M.J. Larsen B.J. Palm	Appl. Phys. Commun. <u>1</u> , 61 (1981), DTIC AD-A110706
5243	Ultrathin, High-Efficiency Solar Cells Made from GaAs Films Prepared by the CLEFT Process	C.O. Bozler R.W. McClelland J.C.C. Fan	IEEE Electron Device Lett. <u>EDL-2</u> , 203 (1981)
5244	Optical Reflectance Technique for Observations of Submonolayer Adsorbed Films	V. Daneu R.M. Osgood, Jr. D.J. Ehrlich	Opt. Lett. <u>6</u> , 563 (1981), DTIC AD-A113232
5246	Slider LPE of $Hg_{1-x}Cd_xTe$ Using Mercury Pressure Controlled Growth Solutions	T.C. Harman	J. Electron. Mater. <u>10</u> , 1069 (1981), DTIC AD-A107976/3
5249	Laser Microreaction for Deposition of Doped Silicon Films	D.J. Ehrlich R.M. Osgood, Jr. T.F. Deutsch	Appl. Phys. Lett. <u>39</u> , 957 (1981), DTIC AD-A113231
5263	Sub-Doppler Submillimeter Spectroscopy Using Molecular Beams	W.A.M. Blumberg D.D. Peck H.R. Fetterman	Appl. Phys. Lett. <u>39</u> , 857 (1981), DTIC AD-A113233
5276	n-Channel Deep-Depletion Metal-Oxide-Semiconductor Field-Effect Transistors Fabricated in Zone-Melting-Recrystallized Polycrystalline Si Films on SiO_2	B-Y. Tsaur M.W. Geis J.C.C. Fan D.J. Silversmith R.W. Mountain	Appl. Phys. Lett. <u>39</u> , 909 (1981), DTIC AD-A113234
5291	Electrical Properties of Laser Chemically Doped Silicon	T.F. Deutsch D.J. Ehrlich D.D. Rathman D.J. Silversmith R.M. Osgood, Jr.	Appl. Phys. Lett. <u>39</u> , 825 (1981), DTIC AD-A110715
5293	Infrared Laser Developments	A. Mooradian P.F. Moulton	Laser Focus <u>18</u> , 52 (1982)

Meeting Speeches

<u>MS No.</u> 5618	Lateral Growth of Single-Crystal InP Over Dielectric Films by Orientation-Dependent VPE	P. Vohl C.O. Bozler R.W. McClelland A. Chu A.J. Strauss	J. Cryst. Growth <u>56</u> , 410 (1982), DTIC AD-A113266
5653	Linewidth Characteristics of (GaAl)As Semiconductor Diode Lasers	A. Mooradian D. Welford M.W. Fleming	In <u>Laser Spectroscopy V</u> , edited by A.R.W. McKellar, T. Oka, and B.P. Stoicheff (Springer-Verlag, New York, 1981), p. 67
5720	Laser-Photochemical Techniques for VLSI Processing	D.J. Silversmith D.J. Ehrlich R.M. Osgood T.F. Deutsch	1981 Symposium on VLSI Technology, Maui, Hawaii, 9-11 September 1981, Digest of Technical Papers, pp. 70-71
5745	New Techniques and Applications for High Resolution Tunable Submillimeter Spectroscopy	H.R. Fetterman W.A.M. Blumberg	In <u>Laser Spectroscopy V</u> , edited by A.R.W. McKellar, T. Oka, and B.P. Stoicheff (Springer-Verlag, New York, 1981), p. 76
5797	Vertical Single-Gate CMOS Inverters on Laser-Processed Multilayer Substrates	G.T. Goeloe E.W. Maby* D.J. Silversmith R.W. Mountain D.A. Antoniadis*	Proc. IEEE Intl. Electron Devices Mtg., Washington, DC, 7-9 December 1981, pp. 554-556
5803	Stress-Enhanced Mobility in MOSFETs Fabricated in Zone-Melting-Recrystallized Poly-Si Films	B-Y. Tsaur J.C.C. Fan M.W. Geis D.J. Silversmith R.W. Mountain	Proc. IEEE Intl. Electron Devices Mtg., Washington, DC, 7-9 December 1981, pp. 232-235

* * * * *

UNPUBLISHED REPORTS

Journal Articles

<u>JA No.</u> 5250	A Calculation of the Capacitance-Voltage Characteristics of p ⁺ -InP/n-InP/n-InGaAsP Photodiodes	J.P. Donnelly	Accepted by Solid-State Electron.
5277	Efficient Raman Frequency Conversion in Liquid Nitrogen	S.R.J. Brueck H. Kildal	Accepted by IEEE J. Quantum Electron.

*Author not at Lincoln Laboratory.

JA No. 5282	Stress-Enhanced Carrier Mobility in Zone-Melt g-Recrystallized Polycrystalline Si Films on SiO ₂ -Coated Substrates	B-Y. Tsaur J.C.C. Fan M.W. Geis	Accepted by Appl. Phys. Lett.
5283	Localized Laser Etching of Compound Semiconductors in Aqueous Solution	R.M. Osgood, Jr. A. Sanchez-Rubio D.J. Ehrlich V. Daneu	Accepted by Appl. Phys. Lett.
5305	Amorphous-Crystalline Boundary Dynamics in Laser Crystallization	H.J. Zeiger J.C.C. Fan B.J. Palm R.L. Chapman R.P. Gale	Accepted by Phys. Rev. B
5308	Applications of Guided-Wave Interferometers	F.J. Leonberger	Accepted by Laser Focus
5312	4-Bit 828-Megasample/sec Electrooptic Guided-Wave Analog-to-Digital Converter	F.J. Leonberger C.E. Woodward R.A. Becker	Accepted by Appl. Phys. Lett.
5318	A Novel Technique for GaInAsP/InP Buried Heterostructure Laser Fabrication	Z.L. Liao J.N. Walpole	Accepted by Appl. Phys. Lett.
5320	Observation of Linewidth Broadening in (GaAl)As Diode Lasers Due to Electron Number Fluctuations	D. Welford A. Mooradian	Accepted by Appl. Phys. Lett.
5326	Efficient GaAs Solar Cells Formed by UV Laser Chemical Doping	T.F. Deutsch J.C.C. Fan D.J. Ehrlich G.W. Turner R.L. Chapman R.P. Gale	Accepted by Appl. Phys. Lett.
MS-5748	Oxide Barriers to Formation of Refractory Silicides	D.J. Silversmith D.D. Rathman R.W. Mountain	Accepted by Thin Solid Films
MS-5765	Ion Beam Assisted Etching for GaAs Device Applications	G.A. Lincoln M.W. Geis L.J. Mahoney B.A. Vojak K.B. Nichols W.J. Piacentini N. Efremow W.T. Lindley	Accepted by J. Vac. Sci. Technol.
MS-5871	Picosecond InP Optoelectronic Switches	A.G. Foyt F.J. Leonberger R.C. Williamson	Accepted by Appl. Phys. Lett.

Meeting Speeches*

MS No. 5607C	Pulsed Laser Processing of Semiconductors	T.F. Deutsch D.J. Ehrlich	12th Winter Colloquium on Quantum Electronics, Snowbird, Utah, 13-15 January 1982
5609B	Advances in Divalent Transition-Metal Lasers	P.F. Moulton	Lasers '81, New Orleans, Louisiana, 14-18 December 1981
5806	Some Surprising Results in Studies of Transition-Metal-Doped Crystals	P.F. Moulton	
5717D	Preparation of High-Quality Silicon Films on Insulators by Zone-Melting Recrystallization	J.C.C. Fan	Seminar, University of California, Berkeley, 19 November 1981
5748	Oxide Barriers to Formation of Refractory Silicides	D.J. Silversmith D.D. Rathman R.W. Mountain	Materials Research Society Conf., Boston, 16-19 November 1981
5760	Transient Heating with Graphite Heaters for Semiconductor Processing	J.C.C. Fan B-Y. Tsaur M.W. Geis	
5763	Preparation of Oriented GaAs Bicrystal Layers by Vapor-Phase Epitaxy Using Lateral Overgrowth	J.P. Salerno R.W. McClelland P. Vohl J.C.C. Fan W. Macropoulos C.O. Bozler A.F. Witt†	
5766	Effects of Interface Structure on the Electrical Characteristics of PtSi-Si Schottky Barrier Contacts	B-Y. Tsaur D.J. Silversmith R.W. Mountain C.H. Anderson, Jr.	
5767	Silicon-on-Insulator MOSFETs on Zone-Melting-Recrystallized Poly-Si Films on SiO ₂	B-Y. Tsaur M.W. Geis J.C.C. Fan D.J. Silversmith R.W. Mountain	

*Titles of Meeting Speeches are listed for information only. No copies are available for distribution.

†Author not at Lincoln Laboratory.

MS No. 5803A	Effect of Thermal Stress on the Carrier Mobility in Zone-Melting-Recrystallized Films on SiO ₂ -Coated Substrates	B-Y. Tsaur J.C.C. Fan M.W. Geis D.J. Silversmith R.W. Mountain	Materials Research Society Conf., Boston, 16-19 November 1981
5868	Crystallographic Characteristics of Si Films Recrystallized by Zone Melting	M.W. Geis H.I. Smith* B-Y. Tsaur J.C.C. Fan	
5765	Ion Beam Assisted Etching for GaAs Device Applications	G.A. Lincoln M.W. Geis L.J. Mahoney B.A. Vojak K.B. Nichols W.J. Piacentini N. Efremow W.T. Lindley	28th National AVS Symposium, Anaheim, California, 3-6 November 1981
5768	Applications of Scanning Electron Beam Lithography	T.M. Lyszczarz	Electron Beam Lithography for Microstructures Device Manufacture Mtg., Carmel, California, 1-3 November 1981
5826	Single-Mode GaInAsP Optical Waveguides	N.L. DeMeo F.J. Leonberger S.H. Groves	Sixth Topical Meeting on Integrated and Guided-Wave Optics, Pacific Grove, California, 6-8 January 1982
5835	Design Rules for Low-Loss Coherently-Coupled LiNbO ₃ Waveguide Bends	L.M. Johnson F.J. Leonberger	
5840	GaInAsP/InP Double Heterostructure Laser with Monolithically Integrated Passive Waveguide	Z.L. Liao J.N. Walpole	
5845	4-Bit 275-MS/s Electrooptic A/D Converter	F.J. Leonberger C.E. Woodward R.A. Becker	
5846	External Cavity Controlled Operation of a Semiconductor Diode Gain Element in Series with an Optical Fiber	R.H. Rediker R.P. Schloss A. Mooradian D. Welford	
5842	Considerations for an Integrated Optical Spectrum Analyzer	P.V. Wright	IEEE Sonics and Ultrasonics Chapter Mtg., Sudbury, Massachusetts, 18 November 1981

*Author not at Lincoln Laboratory.

MS No.
5854

Guided-Wave Electrooptic
Modulators

F.J. Leonberger

Conf. on Fiberoptic
Rotation Sensors, M.I.T.,
10 November 1981

5862

Receiver Technology for the
Millimeter and Submillimeter
Wave Regions

B.J. Clifton

SPIE Mtg. on Integrated
Optics and Millimeter
and Microwave Integrated
Circuits, Huntsville,
Alabama, 16-19 November 1981

5887

Three-Terminal Device Used
for Optical Heterodyning at
Submillimeter IFs

H.R. Fetterman
D.D. Peck
A. Chu
P.E. Tannenwald

1981 IEEE Intl. Conf. on
Infrared and Millimeter
Waves, Miami Beach,
7-12 December 1981

ORGANIZATION

SOLID STATE DIVISION

A.L. McWhorter, Head
I. Melngailis, Associate Head
J.F. Goodwin, Assistant

P.E. Tannenwald, Senior Staff

QUANTUM ELECTRONICS

A. Mooradian, Leader
P.L. Kelley, Associate Leader

Barch, W.E.	Hancock, R.C.
Belanger, L.J.	Johnson, B.C.*
Brueck, S.R.J.	Killinger, D.K.
Burke, J.W.	Lenth, W.
Bushee, J.F.	Lewis, R.C.*
Coulombe, M.J.	Menyuk, N.
Daneu, V.	Moulton, P.F.
DeFeo, W.E.	Murphy, D.V.
Deutsch, T.F.	Parker, C.D.
Ehrlich, D.J.	Peck, D.D.
Feldman, B.	Sullivan, D.J.
Fetterman, H.R.	Tsao, J.Y.
Goodhue, W.D.*	Welford, D.

ELECTRONIC MATERIALS

A.J. Strauss, Leader
J.C.C. Fan, Assistant Leader
J.G. Mavroides, Senior Staff
H.J. Zeiger, Senior Staff

Anderson, C.H., Jr.	Mastromattei, E.L.
Button, M.J.	Metze, G.M.
Chapman, R.L.	Nitishin, P.M.
Davis, F.M.	Owens, E.B.
Delaney, E.J.	Palm, B.J.
Fahey, R.E.	Pantano, J.V.
Finn, M.C.	Salerno, J.P.*
Foley, G.H.	Tracy, D.M.
Gale, R.P.	Tsaur, B-Y.
Iseler, G.W.	Turner, G.W.
Kolesar, D.F.	Vohl, P.
Krohn, L., Jr.	

APPLIED PHYSICS

R.C. Williamson, Leader
C.E. Hurwitz, Associate Leader
F.J. Leonberger, Assistant Leader
T.C. Harman, Senior Staff
R.H. Kingston, Senior Staff
R.H. Rediker, Senior Staff

Armiento, C.A.*	Foyt, A.G.	O'Donnell, F.J.
Becker, R.A.	Groves, S.H.	Orr, L.*
Calawa, A.R.	Hovey, D.L.	Paladino, A.E.
Carter, F.B.	Johnson, L.M.	Plonko, M.C.
Chinnock, C.B.	Lattes, A.L.*	Schloss, R.P.*
DeMeo, N.L., Jr.	Liau, Z.L.	Spears, D.L.
Diadiuk, V.	Lind, T.A.	Tsang, D.Z.
Donnelly, J.P.	Manfra, M.J.	Walpole, J.N.
Ferrante, G.A.	McBride, W.F.	Woodhouse, J.D.

*Research Assistant

ANALOG DEVICE TECHNOLOGY

E. Stern, Leader
J.H. Cafarella, Assistant Leader
R.W. Ralston, Assistant Leader

Anderson, A.C.	Flynn, G.T.	Oates, D.E.
Arsenault, D.R.	Holtham, J.H.	Reible, S.A.
Baker, R.P.	Kernan, W.C.	Sage, J.P.
Behrmann, G.J.	Leung, I.	Slattery, R.L.
Brogan, W.T.	Lowney, S.D.	Withers, R.S.
DiPerna, M.S.*	Lynch, J.T.*	Wright, P.V.
Dolat, V.S.	Macedo, E.M., Jr.	Yao, I.
Fischer, J.H.	Macropoulos, W.	
Fitch, G.L.†	Melngailis, J.*	

MICROELECTRONICS

W.T. Lindley, Leader
F.J. Bachner, Associate Leader
N.P. Economou, Assistant Leader
R.A. Murphy, Assistant Leader

Alley, G.D.	Felton, B.J.	Nichols, K.B.
Bozler, C.O.	Flanders, D.C.	Pang, S.W.
Bromley, E.I.	Geis, M.W.	Piacentini, W.J.
Burke, B.E.	Goeloe, G.T.§	Pichler, H.H.
Cabral, S.M.	Gray, R.V.	Rabe, S.*
Chiang, A.M.	Hansell, G.L.¶	Randall, J.N.
Chu, A.	Lincoln, G.A., Jr.	Rathman, D.D.
Clifton, B.J.	Lyszcza, T.M.	Shaver, D.C.
Daniels, P.J.	Mahoney, L.J.	Silversmith, D.J.
DeGraff, P.D.	McClelland, R.W.	Smythe, D.L., Jr.
Durant, G.L.	McGonagle, W.H.	Vigilante, J.L.
Efremow, N.N., Jr.	Mountain, R.W.	Vojak, B.A.
Elta, M.E.	Mroczkowski, I.H.	Wilde, R.E.

*Part Time

†Co-op Student

§Staff Associate

¶Research Assistant

I. SOLID STATE DEVICE RESEARCH

A. PICOSECOND InP OPTOELECTRONIC SWITCHES

Proton bombardment has been used to reduce the response times of InP optoelectronic switches from a few nanoseconds to less than 100 ps. The electron mobility in these bombarded devices can be greater than $600 \text{ cm}^2/\text{V-s}$, which is over an order-of-magnitude larger than that of devices of comparable speed made on other high-resistivity materials. This relatively large mobility implies that, with similar structures and bias levels, the InP devices should have over an order-of-magnitude larger conductance for a given light level. Also, a comparison of the characteristics of these new switches to those of the previously reported InP devices¹ has been made.

Devices were fabricated on slices of semi-insulating InP which had a resistivity of $\sim 5 \times 10^7 \Omega\text{-cm}$ and a bulk mobility of ~ 2500 to $3500 \text{ cm}^2/\text{V-s}$. Following conventional polishing and etching procedures, interdigitated-finger electrode structures of Au/Ge/Ni were applied to the InP using vacuum evaporation and lift-off lithography. The devices investigated had 2- μm -wide fingers and spaces with an overall active area of $48 \times 48 \mu\text{m}$, as illustrated in Fig. I-1.

After the electrodes has been patterned, the slice for the first set of experiments was cleaved into five separate pieces, with each piece having several devices of the 2- μm geometry. Each piece was covered with pyrolytic phosphosilicate glass (PSG) and annealed at 450°C for 10 s. The glass was then removed, one piece set aside as a standard, and the remaining four were bombarded with a 10^{13} cm^{-2} dose of 200-keV protons. Next, three of these samples were annealed for 10 s in hydrogen at 250°C , 300°C , and 350°C , respectively. Each sample was then cemented to a grooved aluminum block and wire bonded to OSM connectors for evaluation.

Preliminary low-speed measurements were done by means of a raster-scanned He-Ne laser light spot to insure that these devices had the uniformity of photoresponse, linearity of current-voltage characteristics, and the near-theoretical sensitivity of earlier devices.^{2,3} For the high-speed

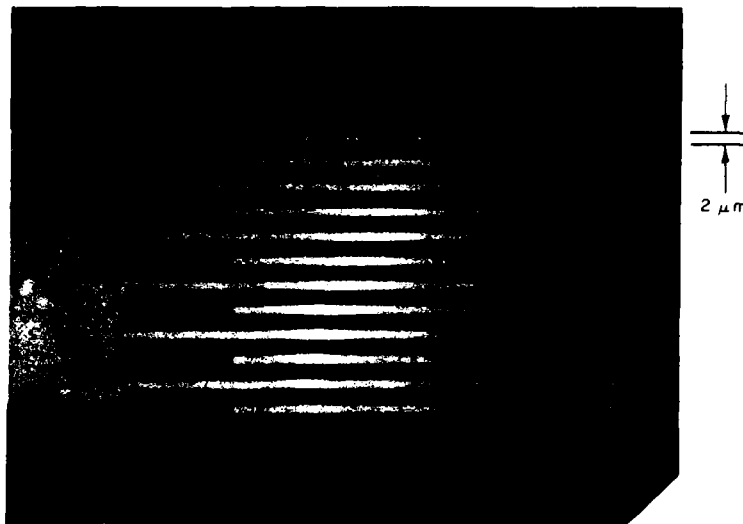


Fig. I-1. Photograph of InP optoelectronic switch. Interdigital electrode lines and spaces are $2\text{ }\mu\text{m}$ wide, and overall active area is $48 \times 48\text{ }\mu\text{m}$.

photoresponse measurements, a commercial low-threshold AlGaAs diode laser ($\lambda \sim 0.85\text{ }\mu\text{m}$) driven by a commercial impulse train generator⁴ was used as a pulsed light source. The light pulses had a repetition rate of 100 MHz and a full width at half maximum (FWHM) of $\leq 100\text{ ps}$, as measured by an InP/GaInAsP/InP n^+-n-p^+ photodiode fabricated at Lincoln Laboratory. The peak optical power focused on the device was estimated to be 3 mW. The pulse measurements described below were made by applying a DC voltage of 300 mV to one side of the switch and connecting the output to a $50\text{-}\Omega$ sampling oscilloscope.

The results for the InP devices are shown in Figs. I-2(a-b) and I-3(a-c). For the unbombarded device, the decay of the photoresponse is approximately exponential with 90-to-10-percent fall time of $\sim 5\text{ ns}$ (time constant of $\sim 2.3\text{ ns}$). Also, from a previous study of device resistance as a



Fig. I-2. Photoreponse of InP optoelectronic switches to short pulses (<100 ps) of AlGaAs diode-laser light ($\lambda \sim 0.85 \mu\text{m}$) of 3-mW peak power. In this test, a DC voltage of 300 mV was connected between ground and one terminal of device, with response shown observed between other terminal and ground on a high-speed sampling oscilloscope (response time ~ 25 ps). (a) Unbombed device, (b) device bombarded with a 10^{13} cm^{-2} dose of 200-keV protons and subsequently annealed at 250°C for 10 s.

function of finger geometry, the electron mobility is estimated to be $\sim 2000 \text{ cm}^2/\text{V}\cdot\text{s}$. Following bombardment, both the response time and mobility are substantially reduced, with the rise and fall times each <100 ps and electron mobility of $\sim 200 \text{ cm}^2/\text{V}\cdot\text{s}$. Subsequent to bombardment and the 250°C anneal, the rise and fall times remained at <100 ps, but the mobility

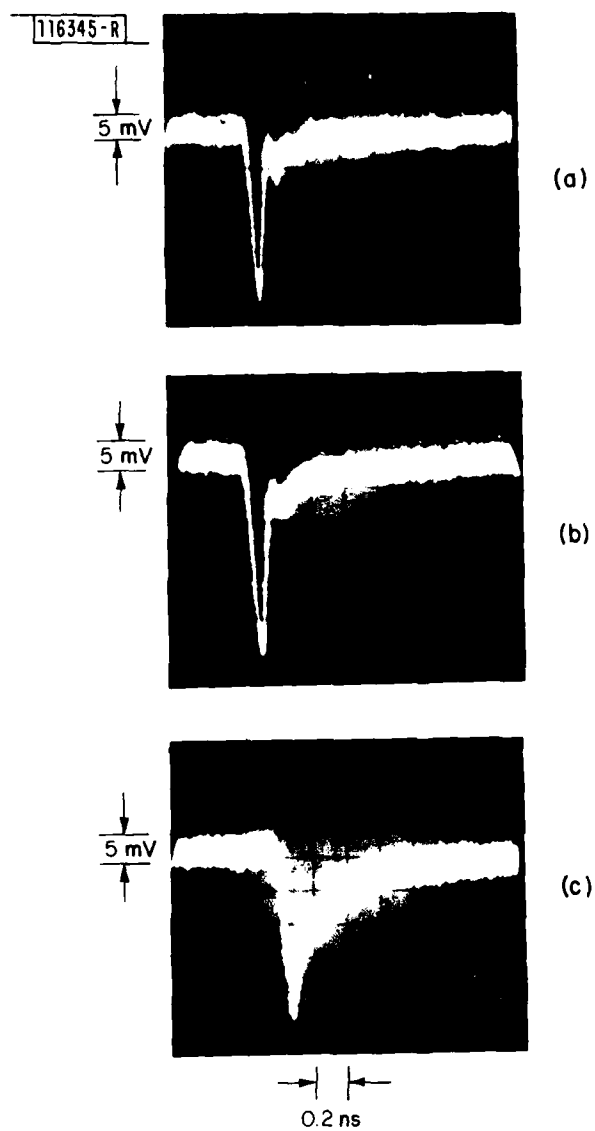


Fig. I-3. Photoresponse of three InP optoelectronic switches, as described in Fig. I-2(a-b), following proton bombardment and subsequent 10-s anneal at (a) 250°C, (b) 300°C, and (c) 350°C.

recovered to at least $1000 \text{ cm}^2/\text{V-s}$. The mobility recovery was estimated by the amplitude of the photoresponse compared with that of the unbombarded device. In making the calculation, the photoconductive lifetime was determined from the measurement shown, and the electron mobility for the unbombarded sample was calculated from the measured DC photoconductance G_{dc} . Here, $G_{dc} = \mu \tau I_{dc} \eta$, where μ is the electron mobility, τ is the photoconductance lifetime, I_{dc} is the absorbed optical intensity, and η is a calculated constant that includes the geometric factors. For the response to a pulse $I(t)$, it was assumed that the photocarriers were generated in a time short compared with τ , so that the photoconductance becomes

$$G(t) = G_0 e^{-t/\tau}$$

where $G_0 = \mu \eta \int I dt$. Thus, G_0 is linearly proportional to electron mobility and independent of lifetime. It should be noted that this measurement may underestimate the mobility value because of carrier recombination during the light pulse.

With the increasing anneal temperature, the rise and fall times remain at $<100 \text{ ps}$, and the mobility remains at $>1000 \text{ cm}^2/\text{V-s}$. However, the bombarded devices show a small "back porch" on the trailing edge of the response. This back-porch component increases in magnitude as the device is annealed toward its unbombarded state. The shape of these pulses was insensitive to focusing and total light incident on the device.

The samples for the second set of experiments were processed in an identical manner as those for the first set, except for the bombardment. In this case, a schedule of 10^{13} cm^{-2} protons at each of three energies (100, 200, and 300 keV) was used to provide a more nearly uniform depth distribution of bombardment effects. The results were similar to those of the first experiments, except for a substantially reduced "back porch." Figure I-4 shows the response of the sample prepared in this way and annealed at 250°C for 10 s. It is clear that the trailing edge is much sharper than that seen in Fig. I-3(a), with a FWHM of 70 ps. However, package resonance effects limit our ability to interpret the trailing edge, and improved packages are in progress. As for the first experiment, the estimated mobility of $>600 \text{ cm}^2/\text{V-s}$ must be regarded as a lower limit due to carrier recombination during the light pulse.

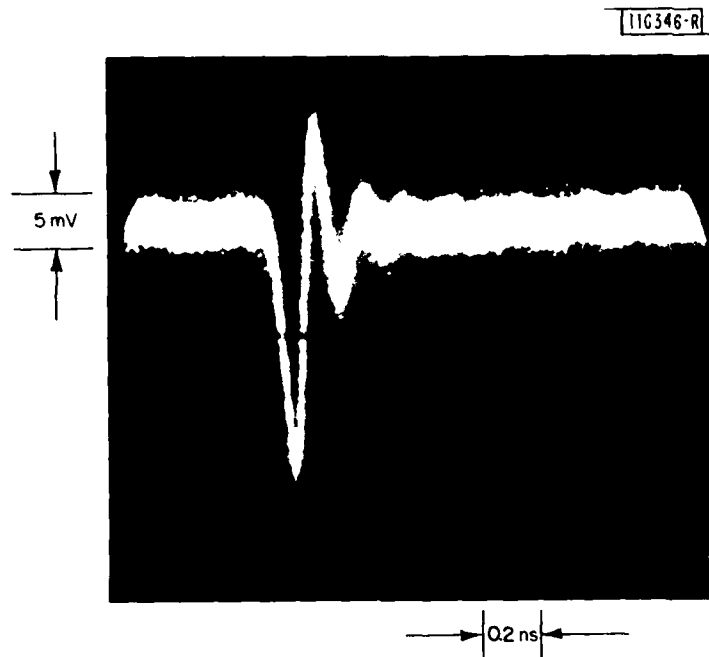


Fig. I-4. Photoresponse of an InP optoelectronic switch as in Fig. I-2(b), except that DC voltage was 500 mV and device was bombarded with 10^{13} cm^{-2} protons at 100, 200, and 300 keV, respectively, and subsequently annealed at 250°C for 10 s.

Another effect of the bombardment that may be a limitation in some cases is a decrease in the off-state (dark) resistance. For the device of the second experiment that was bombarded and annealed at 250°C , the off-state resistance decreased from $>10 \text{ M}\Omega$ to $\sim 100 \text{ k}\Omega$. This value can be compared with the on-state value of $\sim 1000 \Omega$ in the present experiment, and an anticipated value of $<100 \Omega$ when the laser is replaced with one having greater output power. However, the off-state resistance decrease may not be a necessary result of proton bombardment, and more work with different bombardment and anneal schedules (and perhaps with other ions) is needed to investigate this effect. Also, since higher proton doses have been shown to increase absorption below the band edge,⁵ it may be possible to extend the wavelength sensitivity of these devices to $>1 \mu\text{m}$.

The present results can be compared with the earlier fast InP optoelectronic switches.¹ Those devices were fabricated on InP slices similar to

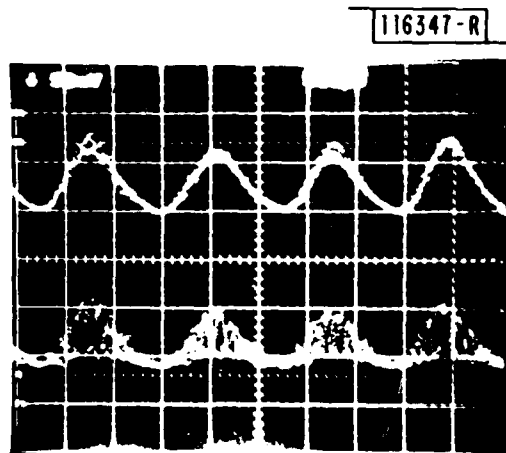
those used here, but the metallization was vacuum-evaporated gold that was patterned by means of conventional photolithography and wet chemical etching to yield a 30- μm -wide microstrip line with a 3- μm gap in the middle of its length. This device had a 1- to 2-ns response time as originally fabricated. However, by using a short anneal (~ 5 s) in hydrogen at 400°C, it was possible to reproducibly reduce this response time to ~ 50 ps. In both the large- and small-time-constant states, the conductance of these devices was about one-tenth of that expected for the measured values of time constant, bulk mobility, and light level, with the lower conductance probably due to contact resistance and/or surface effects. It is also worth noting that the annealing temperature that resulted in faster response also is the temperature at which P outdiffusion begins to occur. Our attempts to apply this technique to the present alloyed-contact higher-response devices have not been successful. The current devices have, in addition to their substantially lower contact resistance, minimal photovoltaic effects, suggesting that the fast response of earlier devices may be associated with photovoltaic effects. Because of the greater sensitivity of devices made using the bombardment technique, we are currently pursuing it instead of further research on the heat-treatment technique.

In summary, InP optoelectronic switches have been fabricated which have fast response times (< 100 ps) and high electron mobility (> 600 $\text{cm}^2/\text{V}\cdot\text{s}$) following proton bombardment and anneal. Work is currently in progress to optimize response time and mobility while minimizing the off-state conductance.

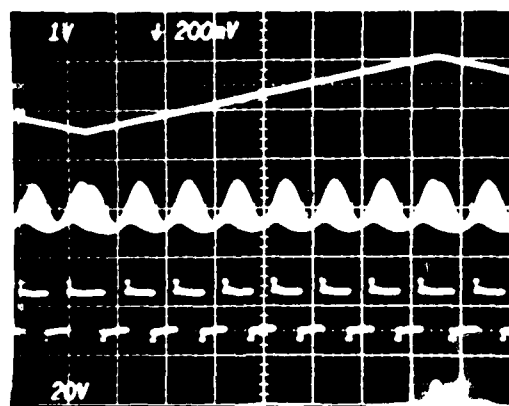
A.G. Foyt R.C. Williamson
F.J. Leonberger G.W. Iseler

B. 4-BIT 828-MS/s GUIDED-WAVE ELECTROOPTIC ANALOG-TO-DIGITAL CONVERTER

We previously reported results on a 4-bit LiNbO_3 guided-wave electrooptic A/D converter, including the operation of individual bit channels at 276 MS/s (see Ref. 6). Here we report the extension of that work to 828 MS/s, including beat-frequency tests with a 413-MHz analog test signal.



(a)



(b)

Fig. I-5. (a) Unmodulated (top trace) and modulated (bottom trace) comparator inputs at 828 MHz. The 200-ps-wide mode-locked optical pulses are broadened by Ge APD and amplifier. (b) A/D converter response to ramp analog test signal at an 828-MHz sampling rate. Upper trace is ramp signal, middle trace is detector output, and lower trace is comparator output.

To obtain the 828-MS/s rate, the output pulses from the mode-locked Nd:YAG laser used in the previous work were time multiplexed using beam splitters and differential time delay. Figure I-5(a) shows a sampling-oscilloscope photograph of the unmodulated signal pulses after passing through the post-detector amplifier, and the same pulses when a ramp analog test signal was applied to the modulator. The pulse envelope appears filled-in because the test signal was not synchronized with the sampling pulses. The slight variations in pulse height were due to alignment effects of the three multiplexed optical beams. Figure I-5(b) shows the ramp test signal, the real-time-detected sinusoidal pulse envelope, and the comparator outputs for the LSB modulator. In this case the comparator utilized a DC reference. Results for other modulators had the expected sinusoidal envelopes. It is important to note that the comparator is a latch-type device, and so, even though it is toggling at a relatively low speed in response to the ramp, comparisons are being made at an 828-MHz rate.

To further demonstrate the high-speed operation of the A/D converter, a beat-frequency test was performed at 828 MS/s. This is a standard test used on conventional high-speed A/Ds which allows the maximum-frequency input signals to be applied while the device output is monitored at a relatively low frequency. A sinusoidal test signal whose frequency was 1 MHz less than one-half the mode-locked sampling pulse rate was applied to the device. Each successive sample of the analog-test signal was thus of opposite polarity (i.e., differing by slightly less than π radians), and every other sample differed slightly in phase. The serial-to-parallel converter following the comparator was activated on every eighth pulse, and only one of the parallel channels was monitored. This mode of comparator operation ensured that the oscilloscope display truly represented signals from each of the three multiplexed pulse trains.

Figure I-6 is an oscillogram showing the results of the beat-frequency test at 828 MS/s. The upper trace is a 1-MHz signal, which was derived by mixing the 413-MHz analog-test signal with a 414-MHz signal derived by detecting the 828-MHz laser pulses, dividing the pulse rate by 2, and

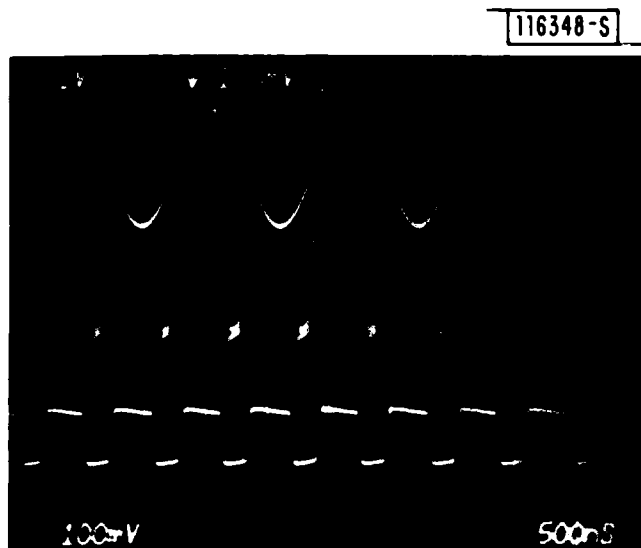


Fig. I-6. Beat-frequency test of electrooptic A/D converter. Input RF test signal is at 413 MHz, sampling is at 828 MHz. Shown from top to bottom in oscillogram are a simulated beat signal, detector output, and comparator output. Phase of beat signal has not been synchronized to that of detector and comparator.

filtering to obtain the 414-MHz fundamental. The 1-MHz signal was used to trigger the oscilloscope. The middle trace shows the detector output. The envelope of these detected pulses has the expected FM modulated form, and its exact shape depends on the peak amplitude of the 413-MHz test signal. In the case shown, the input signal is 10 dBm or $\sim 0.95 V_{\pi}$. The lower trace shows the corresponding comparator outputs. The comparator is again functioning at 828 MS/s. Outputs from the other 3-bit channels were as expected. Further development and testing of this converter are in progress.

F.J. Leonberger
C.E. Woodward
R.A. Becker

C. A NOVEL TECHNIQUE FOR GaInAsP/InP BURIED HETEROSTRUCTURE LASER FABRICATION

A novel technique for the fabrication of GaInAsP/InP buried heterostructure (BH) lasers has been developed. It is based on a mass-transport phenomenon which was recently observed during the fabrication of integrated laser-waveguide structures.⁷ This technique is considerably simpler and more easily controlled than previously reported ones,⁸⁻²¹ and has resulted in BH lasers with threshold currents as low as 9.0 mA.

The experimental procedure is illustrated in Fig. I-7(a-c). The starting wafer was a double-heterostructure (DH) one, prepared by conventional liquid-phase-epitaxial (LPE) techniques on a (100) InP substrate. (Broad-area lasers fabricated from similar wafers have had threshold current densities of 0.9 to 1.3 kA/cm².) Oxide-stripe masks 5.0 to 6.0 μ m wide on 250- μ m centers were first fabricated on the wafer, with the stripes parallel to either (011) or (0 $\bar{1}\bar{1}$) crystallographic directions. Two steps of selective chemical etching were used in order to produce the mesa structure shown in Fig. I-7(b). First, concentrated HCl was used to remove the unprotected InP cap layer. The Ga_{0.27}In_{0.73}As_{0.63}P_{0.37} active layer thus exposed was then removed with a 50-ml aqueous solution of 10 g KOH and 0.2 g K₃Fe(CN)₆. Additional etching, beyond that required to remove the quaternary layer, was sometimes used, depending on the desired amount of undercutting [Fig. I-7(b)].

After completion of the etching steps, the wafer was heat treated in the following manner which had previously been found⁷ to cause a migration of InP, and which resulted in a BH as illustrated in Fig. I-7(c). The wafer was dipped in buffered HF for 1 min. and loaded into an LPE system with a freshly baked graphite slider, but without any growth solution. The wafer was placed in a shallow slot on the graphite slider and was covered by a graphite plate. The system was purged with H₂ and PH₃ while being heated to 670°C. The H₂- and PH₃-flow rates were chosen so that almost no surface changes were observed on plain InP substrates (except for regions near the edges) under the heating cycle used in the present work. The system reached 670°C in

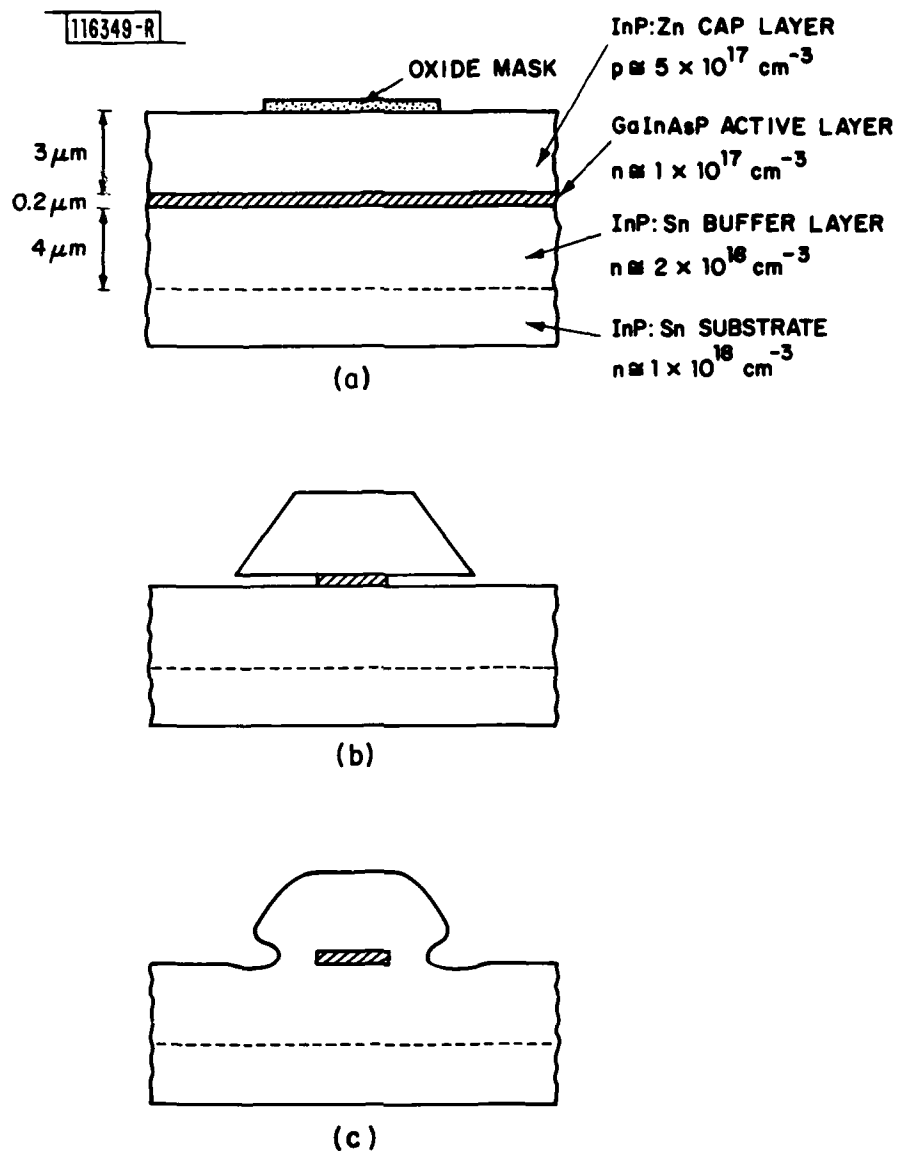
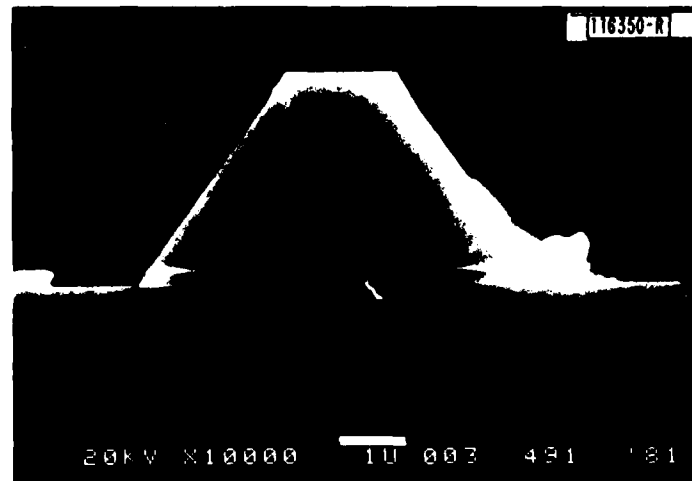


Fig. I-7. Schematic pictures showing mesa etching and mass-transport phenomenon which result in BH. Transport of InP has been observed after heat treatment at 670°C in H_2 and PH_3 atmosphere. (a) DH laser wafer, (b) selective chemical etching, and (c) transport of InP.

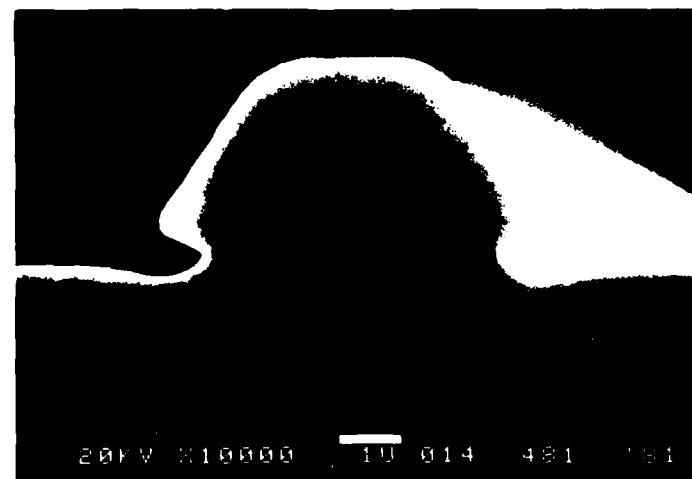
approximately 30 min. and stayed at that temperature for another 30 min. before being rapidly cooled.

Figure I-8(a-b) shows scanning electron microscope (SEM) photographs of cleaved and stained cross sections of two different wafers, one before and the other after being heat treated in the LPE system. In (a) the undercut in the quaternary etching was $2.2\text{ }\mu\text{m}$ from each side, leaving a neck-shaped quaternary region of $1.0\text{-}\mu\text{m}$ width. In some wafers, GaInAsP strips as narrow as $0.3\text{ }\mu\text{m}$ were obtained. A comparison of (a) and (b) shows that the heat treatment resulted in a marked change in the mesa shape. The corners were eroded, while the narrow undercut channels were filled-in with InP. This phenomenon, apparently a transport of InP, has been reproducibly observed in 25 runs of similar experiments, with the notable exception of one in which the PH_3 flow was not used. The transported InP was generally symmetrical on the two sides of a mesa and was uniform for different mesas on the same wafer. The width of the InP varied between 0.5 and $2.0\text{ }\mu\text{m}$, depending mainly on the amount of undercut. The recess at the base of the final mesa evident in Fig. I-8(b) was reduced (or totally eliminated) with a smaller initial undercut. Mesa tops which were initially narrower than roughly $2\text{ }\mu\text{m}$ were completely rounded after the heat treatment, whereas those which were wider retained a flat top as in Fig. I-8(b).

The resulting structure, which consists of a GaInAsP strip completely surrounded by InP, is ideally suited for the fabrication of a BH laser. To complete the processing, the wafer was first coated with oxide and patterned with openings on the mesa tops. After a zinc skin-diffusion through the openings in the oxide, Au-Zn alloyed contacts were made to the p^+ -InP. The wafer was then lapped from the substrate side to a thickness of $100\text{ }\mu\text{m}$, after which a Au-Sn alloyed contact was applied. Next, Ti ($200\text{ }\text{\AA}$) and Au ($500\text{ }\text{\AA}$) layers were sputter-deposited over the entire wafer on the mesa side to facilitate contacting. Individual BH lasers were then obtained by cleaving and saw-cutting.



(a)



(b)

Fig. I-8. SEM micrographs showing chemically etched mesas (a) before and (b) after transport of InP. Mesa in (a) is from a bar cleaved off Wafer 491, which had a narrow (1.6 μm) mesa top, while that in (b) is from Wafer 481, for which the mesa top was wider ($\sim 2.8 \mu\text{m}$). (See Table I-1.) These cleaved facets have been stained [more heavily in (b)] in order to bring out contrast between GaInAsP and InP.

TABLE I-1
SOME PROPERTIES OF THE GaInAsP/InP BH LASERS
FABRICATED BY THE TRANSPORT OF InP

Wafer	Active Region Widths (μm)	Lowest Threshold Current (mA)	Device Length (μm)
475	3.9 to 4.5	33.0	406
476	1.8 to 2.5	20.0	254
481	0.7 to 1.4	13.8	305
489	0.7 to 1.5	9.0	279
491	1.0 to 2.2	58.0	254
513	3.0 to 3.6	17.0	279

Six wafers have been processed for BH lasers. The active region widths of each wafer shown in Table I-1 were obtained by measurements of mesas on a bar cleaved from one edge of that wafer. The BH lasers were tested in room-temperature pulsed operation with the lowest threshold currents shown in Table I-1. The yields of low-threshold devices in the first five wafers were only modest. A marked improvement was observed in the sixth wafer in which approximately 60 percent of the devices showed normal I-V characteristics and very consistent threshold currents (17 to 19 mA). This improvement was related to a special mesa structure used in this particular wafer: most areas of the wafer were protected by oxide-masks during the selective chemical etching except for stripe regions of 10- μm width on the two sides of each laser mesa. These unetched areas are expected to provide better support and protection for the laser mesas.

The lowest threshold current obtained to date was 9.0 mA. Further reduction could well be achieved by using shorter devices and narrower active regions. Nevertheless, the present low thresholds are already comparable to or better than those obtained by more conventional fabrication techniques,⁸⁻²¹ for which the lowest reported value was 10 mA (Ref. 21). It

is important to note that the new technique described here is considerably simpler than those reported previously, since it eliminates the need for the LPE regrowth of burying layers. The latter not only requires all the special precautions for LPE regrowth, but also demands critical control of layer thicknesses in order to reduce leakage current. In the present structure, the burying sidewalls of transported InP are just wide enough to provide mode confinement, but narrow enough to minimize current leakage. Moreover, the InP transport has been found to be very reproducible and easily controlled.

With respect to the transport of InP, the driving force for the phenomenon is probably a surface-energy minimization. It is also likely that the presence of the PH_3 plays an important role in the transport process. However, detailed study of the transport kinetics has not yet been attempted, and the experimental parameters used in the present work were those for which the process was first observed. To our knowledge, this is a novel phenomenon and may find other applications in device fabrication.

Z.L. Liao
J.N. Walpole

REFERENCES

1. F.J. Leonberger and P.F. Moulton, Appl. Phys. Lett. 35, 712 (1979), DDC AD-A085785/4; Solid State Research Report, Lincoln Laboratory, M.I.T. (1979:4), p.1, DDC AD-A084271/6.
2. A.G. Foyt, F.J. Leonberger, and R.C. Williamson, Proc. SPIE Vol.269: Integrated Optics (Society of Photo-Optical Instrumentation Engineers, Bellingham, Washington, 1981), pp.109-114, DTIC AD-A108854/1; Solid State Research Report, Lincoln Laboratory, M.I.T. (1981:2), p.3, DTIC AD-A110947.
3. A.G. Foyt, F.J. Leonberger, and R.C. Williamson, IEEE Trans. Electron. Devices ED-28, 1214 (1981) (Abstract).
4. K.Y. Lau and A. Yariv, Opt. Commun. 35, 337 (1980).

5. F.J. Leonberger, J.N. Walpole, and J.P. Donnelly, IEEE J. Quantum Electron. QE-17, 830 (1981), DTIC AD-A105372; Solid State Research Report, Lincoln Laboratory, M.I.T. (1981:1), p.1, DTIC AD-A103887/6.
6. Solid State Research Report, Lincoln Laboratory, M.I.T. (1981:4), p.9, DTIC AD-A114189.
7. Z.L. Liao and J.N. Walpole, paper WB3, Technical Digest, Topical Meeting on Integrated and Guided-Wave Optics, Optical Society of America, 1982; Solid State Research Report, Lincoln Laboratory, M.I.T. (1981:3), p.7, DTIC AD-A112696.
8. J.J. Hsieh and C.C. Shen, Appl. Phys. Lett. 30, 429 (1977), DDC AD-A063419/6.
9. M. Hirao, A. Doi, S. Tsuji, M. Nakamura, and K. Aiki, J. Appl. Phys. 51, 4539 (1980).
10. Y. Itaya, T. Tanbun-Ek, K. Kishino, S. Arai, and Y. Suematsu, Jpn. J. Appl. Phys. 19, L141 (1980).
11. H. Nagai, Y. Noguchi, K. Takahei, Y. Toyoshima, and G. Iwane, ibid., p.L218.
12. T. Murotani, E. Oomura, H. Higuchi, H. Namizaki, and W. Susaki, Electron. Lett. 16, 566 (1980).
13. R.J. Nelson, R.B. Wilson, P.D. Wright, P.A. Barnes, and N.K. Dutta, IEEE J. Quantum Electron. QE-17, 202 (1981).
14. S. Arai, M. Asada, T. Tanbun-Ek, Y. Suematsu, Y. Itaya, and K. Kishino, ibid., p.640.
15. E. Oomura, T. Murotani, H. Higuchi, H. Namizaki, and W. Susaki, ibid., p.646.
16. P.C. Chen, K.L. Yu, S. Margalit, and A. Yariv, Appl. Phys. Lett. 38, 301 (1981).
17. W. Ng, C.S. Hong, H. Manasevit, and P.D. Dapkus, Appl. Phys. Lett. 39, 188 (1981).
18. W. Ng, C.S. Hong, H. Manasevit, and P.D. Dapkus, Third International Conference on Integrated Optics and Optical Fiber Communication, Optical Society of America, 1981, Technical Digest, p.52.
19. I. Mito, K. Kaede, M. Kitamura, K. Kobayashi, and S. Matsushita, ibid., p.44.
20. E. Oomura, H. Higuchi, R. Hirano, H. Namizaki, T. Murotani, W. Susaki, and K. Shirahata, ibid., p.44.
21. M. Nakamura and S. Tsuji, IEEE J. Quantum Electron. QE-17, 994 (1981).

II. QUANTUM ELECTRONICS

A. Co:MgF₂ LASER: HIGH-AVERAGE-POWER OPERATION, Q-SWITCHED PERFORMANCE, AND SCALING OPERATIONS

The pulse-pumped Co:MgF₂ laser described previously¹ was operated at a 50-Hz repetition rate to produce a TEM₀₀, average-power output of 7.3 W at 1.92 μm . The improvement in performance over earlier results¹ was obtained by coating the crystal heat sink with a thin layer of indium, which greatly improved the thermal contact between the crystal and heat sink. The input-output-power relation for the system is shown in Fig. II-1; the linearity indicates an absence of appreciable heating effects up to the 35 W maximum available output power from the Nd:YALO pump laser.

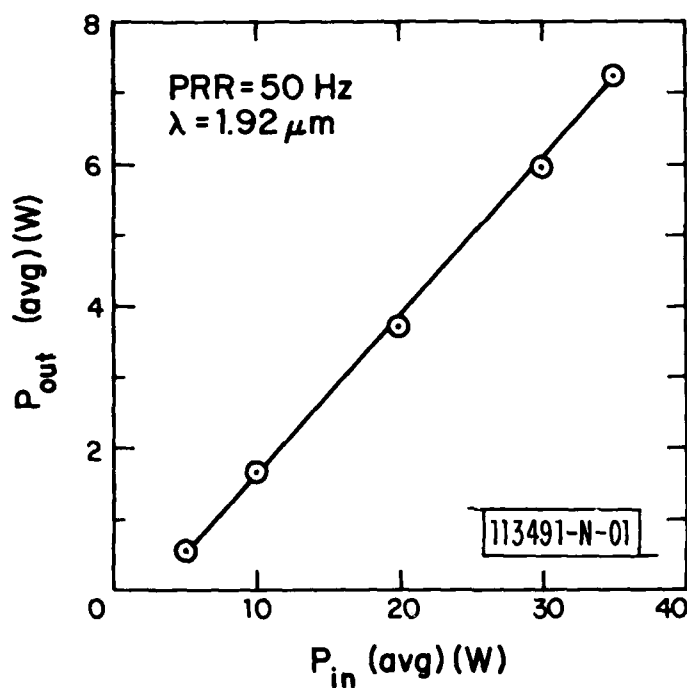


Fig. II-1. Co:MgF₂ laser average output power at 1.92 μm vs average input power, at a pulse rate of 50 Hz.

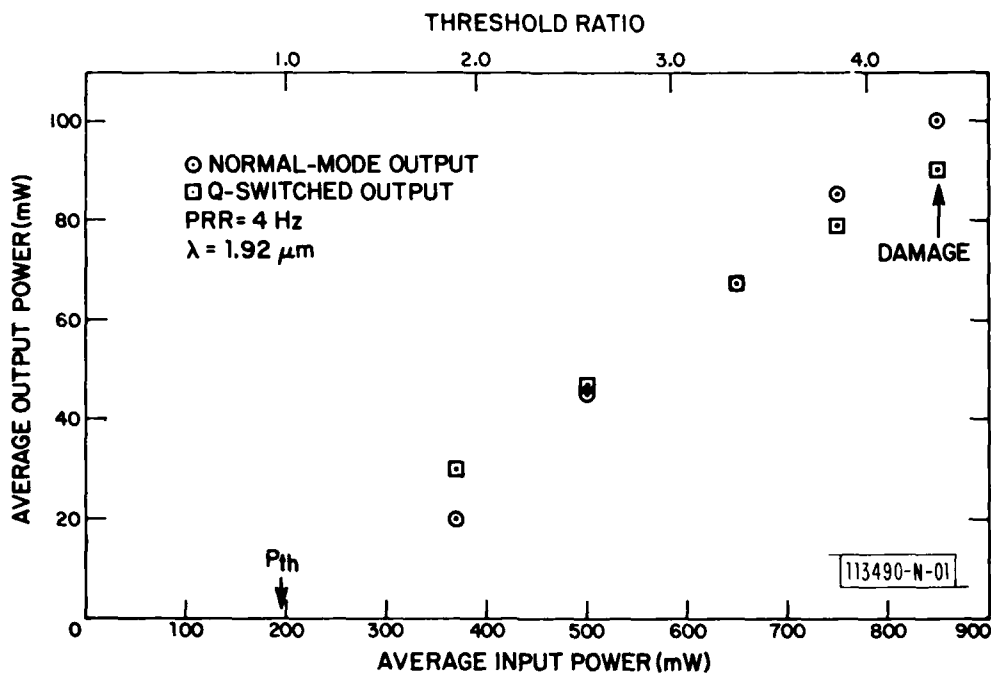


Fig. II-2. Average output vs input power for both normal-mode and Q-switched Co:MgF₂ laser, at a 4-Hz repetition rate.

Q-switching of the Co:MgF₂ laser was accomplished with the insertion of a fused silica, Brewster-angle acoustooptic loss modulator in the laser cavity. For these experiments, the output mirror transmission was ~5 percent and the pulse repetition rate was 4 Hz. The output-vs-input average-power relation at several operating points, for both normal and Q-switched modes of operation, is shown in Fig. II-2. At a pulsed-output energy of 25 mJ, damage to the cavity mirrors was observed; the output pulsewidth was approximately 200 ns. Reliable, TEM₀₀, damage-free operation was possible at a 20-mJ output-energy level, with the pulse shape indicated by Fig. II-3.

It is expected that higher output energies from the Co:MgF₂ laser can be generated by using cavity mirrors with high-damage-resistance coatings and by increasing the laser-cavity mode area. It is useful to calculate relationships needed for scaling up the output of the Co:MgF₂ system. For a

113493-R-01



Fig.II-3. Single-shot Q-switched output pulse of Co:MgF₂ laser. Pulse energy was 20 mJ.

Q-switched laser well above threshold, the output energy E_{out} is given by the relation

$$E_{out} = \eta(R - 1) N_{th} L_m A_m E_L$$

where N_{th} is the threshold population inversion density, R is the actual inversion divided by N_{th} , L_m is the length of the gain medium, A_m is the effective cavity beam-area in the medium, and E_L is the energy of the laser photon; η is the coupling efficiency of the system, defined as the ratio of output coupling loss to total cavity loss. The peak output power P_{out} for a Q-switched laser has to be determined by numerical techniques, but a bounding relation is that

$$P_{out} < E_{out} / 2\tau_c$$

where τ_c is the cavity lifetime.

The very low scattering and diffraction losses in Co:MgF₂ and in the fused-silica Q-switch allow certain simplifying assumptions to be made, because the loss in the cavity (for output-mirror transmissions greater than ~0.5 percent) is essentially determined by the output mirror transmission. Then the value for τ_c is given by

$$\tau_c = 2L/cT$$

where L is the length of the optical cavity, c is the speed of light, and T is the fractional transmission of the output mirror. Also, the value for N_{th} is proportional to T. An additional relationship is that N_{th} is inversely proportional to σ , the laser gain cross section.

With these assumptions, the following relationships hold:

$$E_{out} \propto T(R - 1) A_m / \sigma$$

and

$$P_{out} \propto T^2(R - 1) A_m / \sigma L$$

In considering optical damage to the cavity components, two quantities are of interest - the intracavity fluence F_c (in joules/cm²) and the intracavity intensity I_c (in watts/cm²). These are related by

$$F_c \propto (R - 1) / \sigma$$

and

$$I_c \propto T(R - 1) / \sigma L$$

It has been found that optical damage thresholds for dielectric surfaces depend both on F_c and the pulsewidth, such that the damage value for F_c

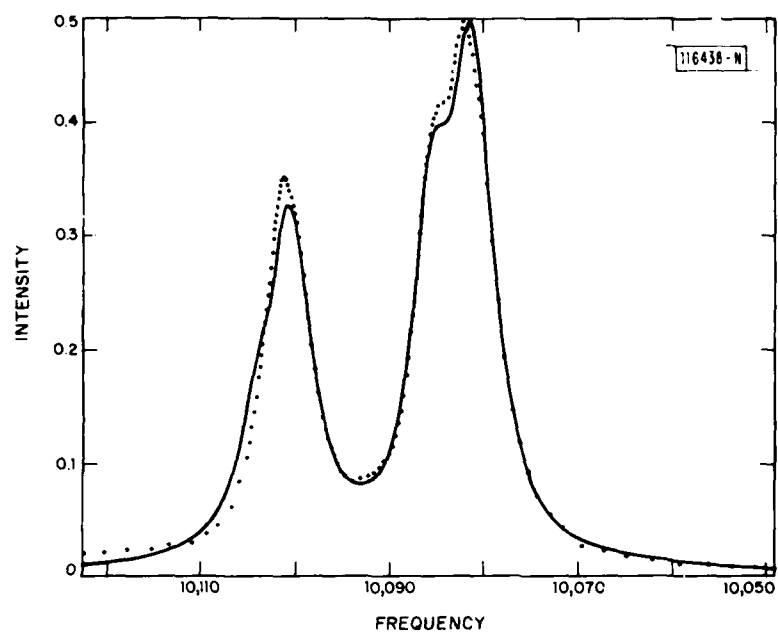
typically increases as the square root of the pulsewidth²; thus, neither F_c nor I_c alone can be used to determine the damage-free operating conditions for a system. However, for small cross sections it could be possible to operate the laser only slightly above threshold because of damage limitations. From the experimental results for the Co:MgF₂ laser it is evident from Fig. II-2 that, with output pulsewidths on the order of 200 ns, operation at values of R at least up to 4 can be achieved without damage. This means that, at that pulsewidth, efficient and stable operation of the Co:MgF₂ laser in the Q-switched mode is possible. The beam diameter in these experiments was about 0.8 mm; with the same output coupling and cavity length, it should be possible to obtain 100 mJ of Q-switched output at a beam diameter of 1.8 mm. Experiments to increase the beam diameter by modifying the cavity optics are now in progress.

P.F. Moulton

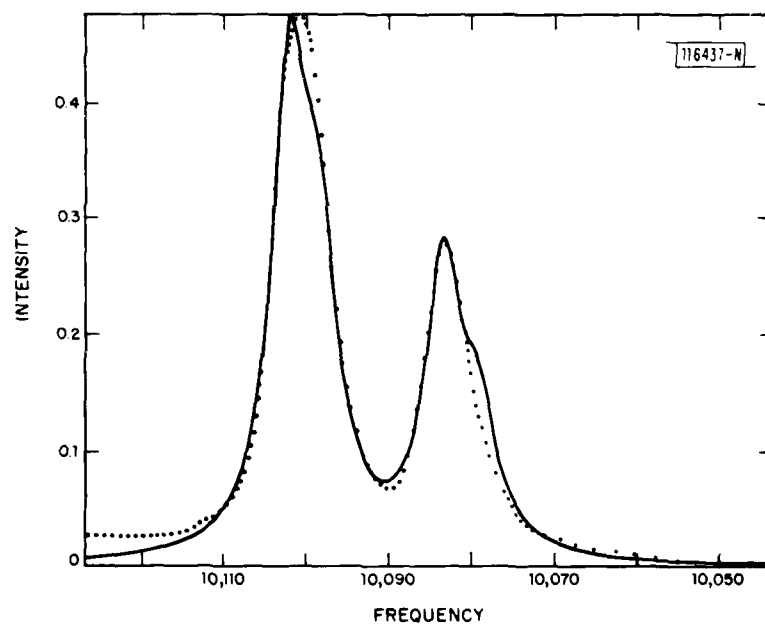
B. JAHN-TELLER EFFECT AND THE OPTICAL ABSORPTION SPECTRUM OF V²⁺ IN MgF₂

Calculations of the optical gain cross section for the vibronic, ⁴T₂ + ⁴A₂ laser transition of V²⁺ in MgF₂ from basic spectroscopic data require knowledge of the energy-level structure of the ⁴T₂ state. Such information is needed to relate measurements of the cross section for zero-phonon ⁴A₂ + ⁴T₂ absorption to the corresponding vibronic emission cross section. Sturge *et al.*³ have previously pointed out the probable existence of a strong Jahn-Teller interaction between the host lattice and the ⁴T₂ state. We report here calculations on the ⁴T₂ levels which take this interaction into account and explain, in particular, the measured zero-phonon-line absorption spectrum.

The observed spectrum [see Figs. II-4(a) and (b)] consists of a doublet in both σ and π geometry, with partially resolved fine structure within each line of the doublet. V²⁺ ions occupy Mg substitutional sites in the MgF₂ rutile lattice. There are two types of V²⁺ sites, each of D_{2h} point



(b)



(a)

Fig. II-4. Computer fit (solid curve) to experimental zero-phonon absorption spectrum (dotted curve) for V^{2+} in MgF_2 : (a) σ polarization; (b) π polarization.

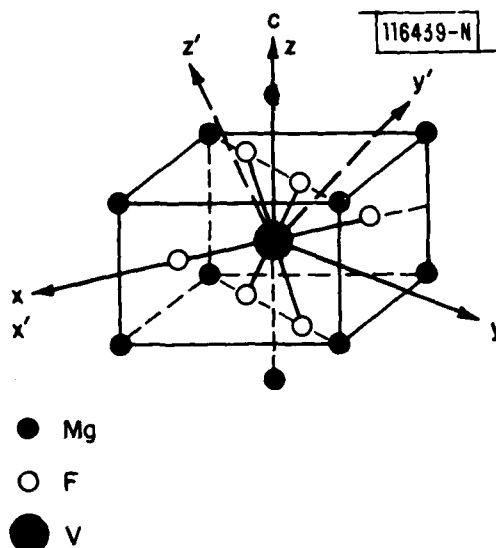


Fig. II-5. Schematic diagram showing environment of V^{2+} ion in MgF_2 in one type of orthorhombic site. Second type of site is same, except for 90° rotation about c-axis.

symmetry, which are equivalent with respect to a 90° rotation about the crystal c-axis (see Fig. II-5). The near-neighbor V^{2+} environment is only slightly distorted from octahedral symmetry, so that we assume that the octahedral eigenstates are useful as a starting basis set. The three T_2 excited electronic states transform as $X' \equiv y'z'$, $Y' \equiv z'x'$, and $Z' \equiv x'y'$, where the primes refer to octahedral axes as shown in Fig. II-5. In the presence of coupling to a vibronic mode of E symmetry, a Jahn-Teller distortion takes place, and new basis functions for the description of the problem become

$$\psi_i = X'_i(r) \phi_i(Q) \quad (II-1)$$

where $X'_i(r)$ are electronic functions transforming as X' , Y' , Z' , and the $\phi_i(Q)$ are corresponding ground-state vibrational functions centered about

three equivalent points in Q-space. The Jahn-Teller distortion in first approximation leaves the three basis states degenerate. There is a nonzero overlap integral (γ) between the wave functions $\phi_i(Q)$ for different values of i .

The effective Hamiltonian describing the 4T_2 state of V^{2+} in MgF_2 projected onto the basis set Eq. (II-1) is

$$\begin{aligned} \mathcal{H} = & -\lambda \vec{L} \cdot \vec{S} + \kappa (\vec{L} \cdot \vec{S})^2 + \rho (L_x^2 S_x^2 + L_y^2 S_y^2 + L_z^2 S_z^2) \\ & - A L_x^2 - B L_z^2 \end{aligned} \quad (II-2)$$

In Eq. (II-2), \vec{L} is a pseudo angular momentum vector operator for $L = 1$. The first term on the right represents the spin-orbit interaction, and the second and third terms represent second-order effects of the spin-orbit interaction (neglecting non-cubic corrections). The fourth and fifth terms represent crystal-field corrections due to the elongation of the Mg-F distance along x' , and the "scissoring" of the Mg-F axes away from y' and z' (the unprimed z -axis is shown in Fig. II-5).

Using the Hamiltonian Eq. (II-2) and the basis states Eq. (II-1), we have calculated eigenvectors and eigenvalues representing the 4T_2 state of V^{2+} in MgF_2 . These have been used to calculate the relative intensities in both σ and π geometry for the zero-phonon absorption spectrum. The best fit to the spectrum obtained thus far assumes that the Z' vibronic state is raised in energy at least 100 cm^{-1} by the orthorhombic potential A (see Fig. II-6). The main splitting of the observed spectrum is given by the second-order spin-orbit interaction $2(\kappa + \rho)$. The additional structure within the main components is due to the spin-orbit interaction and orthorhombic crystal potential B, both drastically reduced by the Jahn-Teller overlap factor γ , since they occur in the Hamiltonian matrix only as off-diagonal elements between the vibronic basis states. In this preliminary fit, we have neglected the off-diagonal contributions of $\kappa(\vec{L} \cdot \vec{S})^2$, which should also be reduced by the factor γ . The fit obtained in Fig. II-4 was

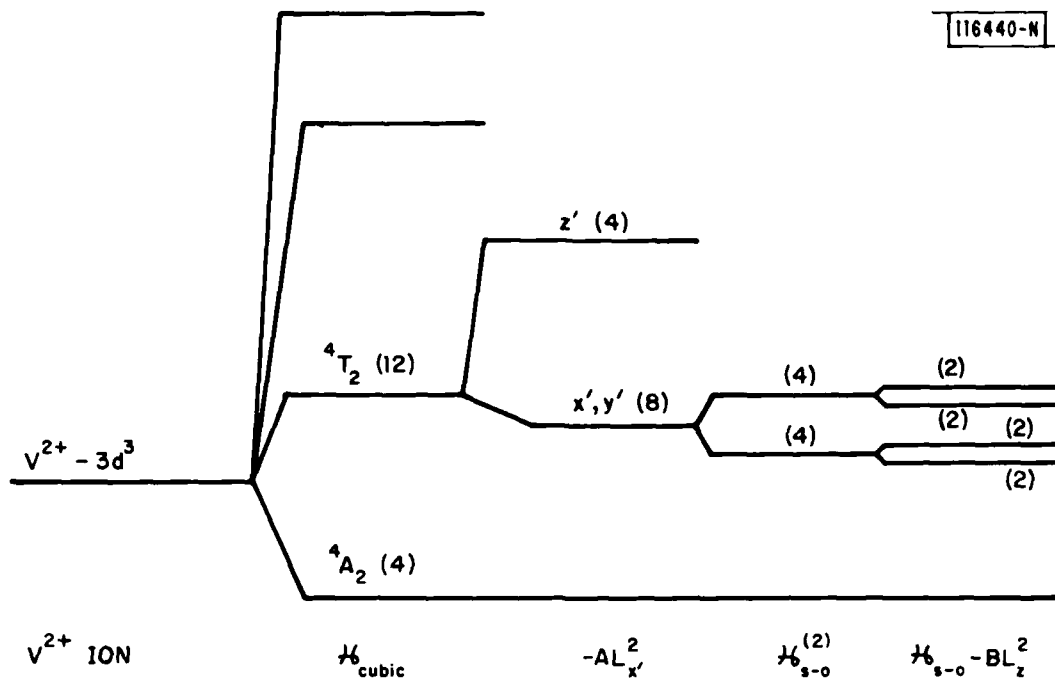


Fig. II-6. Schematic showing breakup of V^{2+} -ion levels in presence of Hamiltonian Eq. (II-2). \mathcal{H}_{s-o} and $\mathcal{H}_{s-o}^{(2)}$ are spin-orbit interaction and second-order spin-orbit interaction, respectively. Effect of \mathcal{H}_{s-o} and $-\mathcal{B}L_z^2$ are reduced by Jahn-Teller overlap factor γ .

based on the parameters $(\kappa + \rho) = -9 \text{ cm}^{-1}$, $\gamma\lambda = 1.2 \text{ cm}^{-1}$, $\gamma B = 3.4 \text{ cm}^{-1}$, $A > 100 \text{ cm}^{-1}$. All components of the spectrum were assumed to be Lorentzian with half-width 2.6 cm^{-1} . We will seek to improve the details of the fit by introducing the additional off-diagonal parameter $\gamma\kappa$ into the calculation.

H.J. Zeiger
P.F. Moulton

C. RAMAN SPECTRA OF ULTRATHIN Si FILMS

Raman scattering in crystalline materials such as semiconductors involves the interaction of an incident photon of energy $\hbar\omega_i$ with a phonon of energy $\hbar\omega_q$ to produce a scattered photon of energy $\hbar\omega_s = \hbar\omega_i - \hbar\omega_q$ (Stokes scattering). In crystals of macroscopic size, the requirement of momentum

conservation allows only long-wavelength optical phonons with wavevectors near the Brillouin-zone center to participate in the scattering process. In crystals of dimensions approaching typical lattice dimensions, however, this momentum conservation requirement is relaxed, and phonons with nonzero wavevectors contribute to the Raman spectrum, resulting in the broadening and shifting of the optical phonon line. Raman spectroscopy therefore provides an indication of the size of crystalline samples, and has been employed to characterize polycrystalline semiconductor films that have been incompletely recrystallized from the amorphous state.^{4,5} However, no quantitative explanation of the dependence of the observed Raman spectra on crystallite size has been presented. We report here the preliminary results of our study of sample size effects on the Raman spectrum of the optical phonons in Si (at 520 cm^{-1} in bulk Si) using Si films that have long-range crystalline order in two dimensions but are very thin in the third dimension (down to 30 \AA). This system is easily characterized with well-known optical constants and is more accessible to simple modeling than are films consisting of crystallites of random size and orientation. A quantitative understanding of the effect of sample size on Raman lineshape will enhance the utility of Raman spectroscopy as a diagnostic technique for characterizing polycrystalline material. These measurements are also important for understanding the modifications that must be made in conventional physical models of semiconductor devices in order to scale to ultrasmall dimensions.

Thin Si films were prepared from commercially obtained $\langle 100 \rangle$ Si epitaxially grown on 2-in.-dia. polished sapphire substrates. The Si was uniformly oxidized until a thin Si layer of the desired thickness remained under a thick SiO_2 cap. The individual layer thicknesses of the resulting Al_2O_3 -Si- SiO_2 structure were determined by fitting to theory experimental transmission spectra recorded over the 0.4- to $3\text{-}\mu\text{m}$ wavelength range. Good agreement between calculated and experimental transmission spectra was obtained down to Si thicknesses on the order of 50 \AA using the optical constants of bulk Si. Because of the nonuniform thickness of the starting silicon-on-sapphire (SOS) material, the thickness of the Si layer used for

the measurements varied from 0 to $>650 \text{ \AA}$, with a linear wedge of 35 \AA/mm across the wafer. It was therefore possible to investigate a wide range of Si-film thicknesses using a single wafer.

Raman spectra of the 520-cm^{-1} optical phonon were recorded in a back-scattering geometry with the 4880-\AA radiation of an Ar-ion laser normally incident on the film. A 60X microscope objective was used as both the focusing and collection lens to provide $1\text{-}\mu\text{m}$ spatial resolution. The scattered light was dispersed by a 1-m double spectrometer and detected with a cooled GaAs PMT using photon counting electronics. Raman spectra measured as a function of Si-film thickness over a thickness range of 190 to 30 \AA exhibit the following general behavior: (1) as the Si thickness decreases, the Raman line broadens and develops a low-frequency tail extending as far as 70 cm^{-1} from line center; (2) the peak position of the Raman line does not shift significantly ($<1 \text{ cm}^{-1}$) from its value for $0.5\text{-}\mu\text{m}$ SOS even for a Si thickness as small as 28 \AA . This second observation is in contrast to results obtained with polycrystalline Si for which large shifts in Raman peak position have been reported and attributed to dimensional effects in the small crystallites.⁴ Spectra recorded for the thicknesses of 28 and 190 \AA are shown in Fig. II-7. The spectrum of the 28-\AA -thick film clearly exhibits an unshifted, broad, central peak and a low-frequency tail. The Raman linewidth of the 190-\AA film is broadened because of laser heating; its low power value of 5.9 cm^{-1} is the same as that obtained for $0.5\text{-}\mu\text{m}$ SOS. Dramatic broadening of the Raman line does not occur for film thicknesses greater than approximately 100 \AA , as can be seen from the summary of linewidth measurements in Fig. II-8, which displays the central peak linewidth as a function of the film thickness.

Broadening of the Raman line toward lower frequency is expected to accompany the relaxation of phonon wavevector selection rules in crystals of finite size because of the participation in the scattering process of lower-energy phonons with wavevectors extending into the Brillouin zone. In amorphous Si, where there is no long-range order and all phonons are able to participate in the scattering process, the Raman line is extremely broad and

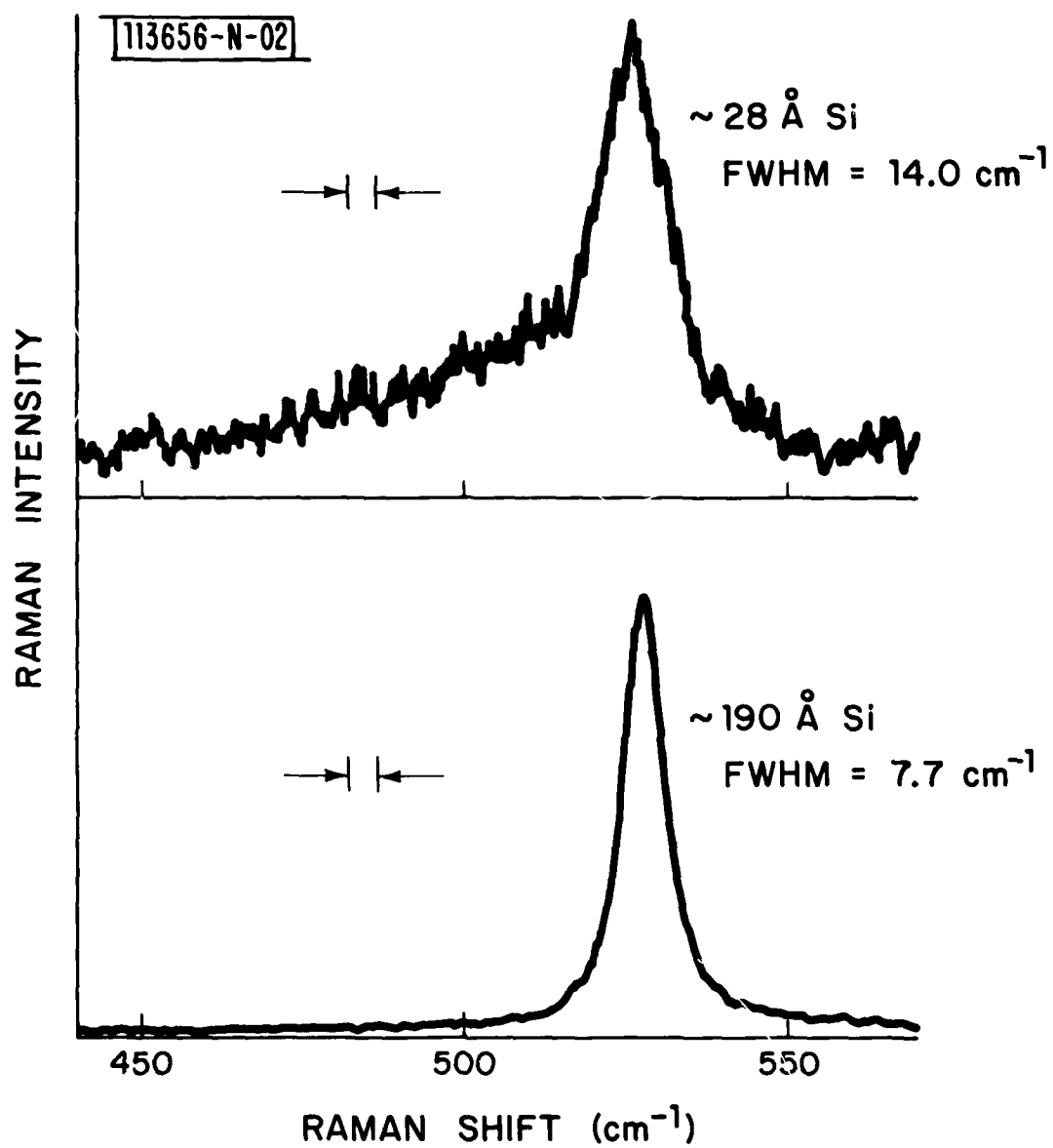


Fig. II-7. Optical phonon Raman spectra in Si films of 28- and 190-Å thickness.

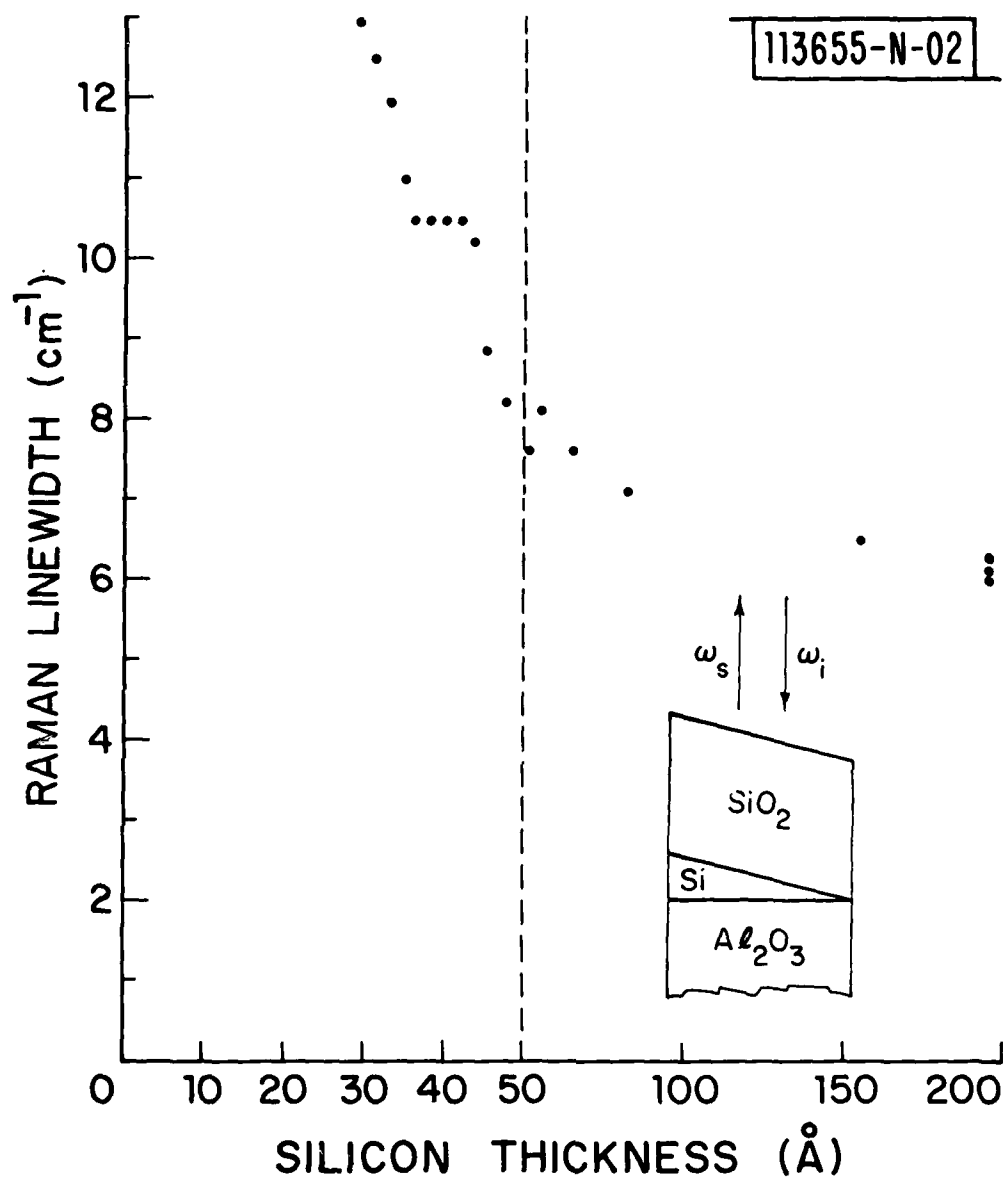


Fig. II-8. Raman linewidth measured as a function of Si film thickness. Experimental scattering geometry and multilayer sample structure are also shown.

centered at 480 cm^{-1} . It is interesting to note that the 30-Å film is only six lattice constants thick but nevertheless has a spectrum that is much closer to that of bulk Si than to that of amorphous Si. Theoretical efforts are currently under way to model the dependence of the Raman lineshape on film thickness in order to understand the transition from a crystalline to amorphous spectrum. Part of the observed broadening may be due to increased phonon scattering at the film boundaries. In addition, the spectra of thin films may be strongly influenced by the defects at the Si-Al₂O₃ interface. Even for the 30-Å film, however, the bulk Si polarization selection rules which depend upon the crystal structure were still well satisfied experimentally. It is uncertain, therefore, what effect the interface defects have on the observed spectra. Films of Si on quartz which have fewer interface defects are being prepared for further study.

D.V. Murphy
S.R.J. Brueck
D.D. Rathman

D. EFFICIENT GaAs SOLAR CELLS FORMED BY UV LASER CHEMICAL DOPING

The use of UV laser chemical processing to dope silicon has recently been described.⁶⁻⁸ The process has been used to make good-quality p-n junctions which have been fabricated into Si solar cells with AM1 efficiencies of 10.3 percent.² We have now applied this technique to the doping of GaAs and to the formation of GaAs solar cells.

In its simplest form, laser chemical doping involves the photolysis of gas phase molecules with a pulsed UV laser to release dopant atoms which strike the surface of the semiconductor. The pulsed laser simultaneously heats the surface of the semiconductor to the melting point, allowing liquid state diffusion of the dopant atoms into the semiconductor. We have examined S-doping of GaAs using H₂S, a common doping gas used in systems for growing GaAs by chemical vapor deposition (CVD). A pulsed ArF excimer laser, operating at 193 nm and producing 7-ns-long pulses, was used as a

source. The laser beam was brought to a line focus near the surface of the sample by a 5-cm-focal-length quartz cylindrical lens. The laser was operated at 2 Hz, with typical laser energy densities at the sample surface of 0.1 J/cm^2 . The GaAs samples were enclosed in a 1-cm-long stainless-steel cell which was translated normal to the beam axis. Scan rates of 0.25 to 8 mm/min. were examined; a rate of 1 mm/min., corresponding to ~ 32 pulses per focal area, was near-optimum for solar-cell formation and was used in the experiments described below.

GaAs solar cells were formed by S-doping a p epilayer grown on a p^+ substrate, producing a $n^+/p/p^+$ shallow homojunction structure. The epilayer and substrate were doped with Zn to concentrations of about 1×10^{17} and $5 \times 10^{18} \text{ cm}^{-3}$, respectively. Samples for van der Pauw measurements of sheet resistance and mobility were made by using substrates having an n^- epilayer with a carrier concentration of $\sim 10^{14} \text{ cm}^{-3}$.

A number of parameter studies were performed to find the optimum conditions for the formation of solar cells. Sections of a GaAs strip were processed under different conditions and then masked and wet-etched to produce mesa solar-cell structures having an area of about 1 mm^2 . A relative measure of solar-cell performance was obtained from the open-circuit voltage V_{oc} under a fixed illumination by a microscope light. Figure II-9(a) shows the variation of the electrical properties of laser-doped GaAs with ArF laser energy density, while Fig. II-9(b) shows the dependence of the V_{oc} of small test cells on laser energy density at the sample surface. The latter curve shows that there is only a relatively narrow range of energy densities over which optimum solar-cell performance can be obtained; this range is about ± 10 percent from the optimum. This contrasts with our previous experiments using laser-doping to make Si solar cells; in that case, the incident energy density could be varied by about ± 25 percent around a nominally optimum value without significant variation in V_{oc} .

Figure II-9(a) gives some indication of the reason for the more critical nature of GaAs junction formation. The electrical properties of the doped material, namely the sheet resistance and the surface carrier density,

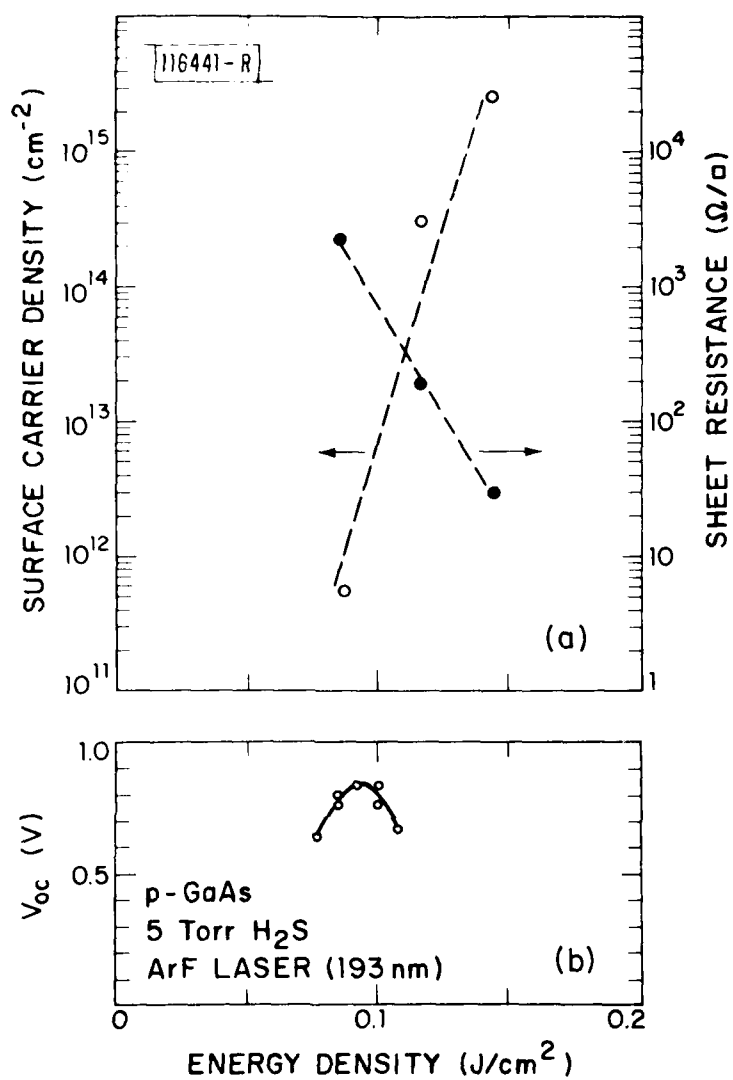


Fig. II-9. (a) Surface carrier density and sheet resistance of UV laser doped GaAs as a function of 193-nm energy density at substrate. $\text{P}_{\text{H}_2\text{S}} = 5$ Torr. (b) Open-circuit voltage of GaAs solar cells under fixed, arbitrary, illumination vs 193-nm energy density.

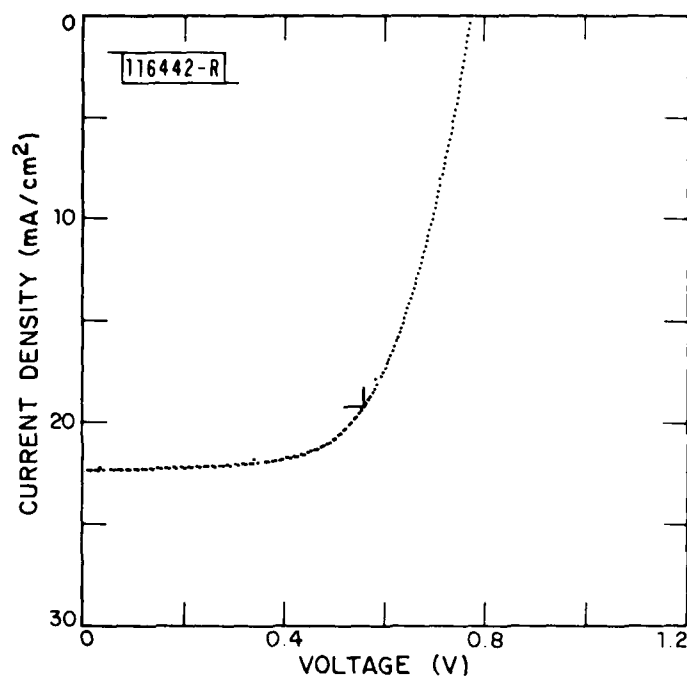


Fig. II-10. Photocurrent density as a function of voltage for a 3 x 3-mm photochemically doped, antireflection-coated, GaAs solar cell with an efficiency of 10.8 percent at AML.

change by decades for variations of less than 50 percent in the laser beam energy density; although only three samples were examined, the trend is clear. The surface mobility, as obtained from the van der Pauw measurements, decreased from 4500 to 80 $\text{cm}^2/\text{V-s}$ as the energy density was increased over the same range covered by Fig. II-9(a). Thus, increasing the doping concentration is accompanied by a more rapid decrease in electron mobility than that which would be expected on the basis of the known variation of mobility with carrier concentration, and may well reflect the effect of laser-induced, electrically active, defects. The narrow range for maximum V_{oc} probably results from the strong dependence of both doping density and mobility on laser energy density.

Figure II-10 shows the current-voltage curve of a 3 x 3-mm-square cell fabricated from an ArF laser irradiated sample; the cell was the best of

several units. The cell has been antireflection coated with an 800-Å-thick, electron-beam-evaporated, Ta_2O_5 film having a refractive index of 2.0. The V_{oc} was 0.775 V, the short-circuit current density J_{sc} was 22.3 mA/cm² (not corrected for contact finger area), and the fill factor was 0.62, resulting in a measured AM1 efficiency of 10.8 percent. This efficiency compares quite favorably with the value of 12 percent obtained for ion-implanted, CW Nd:YAG laser-annealed, GaAs solar cells of somewhat smaller area.⁹

In conclusion, we have used pulsed UV laser radiation to dope GaAs by a process involving dissociation of a doping gas and laser-initiated liquid state diffusion. The doping process has been used to produce p-n junctions which function as solar cells having an AM1 efficiency of 10.8 percent, a value comparable to that achieved in cells formed using laser annealing techniques. The formation of p-n junctions which function as efficient solar cells requires close control over laser parameters. The low sheet resistances obtained compare favorably to those produced using other beam-processing techniques and suggest that ohmic contact formation is a possible application for the technique.

T.F. Deutsch	G.W. Turner
J.C.C. Fan	R.L. Chapman
D.J. Ehrlich	R.P. Gale

E. FABRICATION OF THROUGH-WAFER VIA CONDUCTORS IN Si BY LASER PHOTOCHEMICAL PROCESSING

Through-wafer via conductors have applications in the bonding and interconnecting of novel integrated-circuit device structures. Previous methods of fabrication have relied on the anisotropic wet etching of single-crystal substrates; a large opening angle, associated with the intersection of slow-etching crystallographic planes of the substrate, limits these methods to low effective-aspect-ratio via holes. To illustrate this limitation, a typical closest spacing for vias wet etched in a 10-mil wafer is ~15 mils.

We have recently developed a procedure for the fabrication of high-aspect-ratio through-wafer via conductors in Si. The technique is based on a

rapid, highly anisotropic, laser etching process followed by a two-step metallization.

The details of the laser etching process have been described previously. Briefly, the unprocessed Si wafer is enclosed in a Cl_2 atmosphere and irradiated with several watts of focused multiline output from an argon-ion laser. As illustrated in Fig. II-11(a), the laser output both photolyzes the Cl_2 into reactive Cl atoms and at the same time heats a several-micrometer spot on the wafer to near the Si melting point. A highly localized reaction results in rapid etching accompanied by the evolution of volatile SiCl_4 . Feature sizes as small as several micrometers have been produced. Although a

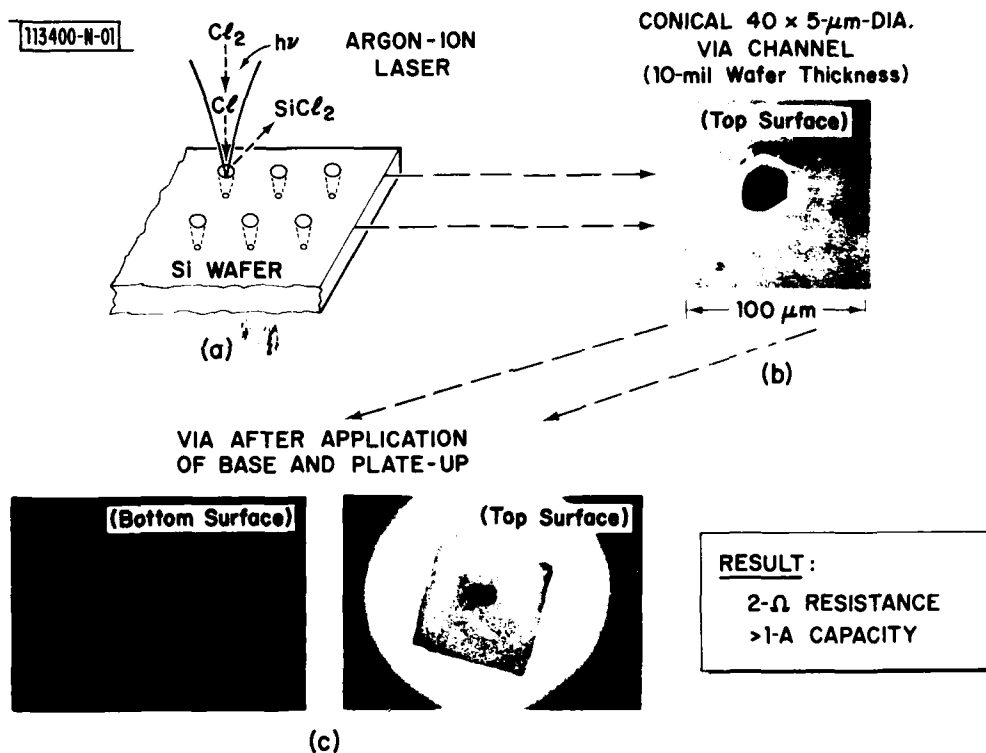


Fig. II-11. Procedure for fabricating through-wafer via conductors. (a) Laser chemical etching of high-aspect-ratio conical holes in Cl_2 gas. (b) Top surface scanning-electron micrograph of a conical via. (c) Top and bottom surface micrographs of finished via conductor. Top surface view shows a rectangular pad for reverse-surface bonding.

selective etching of (100) surfaces is seen at low laser powers, no orientational preference is observed at the higher powers used in this study. Etch-rate differences for n- and p-type wafers and different doping levels are also small.

For this demonstration, arrays of via holes were etched through unprocessed Si wafers. The wafers were loaded into a reaction chamber containing 400 Torr of research-grade Cl_2 . A 3-W argon laser beam was focused with an f/10 achromatic doublet to an $\sim 6\text{-}\mu\text{m}$ spot on the front surface of the wafer. This exposure initiates a rapid reaction which results in through-wafer etching of 250- μm -thick wafers in ~ 25 s; an increased rate can be obtained at higher Cl_2 pressures. With the laser focus at the wafer front surface, conical (40- μm dia. decreasing to 5- μm dia.) holes are produced.

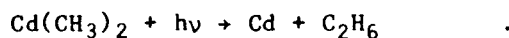
Figure II-11(b) shows a top-surface scanning-electron micrograph for a wafer with a (100) surface orientation. Note that both surfaces show indications of the rectangular etching profile characteristic of the (100) orientation. This indicates that, in the wings of the thermal gradient, etching is controlled by slow dissolution of (111) planes. However, the high aspect ratio of the through-wafer channels shows that in the center of the laser spot the etching profile is primarily determined by the radial thermal distribution. As a result, the hole taper can be controlled by adjusting the peak temperature and beam geometry; conical, doubly tapered, and nearly straight-walled profiles were obtained by altering the focusing conditions and laser power.

After the via holes were etched, the wafers were thermally oxidized to an SiO_2 thickness of 1 μm in order to isolate the via conductor from the Si wafer. Two methods were then used to apply a plating base to the internal hole surface.

In the first method, Ag was evaporated onto both sides of the wafer. Although straightforward, this approach has the disadvantage that heavy evaporation is required since the internal hole surface is at an oblique angle relative to the source. A top-surface thickness on the order of 10 to 15 μm was required to produce a conductive base for the channels used in this

study. An attempt to significantly reduce the material consumed in this step using sputtering was not successful, despite the generally greater step coverage of sputter deposition.

In the second method, laser photodeposition was used to apply the plating base. This approach has the advantage that holes of arbitrarily high aspect ratio can be metallized. To use this process, the wafers were placed under a 1- to 2-Torr atmosphere of $\text{Cd}(\text{CH}_3)_2$. A 10- μW , 257.2-nm beam from a frequency-doubled argon-ion laser was then focused into the etched via holes. The light beam deposits a Cd surface film by the reaction



Grazing-incidence UV radiation is sufficient to obtain efficient deposition and gives good coverage even on nearly vertical surfaces. For this study 1-min. UV exposures were used, although shorter processing times are possible with a high-power laser.

After a conducting base was applied, the via metallization was completed by gold electroplating. Photolithography was then used to isolate the vias for testing. Figure II-11(c) shows top and bottom surface views of a completed via. The via conductors had resistances in the range 0.5 to 5 Ω , and could carry currents of up to 1 A before failing. None of them were shorted to the Si wafer itself. Results using evaporation and laser photodeposition of the plating base were nearly equally good, although conductors formed by photodeposition operate less stably until a several-mA burn-in is performed.

D.J. Ehrlich	R.W. Mountain
D.J. Silversmith	J.Y. Tsao

F. THREE-TERMINAL DEVICE USED FOR OPTICAL HETERODYNING AT SUBMILLIMETER IFs

There has been considerable interest in extending heterodyne technology into the visible region of the spectrum. Such work has relied on MOM devices

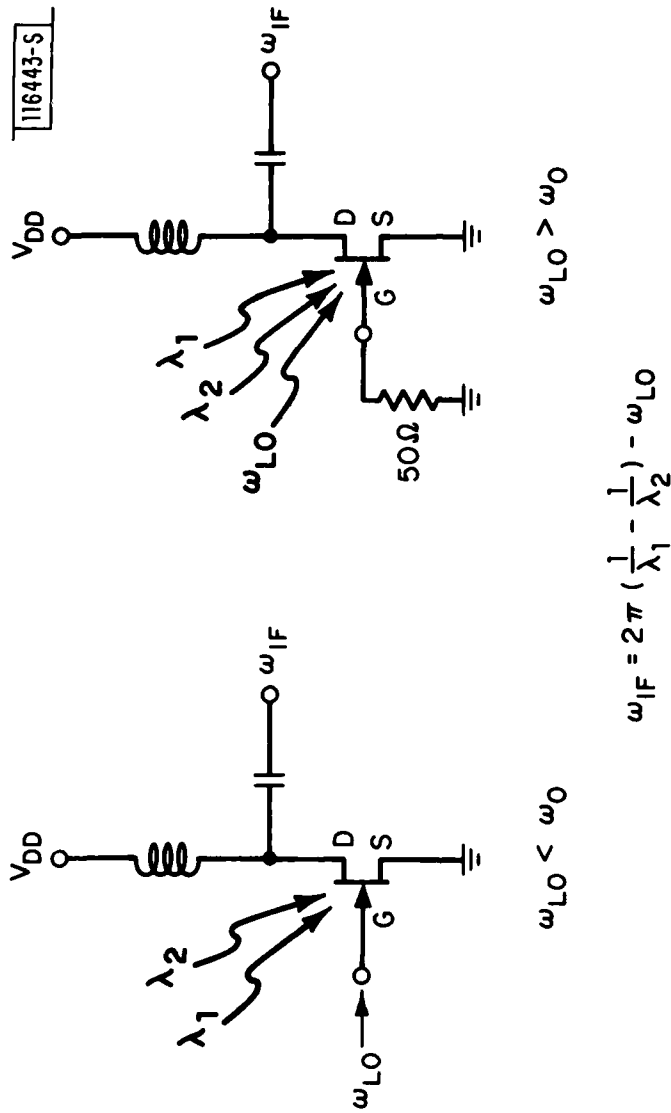


Fig. II-12. Schematic representation of optical mixing plus two ways of downconverting in three-terminal devices.

and, more recently, on Schottky diodes.¹⁰ However, it has been difficult to find suitable devices that both respond to visible radiation and also exhibit wide IF bandwidths. We report here the use of three-terminal GaAs FETs to mix two visible lasers with IF response up to 300 GHz. Above 10 GHz a local oscillator (LO) is injected directly into, or near, the gate region of the FET, and the IF is downconverted to about 500 MHz. Since response to optical signals has been previously observed in FETs,¹¹⁻¹⁴ our initial experiments were to verify that millimeter and submillimeter radiation could be effectively coupled and detected in the device. Video response has been obtained up to 800 GHz, and carcinotron radiation at 350 GHz was mixed with the 5th harmonic of a 70-GHz klystron to produce a 45-dB signal-to-noise IF.

In going to the optical region, a He-Ne laser at 6328 Å and a tunable, stabilized dye laser pumped by an Ar⁺ laser were focused onto the vicinity of the gate with an ~3-μm diffraction-limited spot. The FET gate is 0.5 μm long by 52 μm wide, and the FET is mounted in the common source configuration and biased in the linear region rather than in the saturated region.¹¹⁻¹⁴ The IF signal is taken from the drain terminal. Below 40 GHz, the IF was downconverted to 500 MHz by directly injecting an LO into the gate. At the higher IF frequencies the klystron or carcinotron was coupled in via a closely placed waveguide (see Fig. 11-12).

A number of mechanisms for the observed mixing are possible, such as photoconductivity and consequent modulation of the depletion width for the optical mixing, and distributed capacity effects under the Schottky gate for the millimeter-wave response. Further, since the FET can function as a three-terminal oscillator while simultaneously detecting submillimeter radiation or optical beats, it offers interesting device possibilities such as self-oscillating mixers or subharmonic LOs. These experiments suggest application to measuring and locking optical wavelength sources to far-IR and RF frequency standards, as well as to very wide-bandwidth optical communications.

H.R. Fetterman A. Chu
D.D. Peck P.E. Tannenwald

REFERENCES

1. Solid State Research Report, Lincoln Laboratory, M.I.T. (1981:3), pp.15-21, DTIC AD-A112696.
2. D. Milam, in Laser Induced Damage in Optical Materials, A.J. Glass and A.H. Guenther, Eds. (U.S. GPO, Washington, 1978), NBS Special Publ. 541, pp.164-167.
3. M.D. Sturge, F.R. Merritt, L.F. Johnson, H.J. Guggenheim, and J.P. van der Ziel, J. Chem. Phys. 54, 405 (1971).
4. J.F. Morhange, G. Kanellis, and M. Balkanski, Solid State Commun. 31, 805 (1979).
5. R.P. Salathe, H.P. Weber, and G. Badertscher, Phys. Lett. 80A, 65 (1980).
6. T.F. Deutsch, J.C.C. Fan, G.W. Turner, R.L. Chapman, D.J. Ehrlich, and R.M. Osgood, Jr., Appl. Phys. Lett. 38, 144 (1981), DTIC AD-A101030/5.
7. J.C.C. Fan, T.F. Deutsch, G.W. Turner, D.J. Ehrlich, R.L. Chapman, and R.M. Osgood, Jr., Proc. 15th IEEE Photovoltaic Specialists Conference - 1981, Orlando, Florida, 12-15 May 1981, p.432, DTIC AD-A109263.
8. T.F. Deutsch, D.J. Ehrlich, D.D. Rathman, D.J. Silversmith, and R.M. Osgood, Jr., Appl. Phys. Lett. 39, 825 (1981), DTIC AD-A110715.
9. J.C.C. Fan, R.L. Chapman, J.P. Donnelly, G.W. Turner, and C.O. Bozler, Appl. Phys. Lett. 34, 780 (1979), DDC AD-A073884/9.
10. B. Burghardt et al., Appl. Phys. Lett. 35, 498 (1979).
11. J.J. Pan, SPIE, Vol. 150, 175 (1978).
12. J.C. Gammel and J.M. Ballantine, IEEE Intl. Electron Devices Mtg., Washington, DC, 4-6 December 1978.
13. W.D. Edwards, IEEE Electron Device Lett. EDL-1, 149 (1980).
14. P.R. Smith et al., Appl. Phys. Lett. 39, 739 (1981).

III. MATERIALS RESEARCH

A. PROPERTIES OF ZONE-MELTING-RECRYSTALLIZED Si FILMS ON SiO₂-COATED SUBSTRATES

Silicon-on-insulator (SOI) structures consisting of thin Si films on insulating layers over Si substrates are of interest as potential materials for very-high-density and very-high-speed integrated circuits (ICs). We recently reported¹ a recrystallization process that uses a movable graphite strip heater for zone melting polycrystalline Si films deposited on SiO₂-coated Si substrates. The recrystallized films, which have (100) texture, consist of elongated grains with dimensions up to a few millimeters by a few centimeters. The grains contain numerous sub-grain boundaries that are typically spaced about 20 μm apart. Both grain and sub-grain boundaries are generally aligned parallel to the direction of molten-zone motion.²

We have been investigating the semiconductor properties of the zone-melting-recrystallized films in order to assess their potential usefulness for IC applications. The results of initial studies³ were promising, since large-dimension MOSFETs fabricated in the films were found to have good electrical characteristics despite the presence of sub-boundaries in their active region. We have now extended these studies in order to investigate the electrical properties of the sub-boundaries in detail. We find that the sub-boundaries have little effect on majority electron transport at room temperature and above for films with carrier concentrations of about 10^{17} cm^{-3} . Therefore, SOI structures incorporating zone-melting-recrystallized films show promise for IC applications, even though the films contain sub-boundaries. In addition, we have measured the minority-carrier generation lifetimes both in zone-melting-recrystallized Si films and in epitaxial Si layers grown by chemical vapor deposition (CVD) on such films. The lifetimes in both materials are in the microsecond range, indicating their potential usefulness for bipolar devices.

113054-R-01

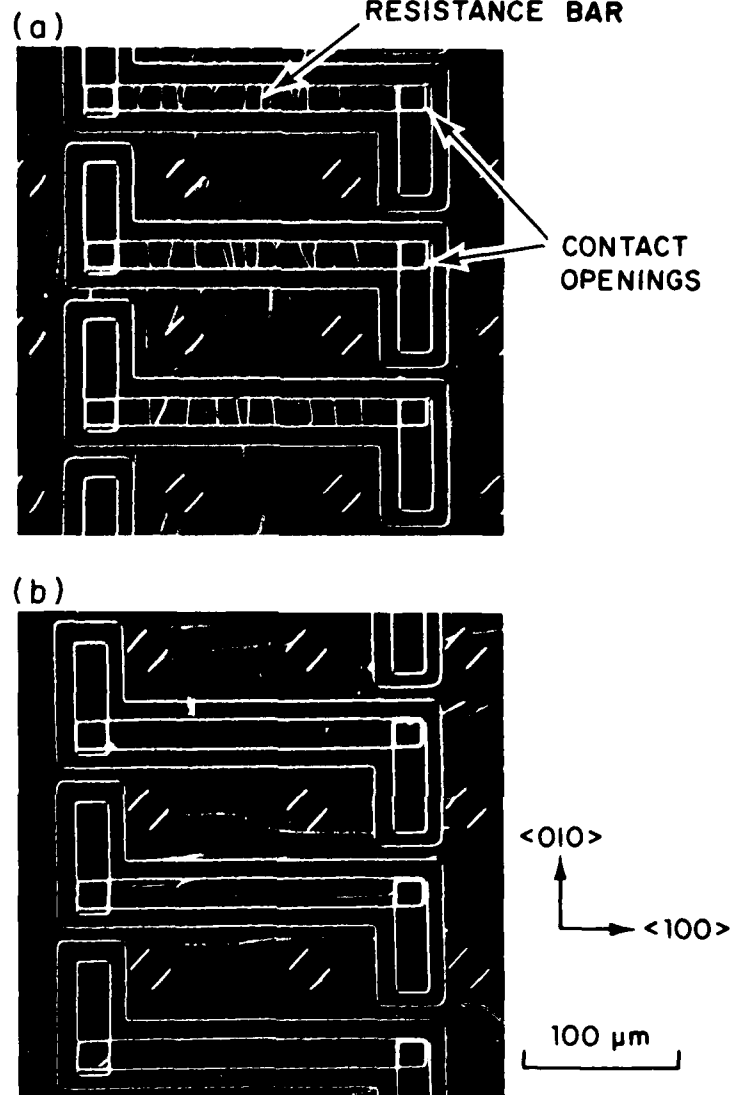


Fig. III-1. Photomicrographs of thin-film resistors fabricated in zone-melting-recrystallized Si films with electron transport (a) perpendicular and (b) parallel to sub-boundaries. Diamond-shaped features are etch pits showing in-plane orientation.

1. Majority-Carrier Transport

To investigate the effect of sub-boundaries on carrier transport in zone-melting-recrystallized Si films, we have made resistance measurements over the temperature range between -20° and $+80^{\circ}\text{C}$ on resistors that were fabricated with their long axis either approximately perpendicular or approximately parallel to the long axis of the sub-boundaries in recrystallized films $0.5\text{ }\mu\text{m}$ thick. To fabricate these devices, resistance bars with dimensions of 18 by $180\text{ }\mu\text{m}$ were defined by a complete moat etch isolation, uniform donor concentrations of $\sim 1 \times 10^{17}$ or $\sim 2 \times 10^{17}\text{ cm}^{-3}$ were produced by implantation of 150-keV P^{+} ions followed by annealing at 1000°C , and ohmic contacts were made by using P-diffusion at 950°C to form heavily doped regions at the ends of the bars, then depositing an Al film and sintering at 450°C . Figures III-1(a) and (b) are photomicrographs showing resistors that are respectively perpendicular and parallel to the sub-boundaries, which were delineated by etching after the resistance measurements were completed. In both cases, electron transport was parallel to a $\langle 100 \rangle$ direction. For the resistance measurements, we selected perpendicular resistors that were intersected by ten or eleven sub-boundaries and parallel resistors that did not contain any sub-boundaries.

Figure III-2 is a log-log plot showing the results of resistance vs temperature measurements for four sets of resistors. The carrier concentration n is $1 \times 10^{17}\text{ cm}^{-3}$ for two sets, $2 \times 10^{17}\text{ cm}^{-3}$ for the other two. For each concentration, one set is perpendicular to the sub-boundaries the other is parallel. Each data point represents an average value obtained from measurements on several resistors. In all cases, the resistance increases with temperature, in contrast to the results for resistors fabricated from CVD poly-Si films,⁴ which have negative temperature coefficients of resistance.

To determine the properties of the sub-boundaries, we have compared the data of Fig. III-2 for parallel and perpendicular resistors. For the former, the total resistance R is just the intragrain resistance R_G ; for the latter, R is the sum of R_G and the sub-boundary resistance R_{SB} . We assume that R_G is the same for parallel and perpendicular resistors with the same n , so that at

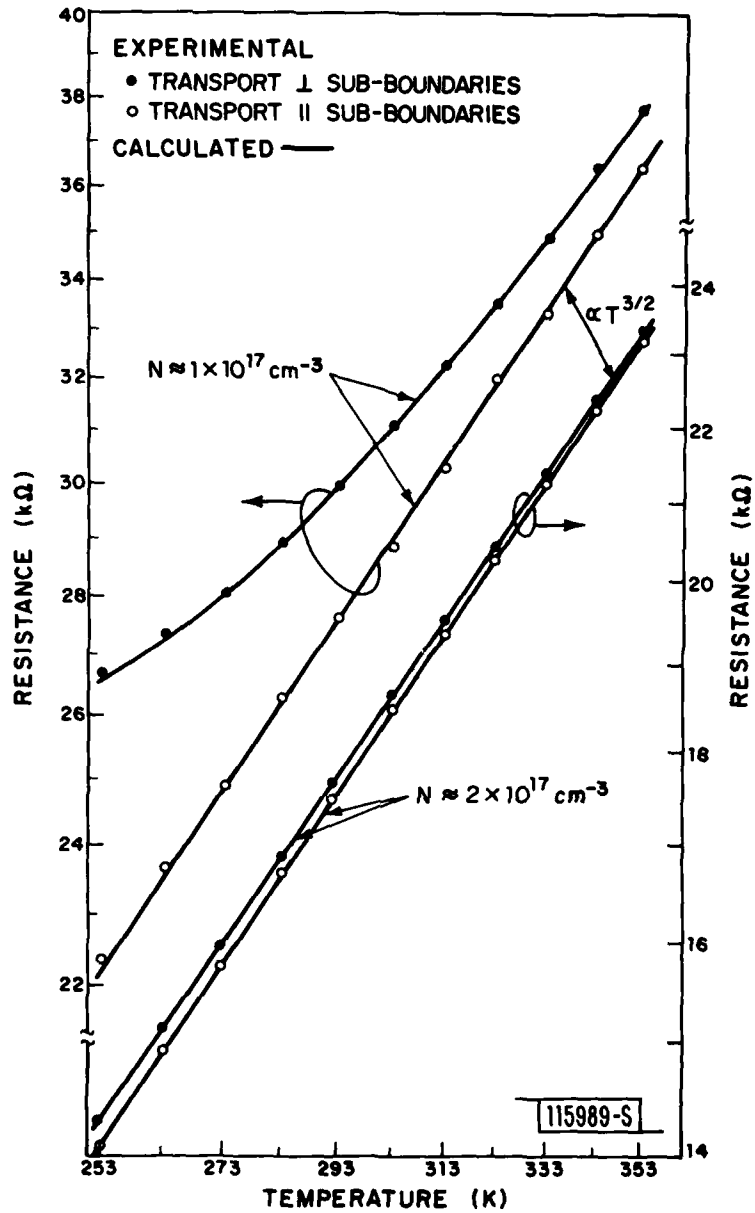


Fig. III-2. Log-log plot of resistance as a function of temperature for four sets of thin-film resistors.

a given temperature T the difference in resistance between the two types is equal to R_{SB} . Figure III-2 shows that R_{SB} is always much less than R_G .

In bulk Si with $n \sim 10^{17} \text{ cm}^{-3}$, over the temperature range studied here the carrier mobility varies approximately as $T^{-3/2}$ because acoustic phonon scattering is the dominant scattering mechanism. If this mechanism also dominates intragrain transport in the recrystallized films,

$$R_G(T) = R_{Go} \left(\frac{T}{300} \right)^{3/2} \quad (\text{III-1})$$

where R_{Go} is the value of R_G at 300 K. This relationship is confirmed by the results shown in Fig. III-2 for the two sets of parallel resistors, since the data are well fitted by straight lines of slope $3/2$. The values of R_{Go} for these lines are 2.85×10^4 and $1.82 \times 10^4 \Omega$ for n of 1×10^{17} and $2 \times 10^{17} \text{ cm}^{-3}$, respectively.

We now consider the perpendicular resistors. If the conventional charge-trapping model^{4,5} is applicable, charge will be trapped at each sub-boundary, producing a potential energy barrier to carrier transport. By using the transport equation for thermionic emission⁵ and assuming a discrete trapping level within the band gap,⁴ we obtain

$$R_{SB}(T) = R_{SBo} \left(\frac{T}{300} \right)^{1/2} \exp [\phi_{SB}/kT] \quad (\text{III-2})$$

where R_{SBo} is a constant, and ϕ_{SB} is the barrier height. The total resistance for a perpendicular resistor is obtained by adding Eqs. (III-1) and (III-2):

$$R(T) = R_{Go} \left(\frac{T}{300} \right)^{3/2} + R_{SBo} \left(\frac{T}{300} \right)^{1/2} \exp [\phi_{SB}/kT] \quad (\text{III-3})$$

For the resistors we have studied, the temperature coefficient of R is positive because the first term on the right side is much larger than the second.

In confirmation of Eq. (III-3), we have found that this equation gives an excellent fit to the experimental results for the perpendicular resistors. The curves in Fig. III-2 for the two sets of these resistors were calculated from Eq. (III-3) by using the values of R_{Go} given above for the parallel resistors of the same n and adjusting the values of R_{SBo} and ϕ_{SB} to give the best fit to the data. For $n = 1 \times 10^{17} \text{ cm}^{-3}$, the values obtained for R_{SBo} and ϕ_{SB} are, respectively, 36.1Ω and 0.17 eV ; for $n = 2 \times 10^{17} \text{ cm}^{-3}$, they are 18.1Ω and 0.058 eV . The values of R_{SBo} differ by a factor of two. We have derived this inverse relationship between R_{SBo} and n from barrier-resistance theory.

Since the depletion width associated with each sub-boundary is much less than the distance between adjacent sub-boundaries, the sub-boundary trapping states will be completely filled. In this case the trapping-state density Q_t is related to ϕ_{SB} by:

$$Q_t^2 = \frac{8\epsilon n}{q^2} \phi_{SB} \quad (\text{III-4})$$

where ϵ is the dielectric constant of Si (see Ref. 4). From the ϕ_{SB} values obtained for $n = 1 \times 10^{17}$ and $2 \times 10^{17} \text{ cm}^{-3}$, Eq. (III-4) gives Q_t values of 7.48×10^{11} and $7.78 \times 10^{11} \text{ cm}^{-2}$, respectively. These values, which agree within experimental error, are substantially lower than those of 2 to $4 \times 10^{12} \text{ cm}^{-2}$ reported for CVD poly-Si films.^{4,6} This difference is not surprising, since the degree of disorder should be less at the sub-boundaries than at grain boundaries.

The effect of sub-boundaries on carrier transport has also been studied by measuring the room-temperature surface electron mobilities in two sets of n-channel MOSFETs, which were fabricated in configurations such that electron transport is parallel to the sub-boundaries in one set and perpendicular in the other. The devices have a gate width and gate length of $45 \mu\text{m}$ and channel doping concentration of $5 \times 10^{15} \text{ cm}^{-3}$ produced by implantation of B-ions followed by thermal annealing. For each set of transistors, Fig. III-3 shows the distribution of mobility measured for 92 randomly selected devices. The

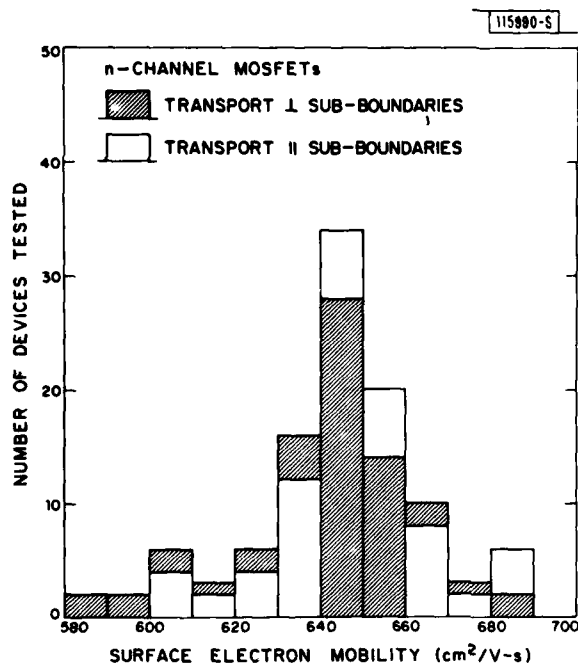
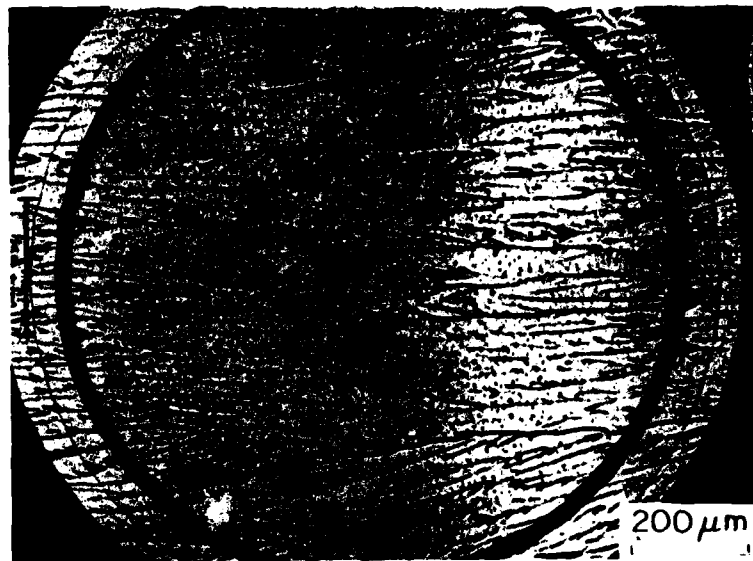
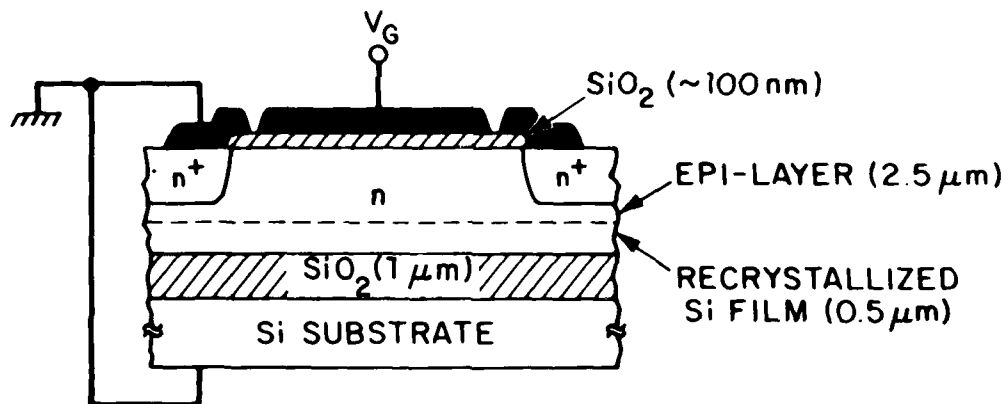


Fig. III-3. Distribution of surface electron mobility for n-channel MOSFETs fabricated in zone-melting-recrystallized Si films with electron transport either parallel or perpendicular to sub-boundaries.

devices with electron transport parallel to the sub-boundaries exhibit an average mobility of $647 \text{ cm}^2/\text{V-s}$, with a standard deviation of $18 \text{ cm}^2/\text{V-s}$. The corresponding values for the other set are 635 and $22 \text{ cm}^2/\text{V-s}$. The mobility difference is very small, although the active region in each of the devices with perpendicular transport should be intersected by three to five sub-boundaries. This result is consistent with the sub-boundary parameters determined from the data for the thin-film resistors. Since the electron concentration in the strongly inverted surface layer of the MOSFETs is very high ($>10^{18} \text{ cm}^{-3}$), the values of R_{SBO} and ϕ_{SB} in this layer should be quite small.



(a)



(b)

115991-R

Fig. III-4. (a) Photomicrograph showing surface of MOS capacitor fabricated in Si epilayer grown on zone-melting-recrystallized Si film. (b) Schematic cross-sectional diagram of epilayer MOS capacitor.

2. Generation Lifetime

For bipolar device applications, the lifetime is a key parameter in determining the gain and speed. Even for such majority-carrier devices as MOSFETs, the minority-carrier lifetime is significant because it sets a lower limit on the leakage current of the reverse-biased drain junction. This current is especially important in complementary MOS circuits, where it determines the minimum quiescent power dissipation.

We have measured the generation lifetimes both in zone-melting-recrystallized Si films and in epitaxial Si layers grown by CVD on such films. The Si epilayers, $\sim 2.5 \mu\text{m}$ thick, were grown in a commercial RF-heated horizontal reactor. In each deposition run, control epilayers were grown on Sb-doped single-crystal Si<100> wafers. Prior to epitaxial growth, some of the recrystallized films were doped with As to a concentration of $\sim 10^{20} \text{ cm}^{-3}$ by ion implantation followed by furnace annealing. Growth was carried out at 1040°C by pyrolysis of silane in a H_2 stream containing sufficient PH_3 doping gas to yield n-type epilayers with a carrier concentration of $\sim 2 \times 10^{15} \text{ cm}^{-3}$. This concentration and the layer thickness were selected to produce structures suitable for the fabrication of bipolar transistors. Although the recrystallized Si films are mirror-smooth, the epilayers grown on them have distinct linear surface features, which are shallow grooves located above the sub-boundaries in the films. These features are illustrated by Fig. III-4(a), which is a photomicrograph of the surface of an MOS capacitor fabricated in one of the epilayers.

Planar MOS capacitors were fabricated both in the recrystallized Si films and in the epilayers. Figure III-4(b) is a schematic cross-sectional diagram showing the structure of an epilayer device. Selective P-diffusion was first carried out at 950°C to produce heavily doped n^+ regions surrounding the gate area for ohmic-contact formation. Gate oxide $\sim 100 \text{ nm}$ thick was then grown in a dry O_2 ambient. Contacts were opened and a $1\text{-}\mu\text{m}$ -thick Al film was deposited and defined over the gate and contact areas. The devices were finally annealed at 450°C for 30 min. in H_2 .

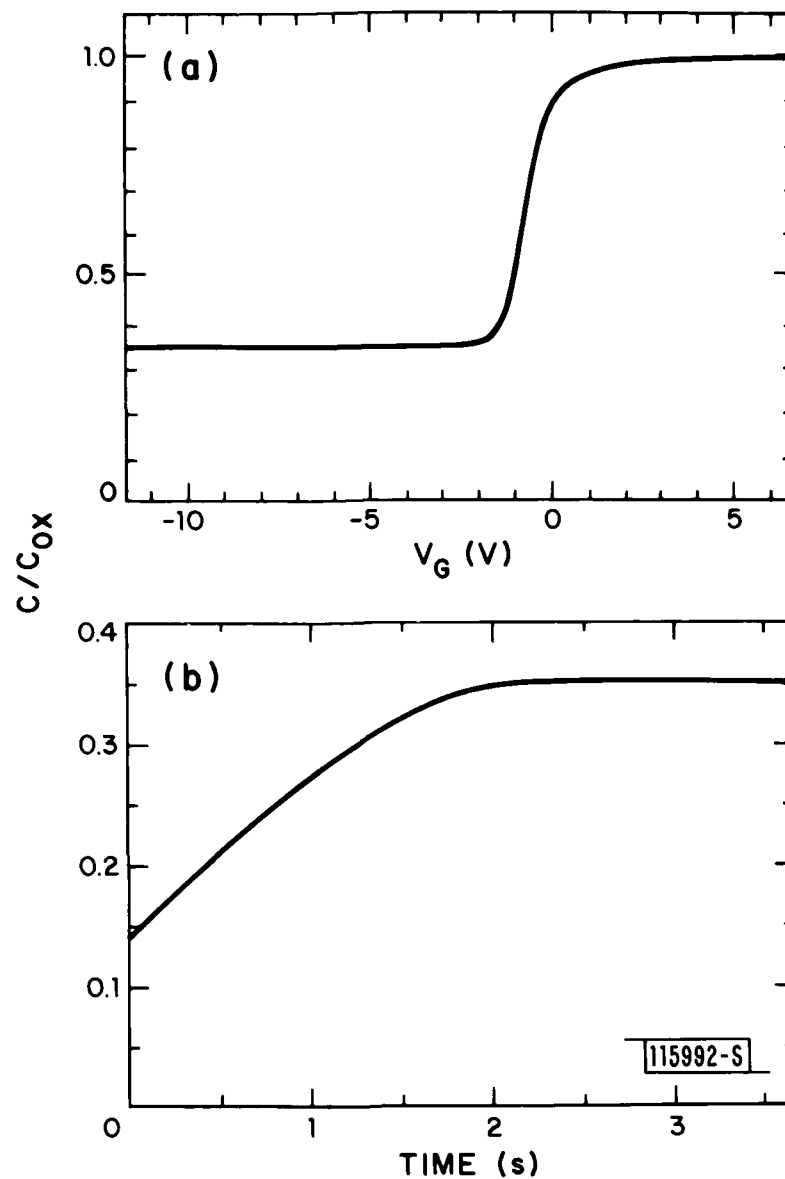


Fig. III-5. Ratio of capacitance (C) to oxide capacitance (C_{ox}) for epilayer MOS capacitor. (a) Dependence on gate voltage (V_G); (b) dependence on time after applying step bias of -20V.

Figure III-5(a) shows a typical high-frequency C-V curve for an epilayer MOS capacitor. The doping concentration N_D in the epilayer, as determined from the ratio of inversion-state capacitance to accumulation-state capacitance, is $\sim 2 \times 10^{15} \text{ cm}^{-3}$. A fixed oxide-charge density of $\sim 3 \times 10^{10} \text{ cm}^{-2}$ is deduced from the flat-band voltage, indicating good oxide quality.

The generation lifetime was measured by the pulsed MOS capacitor technique,⁷ in which the device is pulse biased into deep depletion and relaxes to its quasi-equilibrium inversion state as a result of thermal generation. Surface generation is eliminated by the H_2 annealing step (Ref. 7), so that only the bulk lifetime is measured. This lifetime is given by the expression⁷

$$\tau_g = \frac{n_i}{8N_D} \cdot \frac{C_F}{C_{ox}} \left(1 + \frac{C_I}{C_F} \right)^2 t_F \quad (\text{III-5})$$

where C_I , C_F , and C_{ox} are the depletion (initial), inversion (final), and accumulation (oxide) capacitance, respectively, n_i is the intrinsic carrier concentration, and t_F is the time required for the capacitance to change from C_I to C_F . Figure III-5(b) shows a typical C-t capacitor response curve obtained after applying a step bias of -20V. The value of τ_g obtained from Eq. (III-5) is 1.3 μs .

Lifetime measurements have also been carried out for MOS capacitors fabricated directly in the recrystallized Si films. Since the films are only about 0.5 μm thick, to prevent depletion under the pulsed bias condition the value of N_D was increased to $\sim 1 \times 10^{17} \text{ cm}^{-3}$ by implantation of 150-keV P^+ ions and annealing at 1000°C. For this value of N_D , the depletion width is $\sim 0.4 \mu\text{m}$ under a -20-V pulsed bias condition. The generation lifetimes measured for the films are in the range of 0.2 to 0.5 μs .

Generation lifetimes in the recrystallized films have also been deduced from the p-n junction leakage currents measured for n-channel MOSFETs fabricated by a standard self-aligned poly-Si gate technique.³ The devices have a p-type channel doping concentration of $\sim 1 \times 10^{16} \text{ cm}^{-3}$. The leakage current

TABLE III-1 GENERATION LIFETIMES IN Si RECRYSTALLIZED FILMS AND EPILAYERS			
Structure†	Doping Concentration and Type (cm ⁻³)	τ_g (μ s)	Method§
r-Si/SiO ₂ /Si<100>	r-Si 1 x 10 ¹⁷ (n)	0.2 to 0.5	C-t
r-Si/SiO ₂ /Si<100>	r-Si 1 x 10 ¹⁶ (p)	>1.0	I-V
e-Si/r-Si/SiO ₂ /Si<100>	e-Si 2 x 10 ¹⁵ (n) r-Si (undoped)	0.9 to 1.3	C-t
e-Si/r-Si/SiO ₂ /Si<100>	e-Si 2 x 10 ¹⁵ (n) r-Si ~1 x 10 ²⁰ (n)	0.8 to 1.3	C-t
e-Si/Si<100>	e-Si 2 x 10 ¹⁵ (n) Si<100> >1 x 10 ²⁰ (n)	1.5 to 2.2	C-t
†r-Si = recrystallized film, e-Si = epilayer. §C-t = pulsed MOS capacitor, I-V = p-n junction leakage current.			

density J measured at -5 V drain bias is typically $\sim 3 \times 10^{-7}$ A/cm², but values as low as 8×10^{-8} A/cm² have been measured. According to Ref. 8, the lifetime is given by $\tau_g = qn_1 W / 2J$, where W is the junction depletion width. For $J = 8 \times 10^{-8}$ A/cm², τ_g is calculated to be $1.2 \mu\text{s}$. This value should be considered as a lower limit, since the leakage current is partially due to electron conduction near the lower Si-SiO₂ interface.

Table III-1 summarizes the generation-lifetime data for various sample structures. The values for each structure were obtained from measurements on more than ten randomly selected devices. The lifetimes in epilayers grown on the recrystallized Si films are comparable to those in control layers grown on single-crystal Si wafers and are substantially higher than the values of 1 to 40 ns reported for conventional Si-on-sapphire materials.⁹ The observation of generation lifetimes in the microsecond range for both the recrystallized films and the epilayers grown on them suggests that the defects in these materials are not very effective trapping centers. If the recombination lifetimes also have comparable values, SOI structures prepared by zone-melting recrystallization and subsequent epitaxial growth are potentially useful for bipolar-device applications.

B-Y. Tsaur	D.J. Silversmith
J.C.C. Fan	R.W. Mountain
M.W. Geis	

B. PREPARATION OF ORIENTED GaAs BICRYSTAL LAYERS BY VAPOR-PHASE EPITAXY USING LATERAL OVERGROWTH

The increasing utilization of polycrystalline semiconductors for various device applications has stimulated numerous investigations of the electronic properties of grain boundaries (GBs). It has been found that these properties are influenced by both GB structure and composition, but detailed study of structural effects has been limited. A systematic experimental study of these effects requires the availability of samples containing GBs that have well-specified structures with geometries suitable for electronic characterization.

Nine parameters are required for completely specifying the geometrical structure of an ideal GB between two crystals: three orthogonal axes defining a reference coordinate system that is associated with one of the crystals, three angles by which the second crystal is rotated about these axes with respect to the first, and the three coordinates of the boundary plane in the reference system. This report describes a novel technique that utilizes vapor-phase epitaxy to grow bicrystal layers in which these parameters are all determined. As an initial demonstration of this technique, we have grown a series of GaAs bicrystals in each of which the boundary plane is a $(\bar{1}11)$ plane and the two crystals are rotated with respect to each other about a $[110]$ axis, but not about the other two orthogonal axes. Thus, the GBs are $[110]$ tilt boundaries with structures differing only in the magnitude of the $[110]$ rotation angle, which we designate as the misorientation angle θ . Initial electrical measurements indicate that there is a potential barrier associated with each GB whose height varies with θ .

The GaAs bicrystals are grown on composite substrates prepared by bonding two appropriately oriented GaAs crystals that are cut from a single-crystal boule. As shown schematically in Fig. III-6, the crystals have (110) faces, and cross sections for bonding are cut perpendicular to these faces. For the reference crystal, which we also designate as Crystal 1, the cross section is a $(\bar{1}11)$ plane; for Crystal 2, the cross section is an off- $(\bar{1}11)$ plane that is rotated about the $[110]$ direction by the desired misorientation angle. The cross sections are then polished, and the crystals are encapsulated with a thin layer of phosphosilicate glass. One of the cross sections is coated with photoresist containing particles of a $\text{PbO-SiO}_2\text{-Al}_2\text{O}_3$ glass. The cross sections are placed in contact, and the crystals are pressed together and heated in air to above 810°C , the melting point of the glass. During this process the photoresist is volatilized, and the crystals are bonded together by a continuous glass film about $5\text{ }\mu\text{m}$ thick. After cooling, the composite formed is cut into wafers $750\text{ }\mu\text{m}$ thick with (110) surfaces. One such wafer is shown schematically in the upper diagram of Fig. III-7. The upper (110) surface is lapped, polished, and coated by

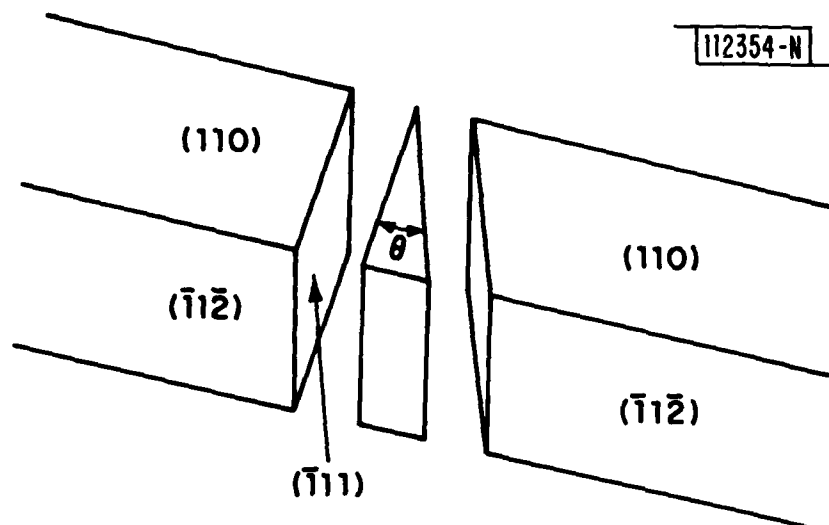


Fig. III-6. Geometry of single crystal cut to form component crystals of substrate for epitaxial growth of bicrystal layer with $[110]$ tilt boundary.

chemical vapor deposition with an SiO_2 layer $0.2 \mu\text{m}$ thick. To complete preparation of the substrate, an SiO_2 stripe $35 \mu\text{m}$ wide that runs along the length of the bonded interface is defined photolithographically. As shown in the upper diagram of Fig. III-7, this stripe masks the bonding glass film and extends $15 \mu\text{m}$ over each of the GaAs crystals.

Except for the use of composite substrates, the procedure for obtaining GaAs bicrystals is essentially the same as the one we have employed previously for preparing single-crystal GaAs layers over insulating films by means of lateral overgrowth using the $\text{AsCl}_3\text{-GaAs-H}_2$ method of vapor-phase epitaxy.¹⁰⁻¹² Deposition of GaAs is carried out under conditions selected so that nucleation of GaAs growth occurs on the exposed (110) surface of Crystals 1 and 2, but not on the SiO_2 masking stripe. When the thickness of the GaAs epilayers on the crystals exceeds that of the SiO_2 , these layers seed

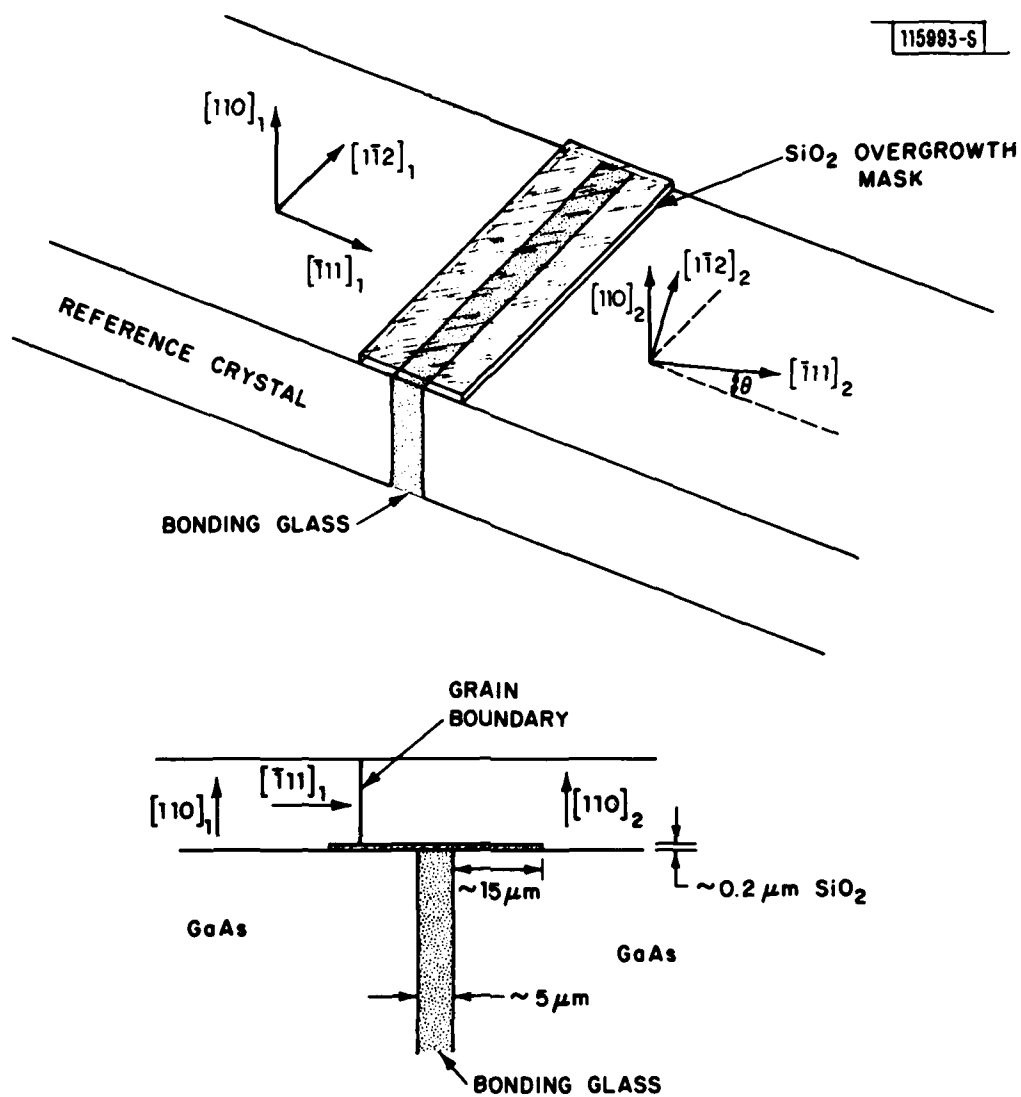


Fig. III-7. Schematic diagrams of composite substrate (top) and cross section of substrate and bicrystal layer grown by vapor-phase epitaxy (bottom).

lateral growth over the stripe. This overgrowth continues simultaneously with vertical growth until the two layers merge to form a continuous film, after which growth proceeds normally. The lateral growth seeded by Crystal 1 is bounded by a slow-growing ($\bar{1}11$) facet. Since the GB in the bicrystal is located where the two lateral growths merge, as shown in the lower diagram of Fig. III-7 the GB plane is a ($\bar{1}11$) plane, regardless of the misorientation angle of Crystal 2.

Three nominally undoped bicrystal layers about 30 μm thick - containing [110] tilt boundaries with θ of approximately 10°, 24°, and 30° - were prepared in a single deposition run with a growth time of 7 h at a substrate temperature of 720°C. A control sample, which we designate as a "0° bicrystal," was grown in the same run on a composite substrate formed from two crystals - both having bonding cross sections cut 10° from the ($\bar{1}11$) plane. The crystals used to form the substrates were all cut from the same nominally undoped, high-resistivity p-type GaAs boule. A conventional epilayer grown during the same deposition run on a single-crystal (110) substrate was found to be n-type with a carrier concentration of $1 \times 10^{15} \text{ cm}^{-3}$.

Laue back-reflection x-ray diffraction photographs were taken for the four bicrystals. Each photograph shows two (110) patterns rotated with respect to each other by the angle θ about the [110] tilt axis. In each case, the [110] poles are slightly displaced from each other, indicating a deviation of less than 1° from the pure tilt orientation. The values of θ measured from the Laue patterns are 10.1°, 24.0°, and 30.5°, with an estimated uncertainty of 0.5°, compared with intended values of 10°, 25°, and 30°.

Figure III-8 shows Nomarski interference contrast micrographs taken of the as-grown surfaces of the 0° and 24° bicrystal layers. Similar micrographs were obtained for the other two bicrystals. In each case the trace of the GB is quite straight, indicating that the rate of lateral growth for each component crystal was uniform along the length of the SiO_2 stripe. Matching series of parallel straight lines that can be attributed to surface faceting during growth are observed for the two crystals, with the corresponding pairs of lines meeting along the GB at the angle θ .

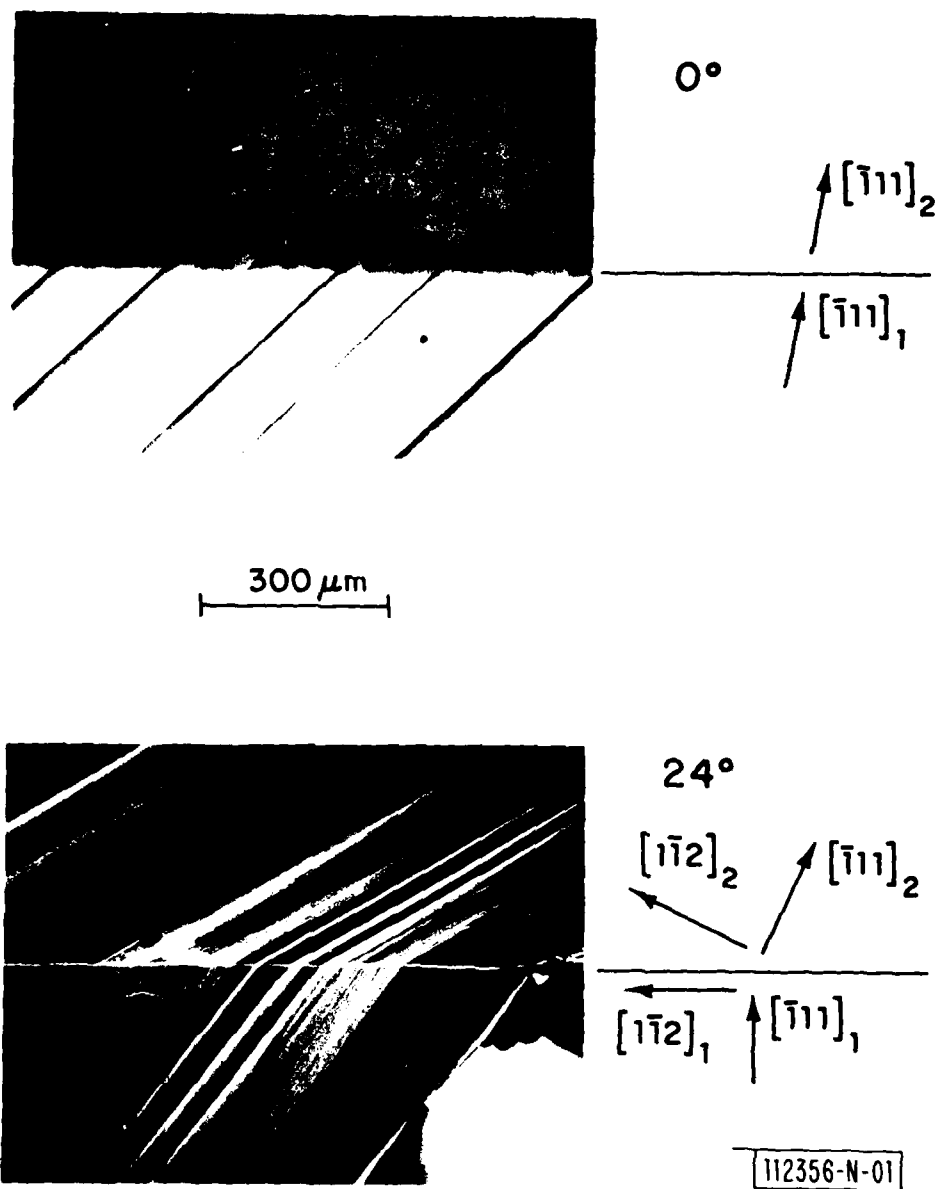


Fig. III-8. Nomarski contrast micrographs of as-grown bicrystal layers with 0° and 24° $[110]$ tilt boundaries.

For electrical measurements on each of the bicrystals, specimens 1.5 mm wide and 5 mm long were prepared by making a series of saw cuts perpendicular to the GB and extending through the bicrystal layer and substrate. A mesa about 0.5 mm wide, bisected by the GB, was then defined by masking the grown surface and etching down to the substrate. Four ohmic contacts, two on each crystal, were prepared by alloying Sn dots to the mesa at 300°C.

Figure III-9 shows the I-V curves obtained by measurements across the GB in the 0°, 10°, and 24° bicrystals. For the 0° bicrystal the curve is linear, showing that no potential barrier is present. The other two curves have a strongly nonlinear form characteristic of back-to-back diodes. This behavior indicates the existence of a potential barrier due to trapped charge at the GB. Both curves are asymmetric, probably due to differences in carrier concentration between the two component crystals that result because the rate of dopant incorporation during lateral growth varies with crystallographic orientation.¹² The curves are plotted so that the portion in the first quadrant shows the behavior obtained when a positive bias was applied to the (111) reference crystal. For this portion the breakdown voltage is much higher for the 24° bicrystal than for the 10° one, indicating that the potential barrier increases with increasing θ , as might be expected.

J.P. Salerno
R.W. McClelland
P. Vohl

J.C.C. Fan
W. Macropoulos
C.O. Bozler

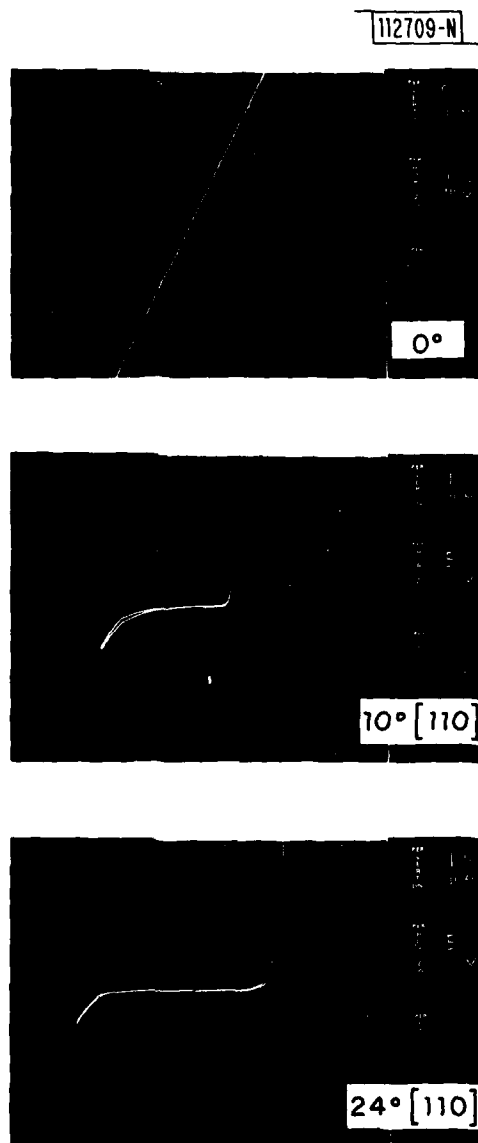


Fig. III-9. Current-voltage characteristics measured across [110] tilt boundaries with $\theta = 0^\circ$, 10° , and 24° .

REFERENCES

1. M.W. Geis, B-Y. Tsaur, J.C.C. Fan, D.J. Silversmith, R.W. Mountain, J.P. Donnelly, E.W. Maby, and D.A. Antoniadis, 39th Annual Device Research Conference, Santa Barbara, California, 22-24 June 1981.
2. M.W. Geis, H.I. Smith, B-Y. Tsaur, J.C.C. Fan, E.W. Maby, and D.A. Antoniadis, Appl. Phys. Lett. 40, 158 (1982).
3. B-Y. Tsaur, M.W. Geis, J.C.C. Fan, D.J. Silversmith, and R.W. Mountain, Appl. Phys. Lett. 39, 909 (1981), DTIC AD-A113234.
4. See, for example, J.Y.W. Seto, J. Appl. Phys. 46, 5247 (1975).
5. C.H. Seager and T.G. Castner, J. Appl. Phys. 49, 3879 (1978).
6. N.C.C. Lu, L. Gerzberg, and J.D. Meindl, IEEE Electron Device Lett. EDL-1, 38 (1980).
7. D.K. Schroder and J. Guldberg, Solid-State Electron. 14, 1285 (1971).
8. A.S. Grove, in Physics and Technology of Semiconductor Devices (Wiley, New York, 1967), Chap.6.
9. D. Kranzer, Appl. Phys. Lett. 25, 103 (1974).
10. R.W. McClelland, C.O. Bozler, and J.C.C. Fan, Appl. Phys. Lett. 37, 560 (1980), DTIC AD-A101024/8.
11. C.O. Bozler, R.W. McClelland, and J.C.C. Fan, IEEE Electron Device Lett. EDL-2, 203 (1981).
12. C.O. Bozler, R.W. McClelland, J.P. Salerno, and J.C.C. Fan, J. Vac. Sci. Technol. 20, 720 (1982).

IV. MICROELECTRONICS

A. VERTICAL SINGLE-GATE CMOS INVERTERS ON LASER-PROCESSED MULTILAYER SUBSTRATES

Complementary MOS (CMOS) logic is important because, for a given minimum feature technology, it consumes less power than any other MOS logic configuration. This advantage is gained at the expense of substrate area per logic unit. The joint-gate CMOS (JCMOS) logic configuration offers a solution to this problem because nMOS and pMOS transistors are stacked vertically to save substrate area. The feasibility of this logic configuration was first reported by Gibbons and Lee.¹ The JCMOS inverter reported here differs from the earlier design because it is fabricated from the top down rather than from the bottom up in order to achieve self-alignment. Moreover, by using the top-down fabrication procedures one can avoid lateral diffusion of the p⁺ source and drain regions of the lower pMOS transistor during both laser recrystallization of the upper polysilicon layer and n⁺ source-drain formation for the nMOS transistor.

Fabrication of the JCMOS inverter starts with an n-type <100> 5- to 10- Ω -cm substrate. A 1000- \AA thermal oxide is grown, followed by a 1- μm deposition of LPCVD polysilicon to serve as the gate electrode of both pMOS and nMOS transistors. The gate polysilicon is heavily ion-implanted with boron ($2.5 \times 10^{18} \text{ cm}^{-3}$) in order to allow fabrication of an upper nMOS transistor with reduced vertical electric field after threshold voltage adjustment by ion implantation.² Next, a gate oxide of 1500 \AA is thermally grown over the polysilicon joint gate. A 7500- \AA layer of amorphous silicon is deposited over this gate oxide to serve as the active region for the nMOS transistor following recrystallization. A threshold adjustment implant provides for an ultimate boron background concentration of $1.33 \times 10^{16} \text{ cm}^{-3}$. Laser recrystallization is performed with a scanning CW argon laser at a power density of $7 \times 10^5 \text{ W/cm}^2$ and a scanning speed of 4 cm/s. An additional 1500- \AA layer of polysilicon is deposited for consumption by an oxidation step that appears later in this process sequence. Finally, a 500- \AA layer of CVD

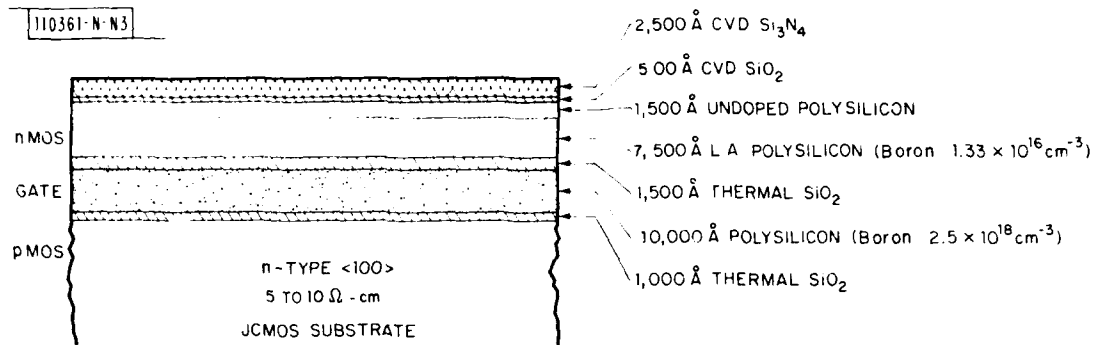


Fig. IV-1. Multilayer substrate prepared for stacked JCMOS device fabrication.

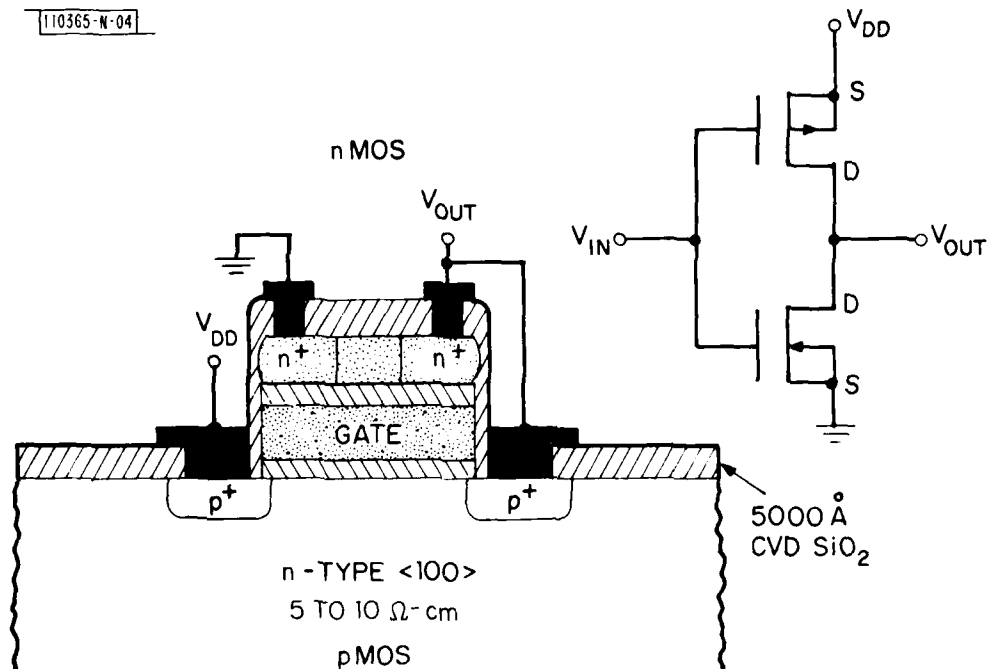


Fig. IV-2. Cross section of a completed vertically stacked CMOS structure showing how nMOS and pMOS devices are interconnected to form JCMOS inverter.

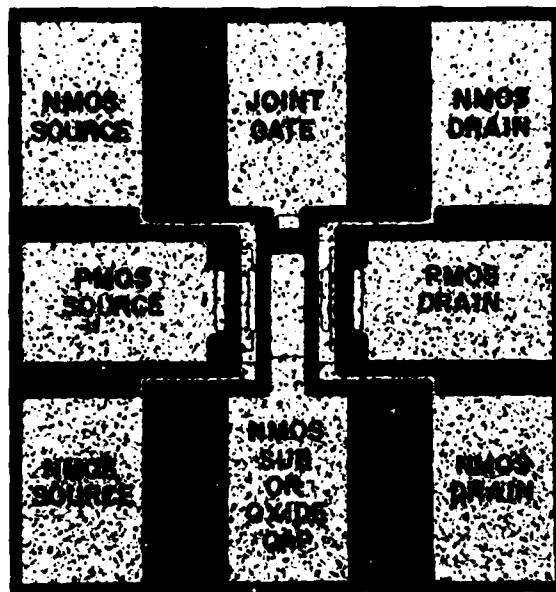


Fig. IV-3. Top view of completed JCMOS inverter.

SiO_2 is deposited, followed by a 2500-Å layer of CVD Si_3N_4 . Figure IV-1 shows the "wedding-cake" structure that is created by the preceding processing steps.

The detailed fabrication sequence for the JCMOS inverter is described elsewhere.³ The inverter uses six masks in a self-aligned, top-down process. The gate-width to gate-length ratio (W/L) was 88/38 μm for the nMOS upper device and 88/60 μm for the pMOS lower device. A cross section of the completed structure is shown in Fig. IV-2, and a top view of the finished device is given in Fig. IV-3.

Figures IV-4(a) and (b) show typical source-drain characteristics of the nMOS and pMOS transistors, respectively. Analysis of the nMOS devices yielded an average surface electron mobility of 200 $\text{cm}^2/\text{V-s}$ and an average threshold voltage of +3.8 V. Analysis of the pMOS devices yielded an average surface hole mobility of 230 $\text{cm}^2/\text{V-s}$ and an average threshold voltage of -2.5 V.

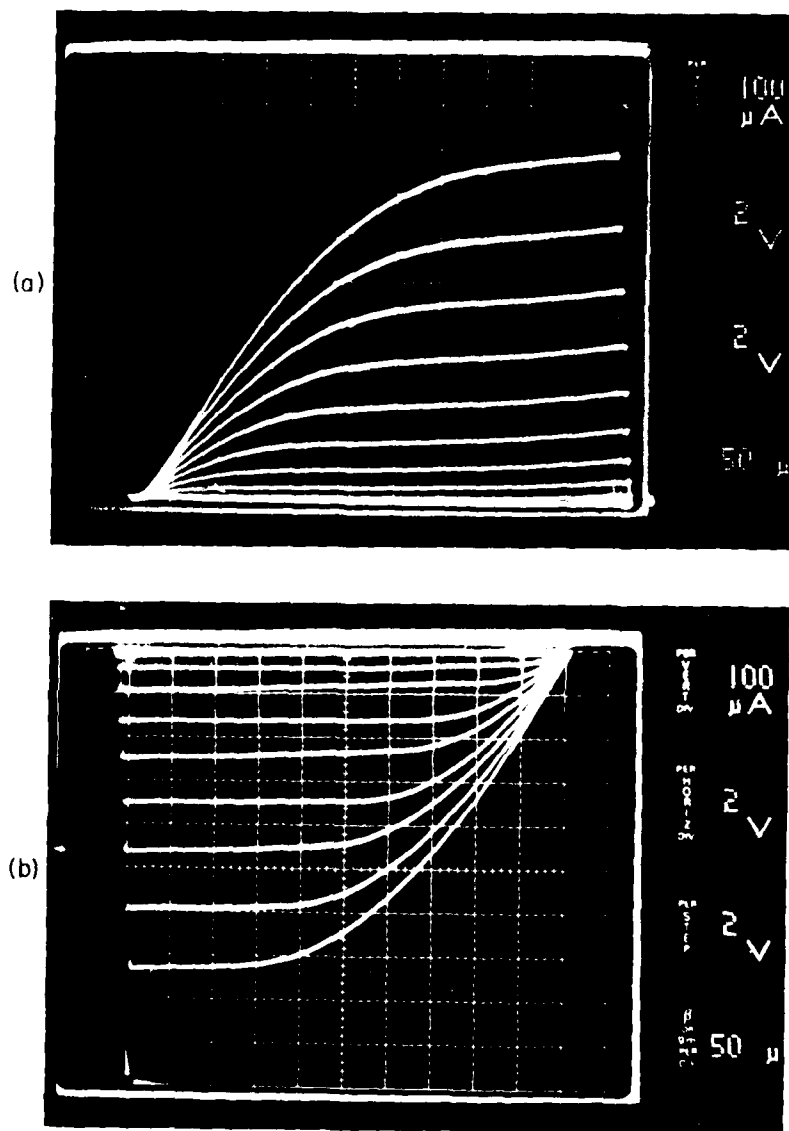


Fig. IV-4. (a) nMOS and (b) pMOS I-V characteristics as measured on a typical JCMOS inverter.

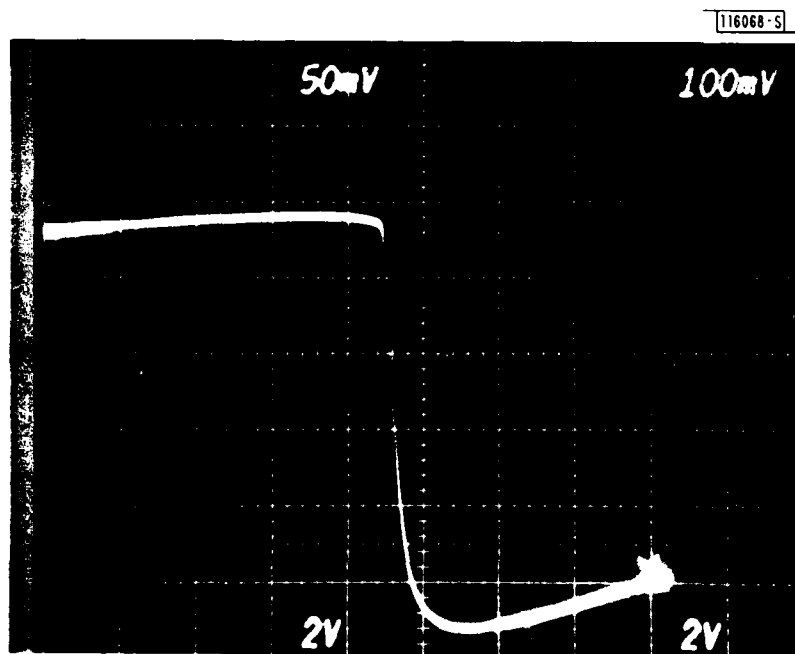


Fig. IV-5. Transfer curve for JCMOS inverter. Each major division in X (input) and Y (output) is 2 V. Zero input corresponds to left-hand axis, while zero corresponds to y-axis baseline.

The inverter transfer curve shown in Fig. IV-5 is the characteristic displayed by the JCMOS inverter when connected as shown in Fig. IV-2. The low frequency gain is -12.5. The increasing voltage in the output logical zero state is due to gate oxide leakage in the lower pMOS device. This problem may be related to the recrystallization procedure that was chosen.

JCMOS inverter rise and fall times are typically 2 μ s, limited both by the relatively poor ($\sim 200 \text{ cm}^2/\text{V}\cdot\text{s}$) surface electron mobility in the top-layer recrystallized nMOS device and by the high parasitic capacitance ($\sim 1 \text{ pF}$) inherent in this type of 3-D structure. The effects of parasitic capacitance can be significantly reduced, in part, by appropriate layout design and W/L scaling. A 4- μm -channel-length technology yields a JCMOS inverter with

approximate 40- x 8- μ m dimensions. Improved recrystallization procedures offer promise for more favorable surface electron mobility.

G.T. Goeloe
E.W. Maby†
D.J. Silversmith

R.W. Mountain
D.A. Antoniadis†

B. HIGH-RESOLUTION ION-BEAM LITHOGRAPHY

Ion-beam exposure of resists is a promising new lithographic technique for the reproduction of patterns having submicrometer features.⁴⁻⁶ Both high resolution and short exposure times should be possible. The main difficulty is the development of a suitable mask technology which will provide sufficient contrast with a minimum of scattering of the incident beam. Rensch et al.⁶ have reported the replication of ~ 0.5 - μ m features with an estimated resolution of < 0.1 μ m by exposing PMMA through an open transmission mask. Karapiperis and Lee⁷ have fabricated 400-Å slots in PMMA by exposing it through an open conformable gold mask. In this report, we describe a reusable membrane mask for protons which we have used to replicate lines as small as 600 Å.

A proton mask, like an x-ray mask, has transparent and opaque areas which define the pattern to be replicated. In the case of protons, the materials which might be used as the opaque absorber differ by only about a factor of two⁸ in their stopping power compared with resist materials such as PMMA. Therefore, to produce high-aspect-ratio structures in resist, the mask must also have high-aspect-ratio structures.

The mask which was developed for these experiments is shown in Fig. IV-6. It consists of a single polyimide membrane⁹ 1 to 2 μ m in thickness. The pattern to be replicated is defined as a surface relief

†Department of Electrical Engineering and Computer Science, M.I.T.



ABSORBER - 1-2 μm POLYIMIDE
 MEMBRANE - 0.5-1 μm POLYIMIDE
 FABRICATION - OXYGEN R.I.E.

Fig. IV-6. Polyimide membrane mask structure. Pattern to be replicated is defined as a surface relief structure. Protons are stopped in thick areas of mask but pass through thin areas, exposing resist.

structure on the membrane. The detailed fabrication sequence is illustrated in Fig. IV-7. Oxygen reactive-ion etching¹⁰ (R.I.E.) is used to fabricate high-aspect-ratio structures in the polyimide. Contrast for the proton exposure of resist is provided by the modulation in membrane thickness, the polyimide acting as both absorber and support membrane. The stopping power of polyimide was determined by measuring the transmission of protons through membranes of known thickness as a function of incident beam energy. The results for three membrane thicknesses are shown in Fig. IV-8. From these measurements we assign a nominal value of 100 keV/ μm for the stopping power of polyimide for protons in the energy range of 50 to 200 keV. This value, along with the value of 125 keV/ μm for PMMA,¹¹ allows the design of an appropriate mask structure.

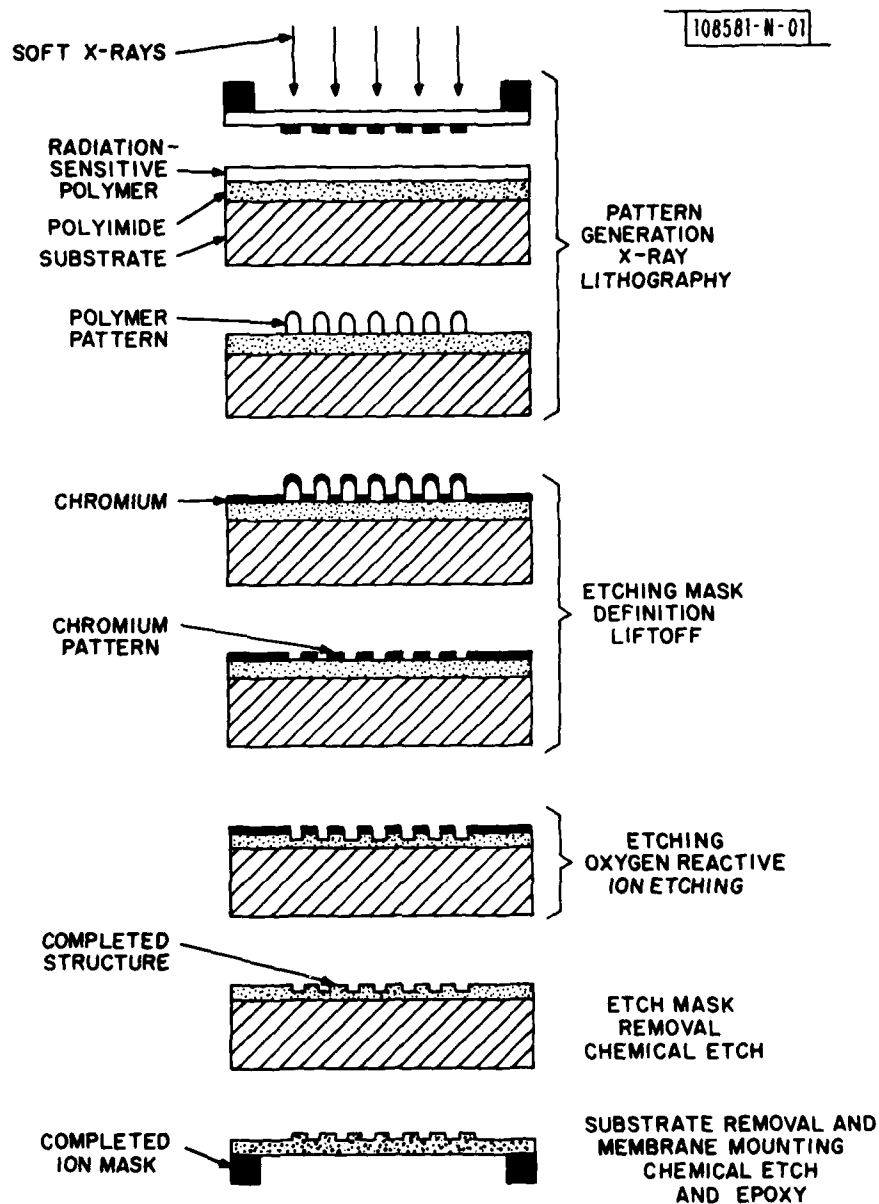


Fig. IV-7. Mask fabrication procedure. Pattern is originally defined in PMMA by x-ray lithography and a Cr liftoff is performed. Cr acts as a mask for oxygen R.I.E. of polyimide.

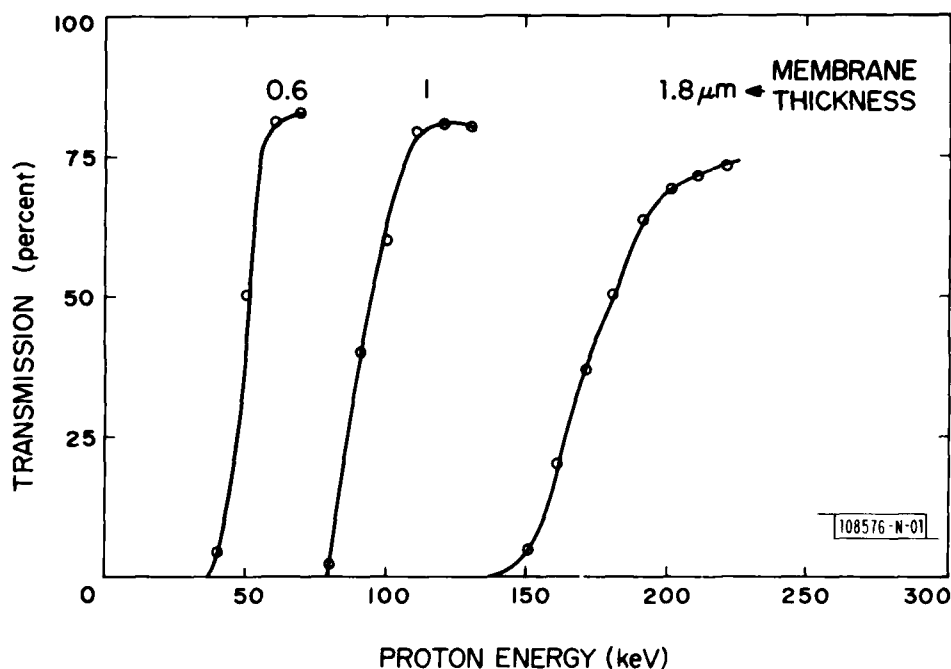


Fig. IV-8. Proton transmission vs energy. Transmission curves for three membrane thicknesses are shown. Stopping power of polyimide for protons in energy range of 50 to 200 keV is ~ 100 keV/ μm .

The exposure process is shown schematically in Fig. IV-9. A conventional ion-implantation system is used to generate a beam of protons whose energy can be varied from 40 to 400 keV. The beam is incident on the polyimide membrane mask, which is held in contact with a PMMA-coated substrate. Beam energy is selected so that the protons are stopped in the thick areas of the mask but pass through the thin areas, emerging with sufficient energy to expose the PMMA. The optimal combination of proton dose and development parameters was determined empirically. A dose of 2×10^{13} H^+/cm^2 , followed by development for 45 s in a 40-percent methyl isobutyl ketone, 60-percent isopropyl alcohol solution yielded the best results. All the exposure results reported here were obtained using this set of dose-development

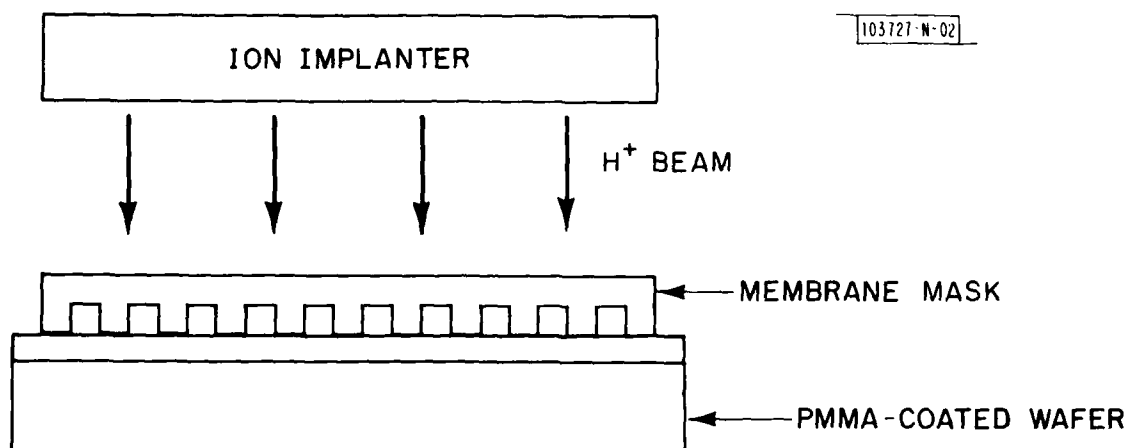


Fig. IV-9. Exposure process. An ion-implantation system is used to flood-expose mask and wafer with a collimated proton beam.

conditions. In addition, it was found that loss of contact between the mask and wafer occurred unless the mask was placed with the relief structure facing the PMMA (as shown in Fig. IV-9). We believe that this is the result of gas evolution from the PMMA during exposure. With the relief structure against the resist, the evolved gas can be contained in the small volume between the thin areas of the mask and the wafer. In the case of grating patterns, it was found that extending the etched channels to the edge of the mask mounting ring completely eliminated any contact problems. In this case, the evolved gas is able to migrate down the channels and out from under the membrane.

Figures IV-10 and IV-11 are scanning electron micrographs of patterns replicated in PMMA. Polyimide membrane masks of total thickness 2 μm and etched depth 1 μm were used for these exposures. The incident energy of the protons was 200 keV. Figure IV-10 shows 0.3- μm slots spaced by 1 μm in 0.4- μm -thick PMMA. The PMMA pattern has an aspect ratio of approximately half that of the mask pattern, and has nearly vertical sidewalls. Figure IV-11 shows 0.16- μm lines and spaces in 0.13- μm -thick PMMA. At these dimensions, the sidewall definition remains excellent and any effects of proton scattering while passing through the 1- μm -thick mask areas are not apparent.

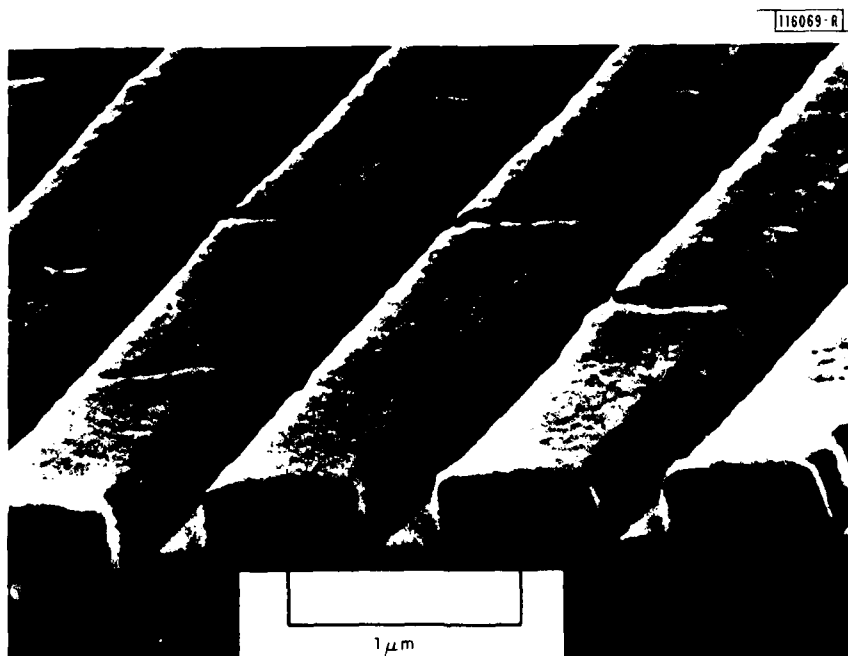


Fig. IV-10. Scanning electron micrograph of proton-exposed pattern in 0.4- μm -thick PMMA. Lines are 0.7 μm wide, and spaces are 0.3 μm wide.



Fig. IV-11. Scanning electron micrograph of 0.32- μm -period pattern in 0.13 μm of PMMA.

To replicate even finer features, a thinner membrane must be used. A polyimide membrane of 1- μm total thickness and 0.4- μm etch depth was used to produce the pattern shown in Fig. IV-12; the proton energy was 100 keV. The lines are approximately 600 Å wide and 0.28 μm high, spaced by 0.3 μm . The finer features reproduced along the edges of the lines and the steepness of the sidewalls indicate that the resolution is considerably better than 600 Å.



Fig. IV-12. Scanning electron micrograph of $\sim 600\text{-}\text{\AA}$ lines separated by $0.3\text{ }\mu\text{m}$. PMMA thickness is $0.28\text{ }\mu\text{m}$.

In conclusion, a new all-polyimide membrane mask for protons has been developed. Replication of features as small as $600\text{ }\text{\AA}$ has been demonstrated. By using thinner membranes, it should be possible to extend the resolution of this technique, and the replication of features as small as 100 to $200\text{ }\text{\AA}$ may be possible.

N.P. Economou
D.C. Flanders
J.P. Donnelly

C. CHARGE-COUPLED DEVICES: TWO-DIMENSIONAL CORRELATOR

Two-dimensional correlation is of interest for processing imagery and other data which occur in a two-dimensional format. Examples of its use include pattern recognition, correlation tracking, and linear-filtering operations such as edge detection and smoothing. In general this process is computation-intensive, and fast, special-purpose digital processors are often needed to perform the computations in a reasonable time. Because of their far more efficient computational power, CCDs offer the possibility of high-speed processing combined with the modest size and power consumption required in many military systems. In this report, we describe a high-speed CCD-based system which correlates a 256×256 signal with a 32×32 reference in approximately 1 s for a computation rate of more than 100 million operations per second.

A diagram of the two-dimensional correlator system is shown in Fig. IV-13. The signal and reference memory data are stored as 8- and 6-bit words, respectively, and coded in 2's-complement format. The actual correlation computation is performed by two CCDs, a programmable transversal filter (PTF) and an accumulating memory. The PTF^{12,13} is a 32-stage device whose tap-weight values are digitally programmable as 6-bit words, and is capable of operating at a 25-MHz clock rate, although we clock it at 5 MHz for the 2-D correlator.

The accumulating memory consists of a shift register with a charge storage site beside each shift-register cell. A sequence of charge packets can be loaded into the shift register and transferred laterally into the storage sites where they are added to previously stored packets. The contents of the storage sites can be brought back into the shift register and clocked out. We were able to use part of a 100×400 -element CCD imager¹⁴ for the accumulator. This device has a 405-stage output register with an electrical input, and charge can be exchanged between this register and the bottom row of 400 imaging cells, which serve as storage sites.

In this 2-D correlation system, we perform a series of 1-D correlations using the PTF and sum them in the accumulating memory to produce the 2-D

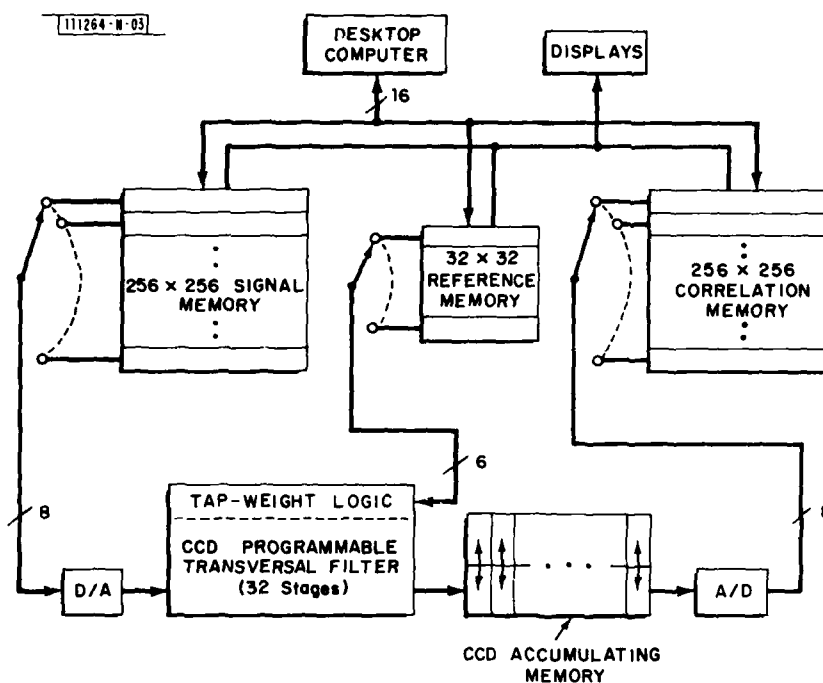


Fig. IV-13. Diagram of CCD-based system which performs correlation of a 256 x 256 signal with a 32 x 32 reference.

correlation. If $s(i,j)$ and $r(i,j)$ are the signal and reference values corresponding to row i and column j of each array, then the crosscorrelation $c(m,n)$ is given by

$$\begin{aligned}
 c(m,n) &= \sum_{i=0}^{31} \sum_{j=0}^{31} r(i,j) s(i+m, j+n) \quad m,n = 0,1,\dots,255 \\
 &= \sum_{i=0}^{31} p(i, i+m, n) \quad (IV-1)
 \end{aligned}$$

where

$$p(i, i+m, n) = \sum_{j=0}^{31} r(i,j) s(i+m, j+n) .$$

These equations also define a partial or one-dimensional correlation vector $p(i, i + m, n)$, $n = 0, \dots, 255$ which is the correlation of row i of the reference with row $i + m$ of the signal. Equation (IV-1) shows that 32 of these 1-D correlations are then vector-summed to produce $c(m, n)$ or row m of the crosscorrelation matrix. In our system, the PTF computes the p -vectors while the accumulating memory sums these vectors.

The sequence by which the 2-D correlation is formed is as follows. Row 0 of the reference is loaded into the PTF tap-weight storage and correlated with row 0 of the signal, and the result is stored in the accumulator. Then, row 1 of the signal and row 1 of the reference are correlated and the result added to the first correlation. This process continues until rows 31 of the signal and reference are correlated. The accumulator then contains the first row of the crosscorrelation, which is clocked out. To produce the second row of the crosscorrelation, reference rows 0 through 31 are correlated with signal rows 1 through 32, and for each succeeding cycle the starting address of the signal memory row is advanced by one. One additional point is that, for our system, the signal matrix indices in Eq. (IV-1) are to be understood as modulo 256. This means that the correlations are cyclic in both dimensions and that the 2-D correlation is of size 256×256 . This is the same procedure as would occur in a digital computation if the correlation is computed using 2-D discrete Fourier transforms, since cyclic convolutions are implicit in that method.

The correlation system shown in Fig. IV-13 is capable of expansion to larger signal- and reference-array sizes. The width (number of columns) of the signal memory is limited by the number of storage sites in the accumulator, while the height of the signal array could be expanded indefinitely. The width of the reference array is set equal to the number of taps on the PTF, while the reference height is limited by the charge storage capacity of the accumulator. Actually, the reference width can be made wider (within limits imposed by the accumulator charge capacity) by breaking each row of the reference into segments of 32 or less and correlating each segment with a given signal row. In this case, the addressing circuitry of the signal

AD-A118 847

MASSACHUSETTS INST OF TECH LEXINGTON LINCOLN LAB
SOLID STATE RESEARCH: 1982-1.(U)
FEB 82 A L MCWHORTER

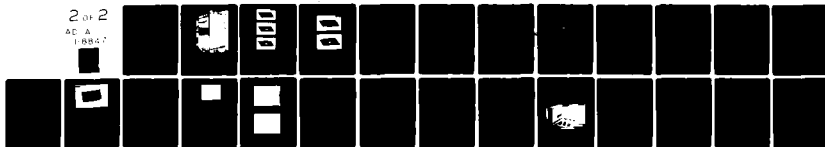
F/6 9/5

UNCLASSIFIED

ESD-TR-82-010

F19628-80-C-0002
NL

2 OF 2
AD A
1982-1



END
DATE
FILMED
09:32
DTIC

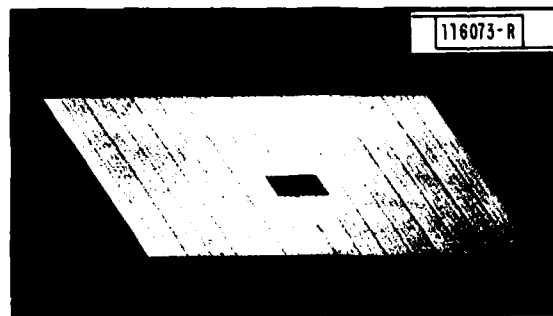
memory must start at different column indices for each reference segment to ensure that the partial correlations are properly aligned when summed in the accumulator. In addition to these possibilities, it should be mentioned that this concept can be extended to any number of dimensions for signal or reference. Thus, using the transversal filter/accumulator combination as the key computational component, any multidimensional correlator can be configured simply by modifying the addressing and timing logic and the size of the memories.

A photograph of the system in Fig. IV-14 shows a cage of 32 cards (mostly wire-wrap) and a control panel. A large fraction of the cards (13 plus a spare) are allocated to the 164K bytes of memory; 10 cards supply the remaining logic functions, such as clocking, memory control, and computer interface; and 5 cards supply the display drive signals. The CCDs and all their support circuitry occupy only 3 cards. The system size could easily be halved with a modest redesign effort, with the largest reduction occurring if the 8K static RAMs used in the memory were replaced with 64K dynamic RAMs.

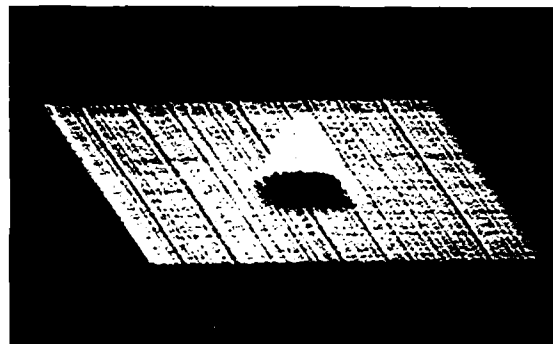
We have performed preliminary tests to demonstrate the system capabilities, and some results are shown in Figs. IV-15(a-c) and IV-16(a-b). In Fig. IV-15(a), a test signal is shown in a quasi-3-D display; it consists of a 32- x 32-pixel pyramid shape against a zero background. The pyramid height is 64, or 1/2 the maximum amplitude of 127 (signal memory range is -128 to +127). The 32 x 32 reference for these tests was the same pyramid, but with 6-bit resolution. This shape was chosen because it utilizes a variety of tap-weight configurations on the PTF and because it was easy to generate in software. Figure IV-15(b) shows the resulting correlation which has been digitized to 8 bits and stored in the correlation memory, while Fig. IV-15(c) shows the calculated result. The striations in the CCD correlation are a result of clock feedthrough, which we expect to be diminished with some further effort. In Fig. IV-16(a) we have added white Gaussian noise of rms value 64 to the pyramid so that signal/noise equals 1. The 2-D-correlation result shown in Fig. IV-16(b) clearly reveals the presence of the signal. In Figs. IV-16(a) and (b) the y-axis amplitude has been reduced from that of Fig. IV-15 by a factor of four for visual clarity.



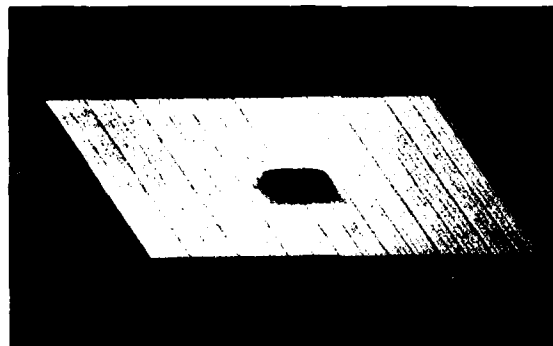
Fig. IV-14. Photograph of CCD 2-D correlator system. System uses 32 circuit boards, 3 of which contain CCDs and their support circuitry, while remaining boards are memory, support logic, and display drivers.



(a)



(b)

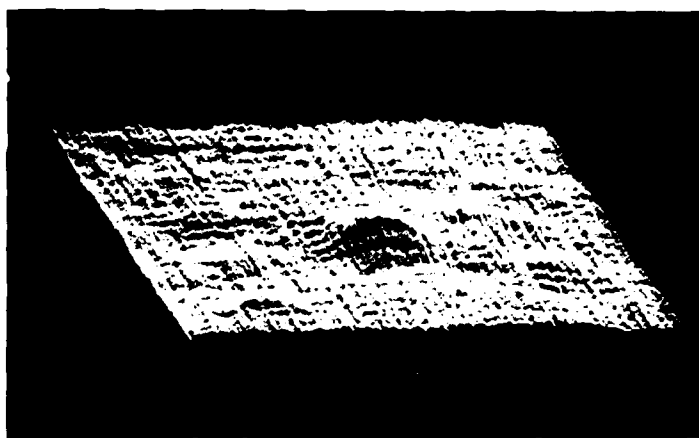


(c)

Fig. IV-15. (a) Photo of CRT display showing 256 x 256 input signal to correlator consisting of a 32 x 32 element pyramid shape. (b) CCD 2-D correlation of signal in (a) with a 32 x 32 reference consisting of same pyramid. (c) Exact calculation of correlation depicted in (b).



(a)



(b)

Fig. IV-16. (a) Same signal as displayed in Fig. IV-15(a) but with added white Gaussian noise of rms value equal to pyramid height. (b) Correlation of signal in (a) with 32 x 32 pyramid reference.

In these photographs the 2-D correlation required 1 s, but the high-speed correlations by the PTF used only about 0.4 s of this time. Most of the remaining time is required for loading the PTF tap-weight storage registers. This number could, with some improvements in logic design, be reduced to the point of nearly eliminating correlator idle time. Even with 1-s correlation time, the system is performing the equivalent of 64 million multiplies and adds per second.

B.E. Burke	G.R. McCully (Group 36)
A.M. Chiang	J.F. Melia (Group 36)
W.H. McGonagle	

REFERENCES

1. J.F. Gibbons and K.F. Lee, IEEE Electron Device Lett. EDL-1, 117 (1980).
2. E. Sun, B. Hoefflinger, J. Moll, C. Sodini, and G. Zimmer, Technical Digest of the International Electron Devices Meeting - 1980, Washington, DC, 8-10 December 1980, pp.791-794.
3. G.T. Goeloe, E.W. Maby, D.J. Silversmith, R.W. Mountain, and D.A. Antoniadis, Technical Digest of the International Electron Devices Meeting - 1981, Washington, DC, 7-9 December 1981, pp.554-556.
4. M. Komuro, N. Atoda, and H. Kawakatsu, J. Electrochem. Soc. 126, 483 (1979).
5. R.L. Seliger, R.L. Kubena, R.D. Olney, J.W. Ward, and V. Wang, J. Vac. Sci. Technol. 16, 1610 (1979).
6. D.B. Rensch, R.L. Seliger, G. Csanky, R.D. Olney, and H.L. Stover, J. Vac. Sci. Technol. 16, 1897 (1979).
7. L. Karapiperis and C.A. Lee, Appl. Phys. Lett. 35, 395 (1979).
8. J.F. Fanni, Air Force Weapons Laboratory Technical Report No. AFWL-TR-65-150 (September 1966).

9. D.C. Flanders and H.I. Smith, J. Vac. Sci. Technol. 15, 995 (1978), DDC AD-A061201/0.
10. P.D. DeGraff and D.C. Flanders, J. Vac. Sci. Technol. 16, 1906 (1979), DDC AD-A090069/6.
11. D.B. Rensch, private communication.
12. Solid State Research Report, Lincoln Laboratory, M.I.T. (1980:2), pp.26-29, DTIC AD-A092724/4.
13. A.M. Chiang and B.E. Burke, 1980 Government Microcircuit Applications Conference Digest of Papers, Houston, Texas, November 1980, pp.182-183.
14. Solid State Research Report, Lincoln Laboratory, M.I.T. (1979:4), pp.56-59, DDC AD-A084271/6.

V. ANALOG DEVICE TECHNOLOGY

A. CONSIDERATIONS FOR AN INTEGRATED OPTICAL SPECTRUM ANALYZER (IOSA)

In a previous report,¹ the design of the detector array and input lens of an IOSA were discussed. This report addresses the design of the Bragg cell and the output lens.

1. Bragg-Cell Design

The Bragg cell (Fig. V-1) is the heart of an IOSA. The collimated optical beam from the input lens is diffracted by a traveling acoustic wave via the photoelastic nonlinearity of the cell. The diffraction angle θ_B (Fig. V-2) is

$$\theta_B = \sin^{-1} \frac{\lambda_o f}{2nv_a} \quad (V-1)$$

where λ_o is the optical wavelength, n is the refractive index, v_a is the acoustic velocity, and f is the acoustic frequency. For small diffraction angles, the beam deflection is thus linearly related to the acoustic frequency.

The most important parameters of the Bragg cell are diffraction efficiency and bandwidth. The efficiency can be increased by increasing the acoustic power P_a or the interaction width L . In practice, however, the acoustic power is limited to less than ~ 1 W by transducer and amplifier considerations. Increasing the interaction width reduces the bandwidth because of the accumulated phase mismatch ΔkL (Fig. V-2) across the cell for frequencies not satisfying the Bragg condition [Eq. (V-1)]. Thus, a compromise must be made between efficiency and bandwidth. For isotropic diffraction, the 3-dB acoustooptic bandwidth is approximately given by

$$\Delta f = \frac{1.77 nv_a^2 \cos \theta_B}{f_o \lambda_o L} \quad (V-2)$$

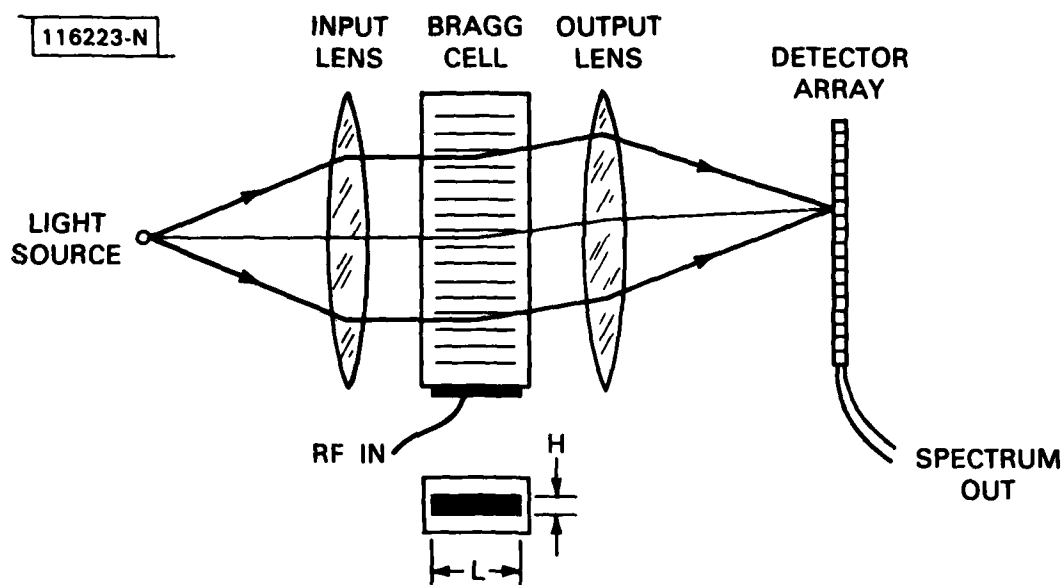


Fig. V-1. Block diagram of an acoustooptic spectrum analyzer.

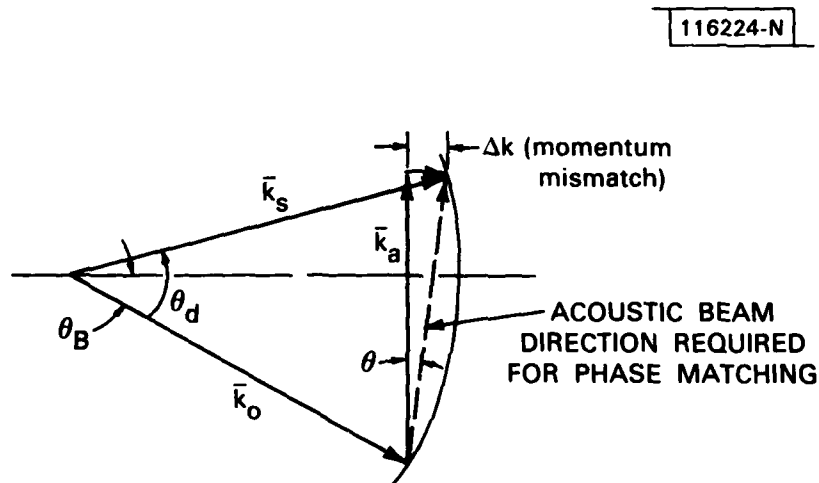


Fig. V-2. Isotropic Bragg-scattering diagram.

The corresponding diffraction efficiency for an octave bandwidth ($\Delta f/f_0 = 2/3$) is

$$\eta = \frac{13.1 \text{ nM}_2^2 P_a \Lambda_o^2 \cos \theta_B}{\lambda_o^3 H} \quad (\text{V-3})$$

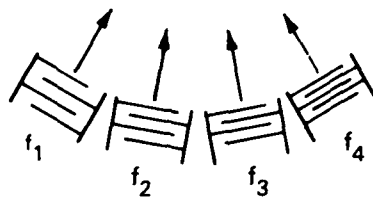
where M_2 is an acoustooptic figure of merit,² Λ_o is the acoustic wavelength, and H is the height of the acoustic beam. For a typical SAW device on LiNbO_3 , η is less than 0.5 percent. A higher efficiency is desirable in order to achieve a larger dynamic range. An upper limit of $\eta \approx 5$ percent is consistent with requiring two-tone intermodulation products < -40 dB (see Ref. 3). Isotropic diffraction efficiency is thus one-order-of-magnitude lower than desired. Two techniques can be used to increase the efficiency-bandwidth product: beam steering and birefringent diffraction.

With beam steering, the direction of the acoustic beam is varied to more closely satisfy the Bragg condition over an extended frequency range. Three transducer configurations for achieving this⁴⁻⁶ are shown in Fig. V-3(a-c). A passive phased array has the advantage that it can also be implemented with bulk-wave transducers [Fig. V-3(c)-(ii)]. Unfortunately, the Bragg angle cannot be tracked exactly with a phased array. However, considerable bandwidth broadening can be achieved. If the Bragg condition is satisfied at two frequencies equally spaced on either side of the center frequency f_o ,

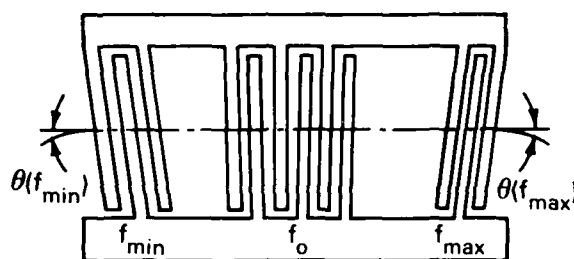
$$\left(\frac{\Delta f}{f_o}\right)_{\text{ph.array}} = \left[2 \left(1 - \frac{\delta\phi_o}{0.442} \right) \left(\frac{\Delta f}{f_o}\right)_{\text{iso.}} \right]^{1/2} \quad (\text{V-4})$$

where $\delta\phi_o = \Delta kL/2$ is the phase mismatch at f_o . For example, if a 1-dB dip in diffraction efficiency at f_o is acceptable, then $\delta\phi_o \approx -0.262$ and

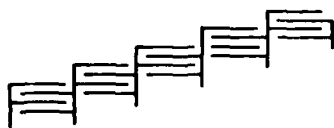
$$\left(\frac{\Delta f}{f_o}\right)_{\text{ph.array}} = 1.26 \sqrt{2} \left(\frac{\Delta f}{f_o}\right)_{\text{iso.}}^{1/2} \quad (\text{V-5})$$



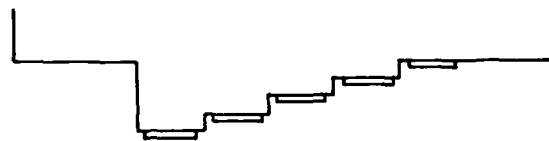
(a)



(b)



(i)



(ii)

(c)

Fig. V-3. Beam-steering transducer configurations: (a) array of stagger-tuned tilted SAW interdigital transducers; (b) SAW chirp transducer with continuously tilted fingers; (c) passive phased arrays: (i) SAW interdigital transducers, (ii) bulk-wave transducers.

The diffraction efficiency of an octave-bandwidth transducer with and without beam steering is shown in Fig. V-4.

While beam steering is possible in all media, birefringent diffraction is applicable only to anisotropic crystals such as LiNbO_3 . Incident and diffracted beams have different polarizations and thus propagate with a different phase velocity. With anisotropic diffraction, the acoustic k-vector required for phase matching (i.e., Bragg diffraction) can be chosen to be tangential to the k-surface of the diffracted beam (Fig. V-5). The momentum mismatch Δk of the diffracted beam is then much less than for isotropic diffraction (Fig. V-2). The bandwidth is identical to isotropic diffraction with a phased-array transducer calculated by Eq. (V-4). A further benefit of birefringence is that the change in polarization of the diffracted beam may permit discrimination against the undiffracted beam.

Finally, beam steering and birefringent diffraction can be used together. This does not result in any further gain in bandwidth. However,

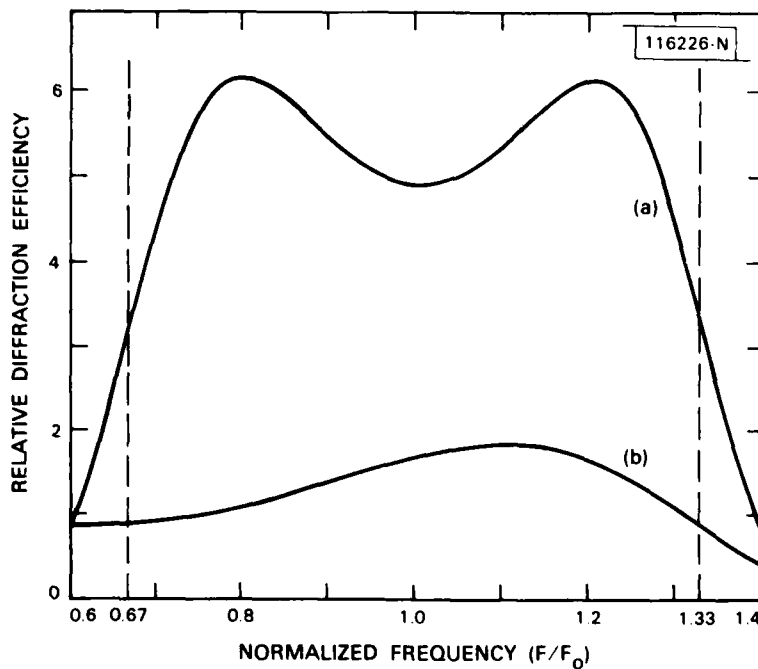


Fig. V-4. Relative diffraction efficiency of an octave-bandwidth Bragg cell employing (a) a phased-array transducer, and (b) a single transducer.

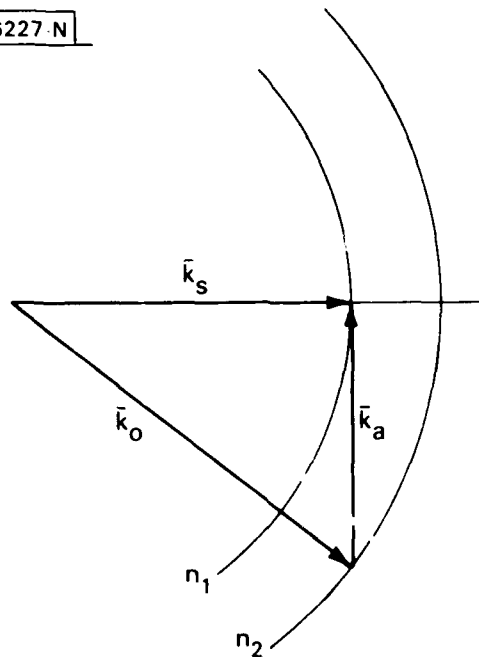


Fig. V-5. Anisotropic Bragg-scattering diagram.

offers the advantage of achieving broadband birefringent diffraction in a crystal which is not sufficiently anisotropic to realize the birefringent broadening considered above. The required birefringence is given by

$$\Delta n = \frac{f_o \lambda_o}{2n v_a} \quad (V-6)$$

which may exceed that which can be obtained from the crystal.

2. Output-Lens Design

The output lens focuses the diffracted output of the Bragg cell on the detector array in the focal plane. Selection of the appropriate optical aperture and weighting were considered previously¹ with respect to the design of the input lens. It is therefore assumed that no weighting is required in the output lens. In this respect, the design of the output lens is somewhat

simpler than the design of the input lens. However, the output lens has one additional requirement: it must have a sufficiently wide field of view to accept the full angular distribution of the diffracted light. In contrast, the field of view of the input lens can be much less. For 1-GHz bandwidth diffraction by a SAW on LiNbO_3 ($\lambda_0 = 0.82 \mu\text{m}$, $n = 2.2$, $v_a = 3488 \text{ m/s}$), from Eq. (V-1) the estimated required angular field of view is approximately 3.1° for the output lens.

Means by which to combine, in integrated form, the weighted input lens, wide-aperture output lens, and monolithic detector array described previously with a bulk-acoustic-wave Bragg cell incorporating beam steering are currently under study.

P.V. Wright

B. SUPERCONDUCTIVE CONVOLVER

Superconductive convolvers capable of processing wideband (2 to 10 GHz) analog signals are currently under development. These devices will be based upon a superconductive, niobium technology developed at Lincoln Laboratory and elsewhere. Fabrication techniques for producing stable, high-quality, superconductive tunnel junctions and high-resolution niobium patterns currently exist.⁷ The tunnel junctions provide the efficient nonlinear elements for mixing, while the superconductive niobium lines provide low-loss circuits for electromagnetic delay and summation. Realization of adequate delay ($>100 \text{ ns}$) on reasonably sized substrates ($<25 \text{ cm}^2$) requires the development of long ($>10 \text{ m}$) superconductive lines on thin ($25 \text{ to } 125 \mu\text{m}$), defect-free dielectrics.⁸ The goal is to achieve time-bandwidth products of 1000 or greater, which will require an integrated superconducting circuit with 1000 or more mixers.

A preliminary superconductive convolver has been fabricated and evaluated; it is shown in Fig. V-6. The device consists of a 1.5-m-long meander line, 20 proximity taps, 19 mixers, 19 bias resistors, and a low-impedance

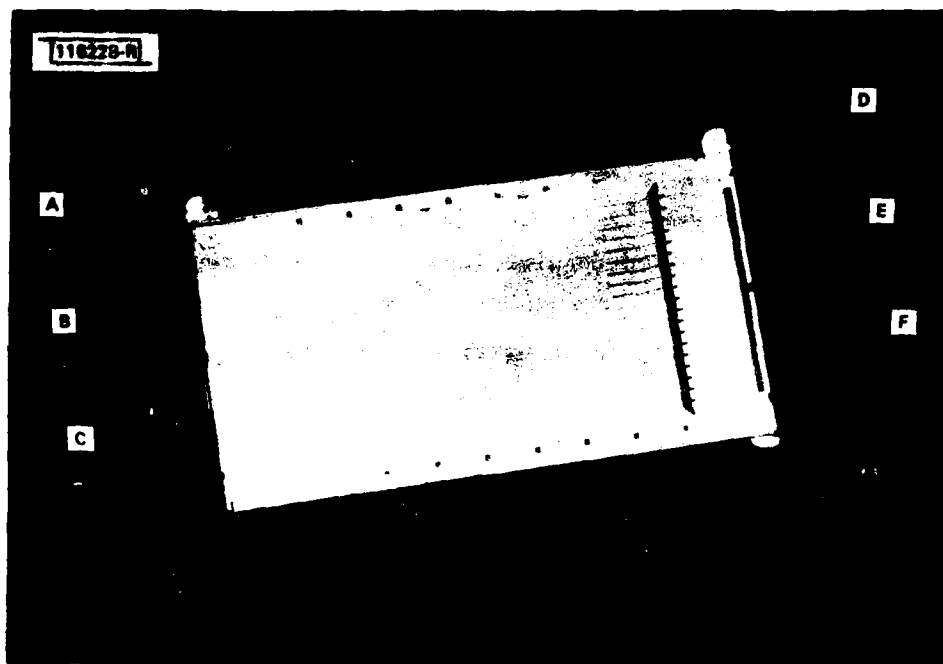


Fig. V-6. Superconductive convolver with 19 taps fabricated on a sapphire substrate.

output line integrated on a crystalline sapphire substrate ($2.5 \times 5.1 \times 0.013$ cm). It is fabricated with eight thin films. A niobium ground plane is on the underside. The seven layers on the topside include a niobium meander line occupying most of the substrate surface, and a niobium output line. Windows etched in silicon monoxide over the output line allow formation of thin niobium pentoxide tunnel barriers. A covering of lead forms the mixer counterelectrodes, as well as the tap array. An array of meander indium-gold resistors feeds bias to the mixers. An additional layer of silicon monoxide provides passivation.

Signal and reference waveforms are entered at ports A and C, respectively, and counterpropagate through the niobium meander line. The coupling of the meander line to a single tap can be measured at port B. The remaining 19 taps, integrated with mixers, create the product of local signal and reference fields. Bias currents to optimize mixing efficiency are distributed through normal-metal resistors from port E. The output signal, obtained by

spatially summing the mixer products on the output line, propagates to port D, with port F being terminated. Propagation of the signals from opposite ends of the delay line produces a relative reversal and shifting of the input waveforms, the nonlinear element multiplies, and the short output transmission line integrates; thus, the output signal represents the convolution of the input signals. Because both of the spatial patterns are moving, there is a halving of the time scale at the output - that is, the center frequency and bandwidth are doubled.

The 1.5-m-long delay line has a measured voltage reflection coefficient of 0.03 (implying an impedance of 53Ω) and provides a delay of 14 ns, as shown in Fig. V-7. The meander line has 40 bends with time-delay spacings of 0.33 ns and 19 capacitive taps with spacings of 0.67 ns. The meander-line bends have a small effect on the delay-line response. However, the capacitive loading of the delay line by the taps is readily observed with time-domain reflector measurements. The tap-to-delay-line coupling is larger than predicted, being a nominal -20 dB with ± 6 dB of ripple over the desired 2- to 4-GHz input band. New designs will incorporate weaker tap coupling. The periodic spacing of the taps introduces a 200-MHz-wide stopband near the center frequency (~ 3 GHz) of the device. This effect will be minimized by reducing the magnitude of the capacitive discontinuities and by some randomization in tap spacings and line lengths.

By injecting a short pulse (~ 200 ps) into the input delay line, the coupling into the output line can be observed directly with a sampling oscilloscope, as shown in Fig. V-8. The first and last pulses in the photograph are dominated by direct coupling between the input and output circuits as the short pulse enters and leaves the microstrip delay line. The 18 pulses in-between, and a portion of the last pulse, are due to sampling of the propagating pulse by the capacitive taps. The amplitude taper (~ 8 dB) of the sampled pulse is due to predicted propagation losses on the output line. This loss is introduced by loading of the output line by the mixers and bias resistors. The loading can be reduced by increasing the impedance of the diodes or by lowering the impedance of the output line below its current $12\text{-}\Omega$ value.

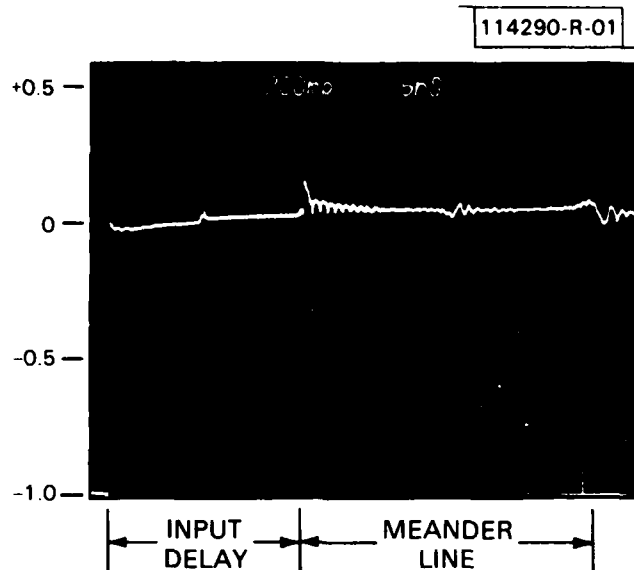


Fig. V-7. Time-domain reflectometer response of convolver delay line to step-function applied voltage, showing sum of incident and reflected voltages as a function of time. For convenience, the vertical scale has been calibrated to read directly in voltage reflection coefficient by assigning zero reflection to the response of a $50\text{-}\Omega$ termination and negative unit reflection to the response for a short-circuit termination. Small bumps appearing at delay times of about 10, 19, 33, and 47 ns are due to discontinuities associated with packaging. Closely spaced reflections are due to capacitive loading of superconductive transmission line by taps. Scales: vertical, 0.2/div; horizontal, 5 ns/div.

The output spectrum of the device with input tones centered at 3.45 and 3.55 GHz is shown in Fig. V-9. The line centered at 7.0 GHz is the desired product of the two input tones. The spectral lines centered at 6.9 and 7.1 GHz are the self-products of the individual inputs. This is a source of spurious signal which occurs because the discrete nature of the taps and mixers does not afford wavevector selection between the spatially uniform cross-product and the spatially varying self-products. These self-products can be suppressed in a variety of ways. Random placement of the discrete

116229-S

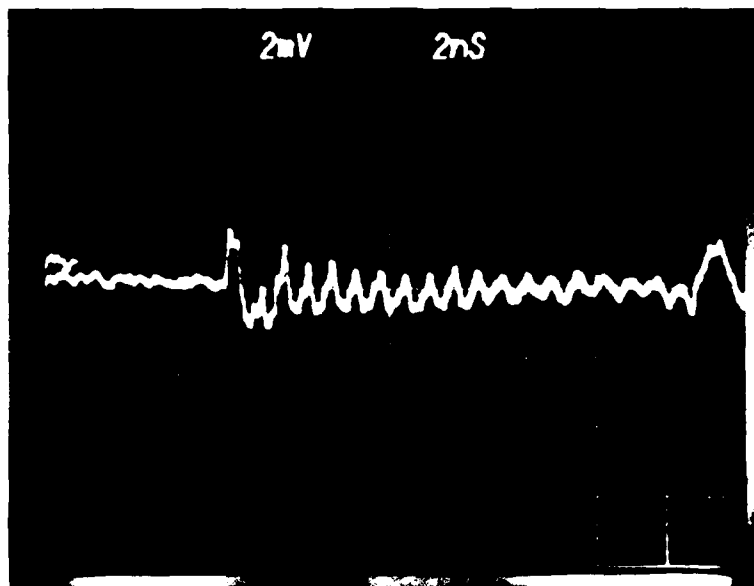


Fig. V-8. Response at convolver output port with very short (~200 ps) input pulse.

116230-S

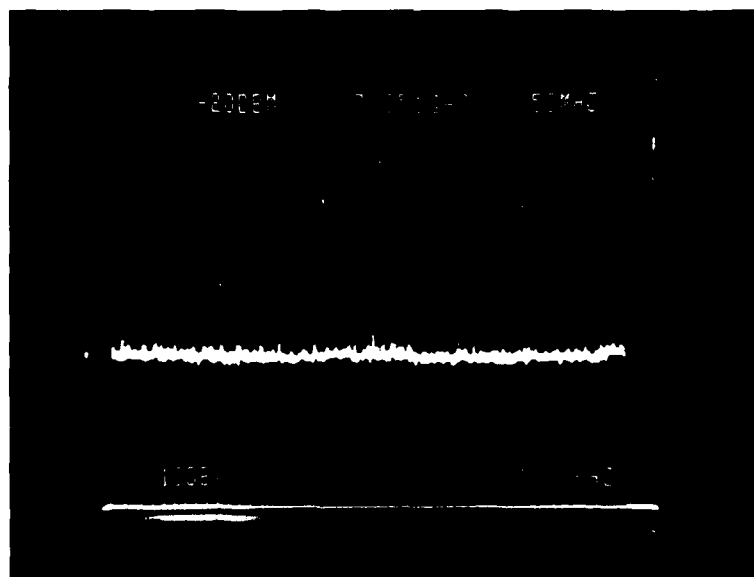


Fig. V-9. Output spectrum of convolver with input CW tones centered at 3.45 and 3.55 GHz.

taps, or use of offset input frequencies and a propagating output, should result in these spurious signals being averaged to acceptable levels. Alternatively, balanced mixer configurations can be used. The measurement in Fig. V-9 was made at very narrow bandwidth (0.1 MHz). When wideband (~4 GHz) measurements are made, the thermal noise floor is near or even above the output level of the desired cross-product. Future designs will incorporate impedance-matching output circuits to improve the device dynamic range. Because of the very low losses (<1 dB) in the meander line, the input efficiency of the device is more than adequate. However, saturation of the superconductive diodes will impose an upper limit on the maximum output power which can be obtained. The dynamic range of the device will be further improved by using serial arrays of the superconductive diodes at each tap.

S.A. Reible
R.W. Ralston
A.C. Anderson

C. COMPACT MULTIPLE-CHANNEL SAW SLIDING-WINDOW SPECTRUM ANALYZER

A SAW chirp-Fourier-transform spectrum analyzer is under development for use by Lincoln Laboratory in an airborne CO₂ laser radar operating at 10.6 μ m (see Refs. 9 and 10). The radar is designed to first detect moving objects using a CW mode of operation, then to identify and classify these objects by providing high-resolution images using a pulsed mode. The high carrier frequency results in a large 84-kHz Doppler-shifted return from a target moving 1.6 km/h (1 mph) relative to a stationary target. To accommodate a ± 100 -km/h range, a bandwidth of about 10 MHz is required.

The parameters of the spectrum analyzer needed for moving-target identification (MTI) are well matched to those available from a SAW chirp-Fourier-transform system.^{11,12} Furthermore, the speed, size, power, and weight advantages of the SAW approach are particularly important for this application, which requires simultaneous processing of 12 scanning laser beams. Additional specifications for the spectrum analyzer are a dynamic range greater than 50 dB, a peak-to-first-sidelobe ratio greater than 25 dB,

an input duty factor greater than 50 percent, no more than a 20-MHz output-spectrum sampling rate (at one sample per 84-kHz resolution cell), and an input power below -10 dBm.

1. System Architecture

Two basic configurations, the multiply-convolve-multiply (M-C-M) and the convolve-multiply-convolve (C-M-C), exist for implementing a SAW chirp-transform spectrum analyzer. The spectral phase is of no interest; thus, the final multiply in the M-C-M structure can be omitted. This structure is denoted by M-C-(M). Since only narrowband inputs are to be processed, the first convolving element in the C-M-C structure can be eliminated. This structure is denoted by (C)-M-C. These configurations are shown schematically in Fig. V-10. The (C)-M-C version has a "sliding" window producing

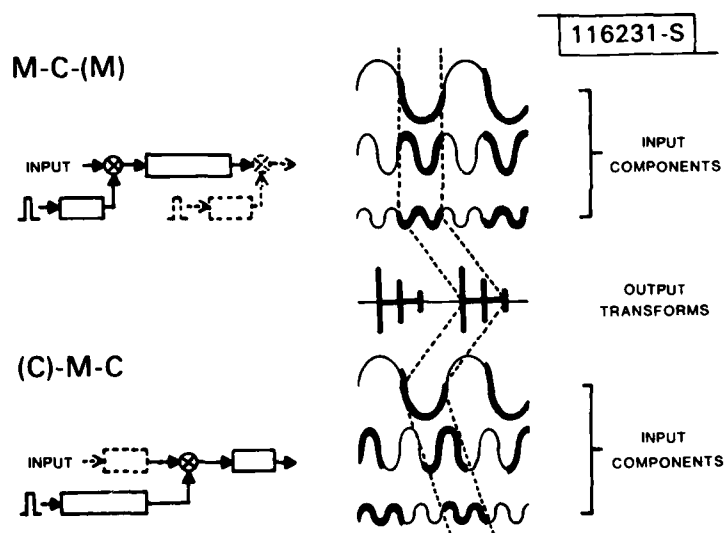


Fig. V-10. Multiply-convolve-(multiply) and (convolve)-multiply-convolve configurations.

the output from different input time windows, depending on input frequency. Although both these variations are M-C structures, the multiplying-chirp duration is shorter than the convolving-chirp duration in the M-C-(M) structure, while the opposite is true for the (C)-M-C structure. In each case, the output is valid only over a period of time given by the difference in length between the convolving and the multiplying chirps.

Weighting required for sidelobe suppression is readily incorporated as an amplitude weighting of the compressor in the (C)-M-C structure, whereas the input to the M-C-(M) structure must be preweighted for sidelobe suppression. Thus, the 12-channel spectrum analyzer uses the simpler (C)-M-C structure in which 12, short, internally weighted compressors, one for each channel, are fed with inputs premultiplied by a single long expander.

2. Device Characteristics

All the chirp filters used for this application are reflective-array compressors (RACs). The 25-dB sidelobe-suppression requirement was exceeded by choosing a modified Hamming weighting with cosine-squared tails for the compressors. With this compressor impulse response, the far-out sidelobes fell off significantly faster than the unmodified Hamming roll-off. The 20- μ s length chosen for the compressor produced a 3-dB Hamming resolution of 63 kHz, while the 30- μ s length chosen for the expander produced a 67-percent input duty factor and a 33-percent output duty factor. The compressor length is consistent with the coherence time expected of the target returns, and the 10- μ s-long 10-MHz-bandwidth output spectrum requires only a 12-MHz output-sampling rate at the 84-kHz resolution. The 10-MHz output was obtained using a bandwidth of 20 MHz for the compressor and 30 MHz for the expander.

In order to eliminate the need for spectral inversion of the expanded chirp, the 12 compressors are up-chirp devices while the single expander is a down-chirp device. The center frequencies of these devices were kept relatively low to avoid the higher propagation losses encountered in high-frequency up-chirp devices. Center frequencies of 85 MHz for the compressors and 125 MHz for the expander were chosen, which resulted in a satisfactory

level of mixer spurious signals and percentage bandwidths below the 25-percent reasonable upper limit for RAC devices.

The midband insertion loss for both RAC devices is 30 dB and provides the required triple-transit suppression. The expander possesses ~ 3.5 dB of $(x/\sin x)$ weighting to compensate for the spectrum of the 32-ns-wide 4-cycle impulse used for chirp generation. With 5- μ s device pedestals of delay, the valid output spectrum emerges ~ 30 μ s after reception of an impulse trigger and extends for 10 μ s.

3. The Spectrum Analyzer

A diagram of the 12-channel spectrum analyzer is shown in Fig. V-11. The chirp generator, shared by all the channels, contains an impulse generator, the expander, amplifiers, monitors, and a two-way divider, all on a single 8- x 10-in. printed-circuit (PC) board utilizing 50- Ω lines for RF signals.

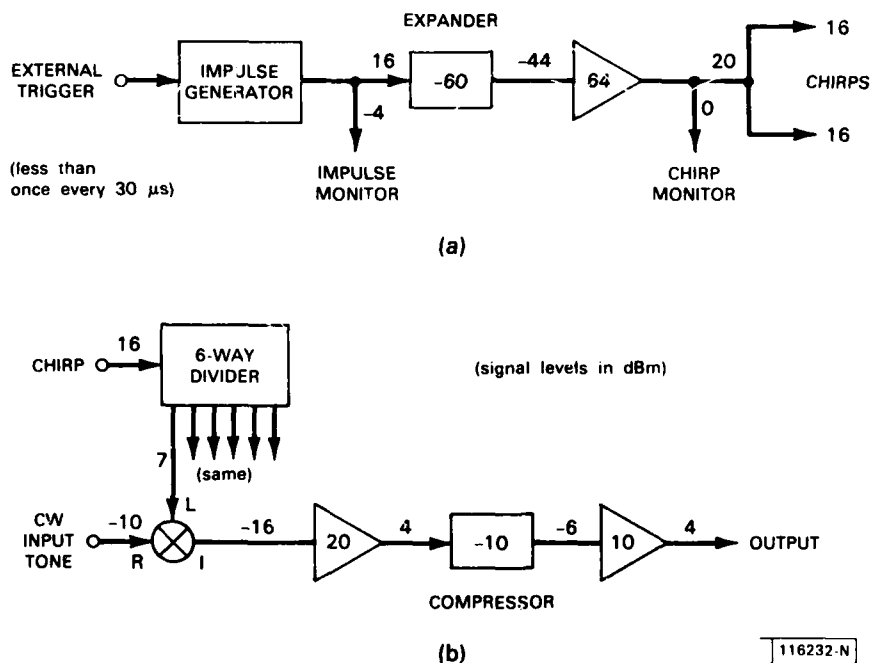


Fig. V-11. Circuit schematic of 12-channel SAW spectrum analyzer: (a) chirp-generator board, (b) analyzer board.

The 12 channels, each consisting of a single compressor, a mixer, and amplifiers, are contained - 6 channels to a board - on two 8- x 10-in. PC boards. The multiplying chirp is evenly divided six ways on each of the spectrum-analyzer boards. The power levels shown in Fig. V-11 were chosen to minimize overall power, size, cost, and weight while meeting the specified requirements. Together, the three boards draw approximately 16 W. These boards are mounted in a 3- x 8- x 10-in. module which is shown in Fig. V-12 with a spectrum-analyzer board removed and the chirp-generator board exposed. Accuracy is maintained even with temperature drifts by processing the temperature-variable location of the spectral components relative to a purposely injected zero-Doppler component. Although not all the required RAC compressors have been fabricated, tests with existing compressors have shown that every system requirement has been met or exceeded.

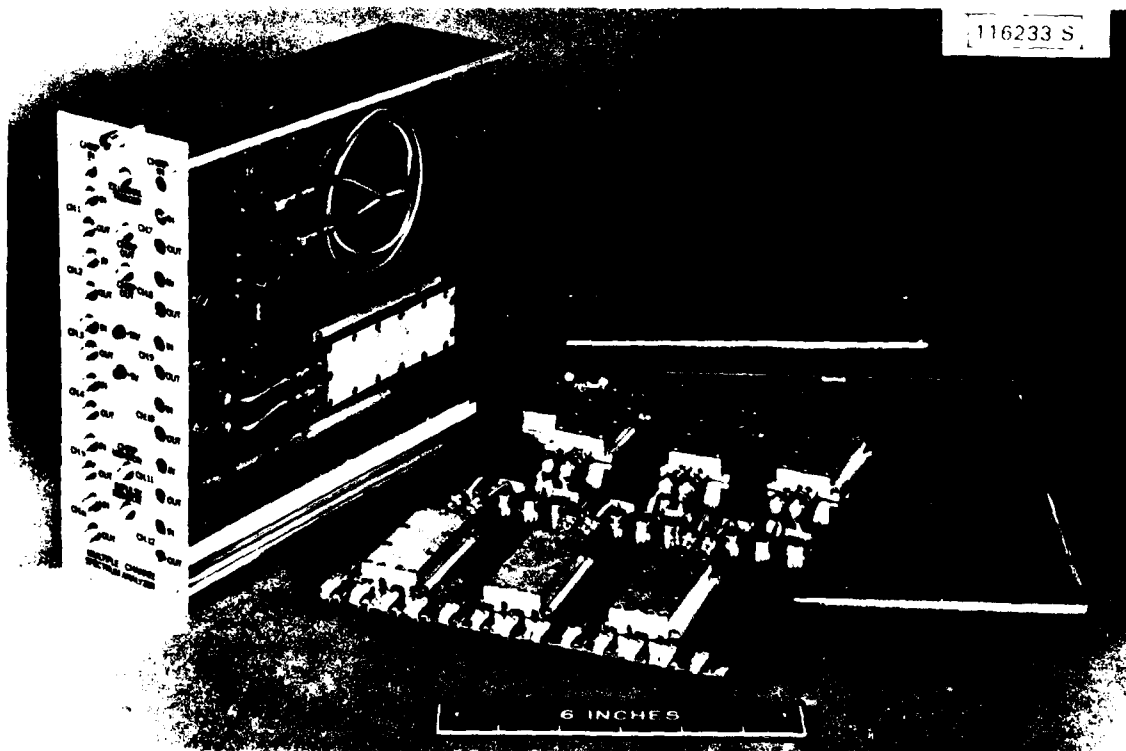


Fig. V-12. Multiple-channel spectrum-analyzer module with cover and a 6-channel compressor board removed to expose chirp-generator board.

The major components of a laser radar system, complete with the SAW spectrum analyzer, are currently being extensively tested in the laboratory. A typical result is shown in Fig. V-13. An automobile was driven at constant velocity through a stationary beam. The characteristic, single-velocity return of the car body changes to a broad, high-velocity return as the wheels - somewhat above axle height - are illuminated.

D.R. Arsenault
V.S. Dolat

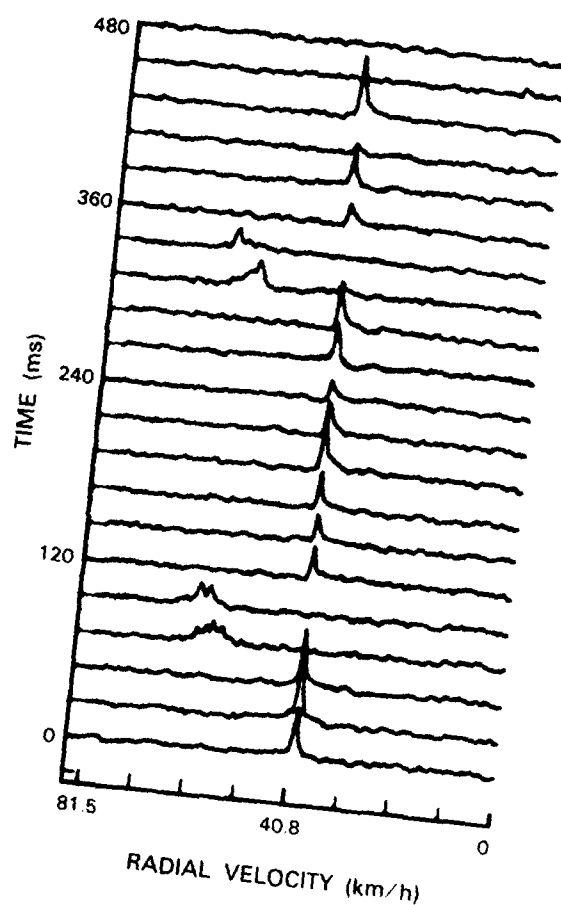
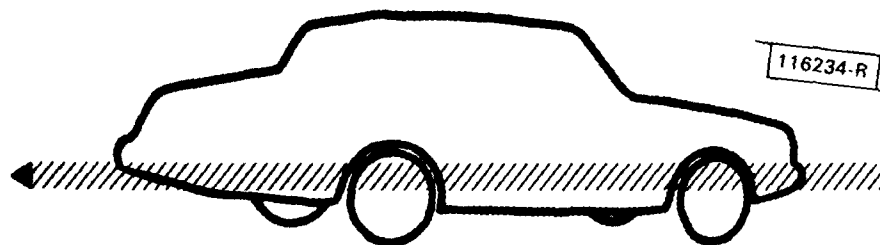


Fig. V-13. Successive Doppler-shifted spectra obtained from an MTI scan of an automobile by processing radar return every 24 ms using SAW analyzer.

REFERENCES

1. Solid State Research Report, Lincoln Laboratory, M.I.T. (1981:3), p.63, DTIC AD-A112696.
2. N. Uchida and N. Nuzeki, Proc. IEEE 61, 1073 (1973).
3. D.L. Hecht, in 1973 Ultrasonics Symposium Proceedings (IEEE, New York, 1973), p.98.
4. C.S. Tsai, M.A. Alhaider, L.T. Nguyen, and B. Kim, Proc. IEEE 64, 318 (1976).
5. T.R. Joseph and B.U. Chen, in 1976 Ultrasonics Symposium Proceedings (IEEE, New York, 1976), p.28.
6. A. Korpel, R. Adler, P. Desmares, and W. Watson, Proc. IEEE 54, 1429 (1966).
7. S.A. Reible, IEEE Trans. Magnetics MAG-17, 303 (1981), DTIC AD-A102938/8.
8. Solid State Research Report, Lincoln Laboratory, M.I.T. (1981:2), p. 57, DTIC AD-A110947.
9. L.J. Sullivan, in SPIE Vol.227: CO₂ Laser Devices and Applications (Society of Photo-Optical Instrumentation Engineers, Bellingham, Washington, 1980), p.148, DTIC AD-A102689/7.
10. R.J. Hull and S. Marcus, in Proceedings of the IEEE 1978 National Aerospace and Electronics Conference (IEEE, New York, 1978), p.662.
11. R.C. Williamson, J.T. Lynch, D.R. Arsenault, and V.S. Dolat, in Coherent Laser Radar for Atmospheric Sensing, Technical Digest (Optical Society of America, New York, 1980), p.WA7-1.
12. Solid State Research Report, Lincoln Laboratory, M.I.T. (1980:2), p.37, DDC AD-A092724/4.

UNCLASSIFIED

SECURITY CLASSIFICATION OF THIS PAGE (When Data Entered)

REPORT DOCUMENTATION PAGE		READ INSTRUCTIONS BEFORE COMPLETING FORM
1. REPORT NUMBER ESD-TR-82-010	2. GOVT ACCESSION NO. AD-A118847	3. RECIPIENT'S CATALOG NUMBER
4. TITLE (and Subtitle) Solid State Research		5. TYPE OF REPORT & PERIOD COVERED Quarterly Technical Summary 1 November 1981 - 31 January 1982
		6. PERFORMING ORG. REPORT NUMBER 1982: 1
7. AUTHOR(s) Alan L. McWhorter		8. CONTRACT OR GRANT NUMBER(s) F19628-80-C-0002
9. PERFORMING ORGANIZATION NAME AND ADDRESS Lincoln Laboratory, M.I.T. P.O. Box 73 Lexington, MA 02173-0073		10. PROGRAM ELEMENT, PROJECT, TASK AREA & WORK UNIT NUMBERS Program Element No.63250F Project No.649L
11. CONTROLLING OFFICE NAME AND ADDRESS Air Force Systems Command, USAF Andrews AFB Washington, DC 20331		12. REPORT DATE 15 February 1982
14. MONITORING AGENCY NAME & ADDRESS (if different from Controlling Office) Electronic Systems Division Hanscom AFB, MA 01731		13. NUMBER OF PAGES 124
		15. SECURITY CLASS. (of this report) Unclassified
		15a. DECLASSIFICATION DOWNGRADING SCHEDULE
16. DISTRIBUTION STATEMENT (of this Report) Approved for public release; distribution unlimited.		
17. DISTRIBUTION STATEMENT (of the abstract entered in Block 20, if different from Report)		
18. SUPPLEMENTARY NOTES None		
19. KEY WORDS (Continue on reverse side if necessary and identify by block number)		
solid state devices	photodiode devices	infrared imaging
quantum electronics	lasers	surface-wave transducers
materials research	laser spectroscopy	charge-coupled devices
microelectronics	imaging arrays	acoustoelectric devices
analog device technology	signal processing	
20. ABSTRACT (Continue on reverse side if necessary and identify by block number)		
<p>This report covers in detail the solid state research work of the Solid State Division at Lincoln Laboratory for the period 1 November 1981 through 31 January 1982. The topics covered are Solid State Device Research, Quantum Electronics, Materials Research, Microelectronics, and Analog Device Technology. Funding is primarily provided by the Air Force, with additional support provided by the Army, DARPA, Navy, NASA, and DOE.</p>		

UNCLASSIFIED

SECURITY CLASSIFICATION OF THIS PAGE (When Data Entered)